

PhD Thesis

**Exciton Behavior in Organic
Semiconducting Crystals: Essential Factor
for Realizing Electrically Driven Lasers**

(有機半導体単結晶中の励起子の挙動：電流励起レーザーの
実現に向けて)

Shang Hui

尚 慧

Department of Physics
Graduate School of Science
Tohoku University
September, 2015

Exciton behavior in organic semiconducting crystals:

Essential factor for realizing electrically driven lasers

有機半導体単結晶中の励起子の挙動：電流励起レーザーの実現に向けて

Introduction

Organic semiconductor lasers have been attracting considerable attention due to their unique advantages such as color-tunability, low production cost, and plastic-like flexibility. To date, all lasers reported are optically pumped, which have a cumbersome and expensive configuration. There is, therefore, great interest in developing an electrically driven laser as it would provide a new class of convenient and easy-to-manufacture laser. It is still a challenge to create sufficient current-induced exciton density for population inversion. This can be solved from the two aspects: one being decreasing the lasing threshold or the other being creating sufficient current density.

The purpose of this PhD research is to challenge these alternatives towards the final goal of electrically driven lasers. First, I focused on reducing the lasing threshold. Specific analysis of gain properties of organic single crystals are described in Chapter 3 of the dissertation. I finally concluded that the number of gain-narrowed peaks is affected by the re-absorption, and the energy distribution of gain is determined by the transition probability and bleaching of the ground-state absorption. Based on these findings, an ideal model for designing a high efficient laser material was given as a guiding principle.^[1] Another idea to reduce lasing threshold is co-doping of high fluorescent material as an emission center. In Chapter 4, I have successfully doped a certain quantity of CNDPASDB (oligo(*p*-phenylene vinylene)1,4-bis(R-cyano-4-diphenylaminostyryl)-2,5-diphenylbenzene) into *trans*-DPDSB (2,5-diphenyl-1,4-distyrylbenzene with

two *trans* double bonds). Light emission color can be varied from blue to green, white and yellow by changing the doping concentration, and superb high external quantum yield (EQY) (~80%) was obtained. Finally, it is proved that dopant materials with smaller energy band gap may introduce carrier-traps, which means doping must be smartly used, otherwise it will be a waste of efforts.^[2]

As described earlier, creating sufficient current density is also an important alternative for realizing laser. Considering the intrinsic confliction between carrier transport and luminescent efficiency in general materials, separation in functions of carrier-transport and light-emission is an intelligent strategy. In this dissertation, I further report a fabrication and characterization of a transistor with bilayer structure, which consists of a high field-effect mobility bottom layer and a high EQY top layer (figure 1), and its emission mechanism in terms of exciton behavior in this new device structure was described.

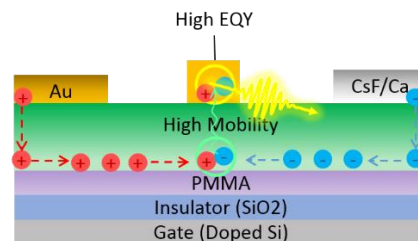


Figure 1. Schematic side-view diagram of bilayer light-emitting transistors. Green layer at bottom stands for tetracene crystal, top layer is doped tetracene.

Experiments

Both pure and 4-(dicyanomethylene)-2-methyl-6-(*p*-dimethylaminostyryl)-4*H*-pyran (DCM1)-doped tetracene crystals were prepared by a physical vapor transport method. Their optoelectronic properties, such as photoluminescence, EQY and field-effect mobility, were studied. Exciton diffusion length along the *c* axis in a tetracene crystal was obtained by characterization of polarization-dependent absorption coefficient and photocurrent. For fabrication of a bilayer transistor, a DCM1-doped crystal was laminated on the center position of the tetracene crystal. Asymmetric Au and CsF/Ca electrodes were employed for injection of holes and electrons, respectively. To investigate the transistor operations, a transistor with a 6-nm TTC (CH₃(CH₂)₄₂CH₃) thin film deposited between the two crystal layers as an exciton blocking layer was also employed.

Results and Discussions

After co-doping DCM1 in a tetracene crystal, the luminescent color was changed from green to red, and EQYs were improved from 1% to 8%, yet the electron mobility decreased from 1.28 to 0.13 cm²V⁻¹s⁻¹.

The absorption coefficient in a tetracene single crystal showed polarization dependent behavior, which results in a similar modulation of photocurrent. From the relationship between absorption coefficient and photocurrent, the exciton diffusion length along the *c* axis was calculated to be 1.87 μm. The diffusion length is longer than the thickness of the bottom layer (0.583 μm) of the bilayer transistor.

The bilayer transistor showed red light emission from the top crystal, which is different from that of pure tetracene (green light emission) as seen in figure 2a. To further prove whether the top crystal can be excited by exciton transfer or photon absorption from the bottom layer, a TTC thin film insulator, which allows photon transport but blocks exciton migration, was inserted between them (figure 2b). Only green light emission was observed in the

device, indicating that there is no light emission in the top layer (figure 2d).

These results have proved our anticipation that excitons transferred from the high-mobility bottom crystal to the top crystal which has higher EQY.

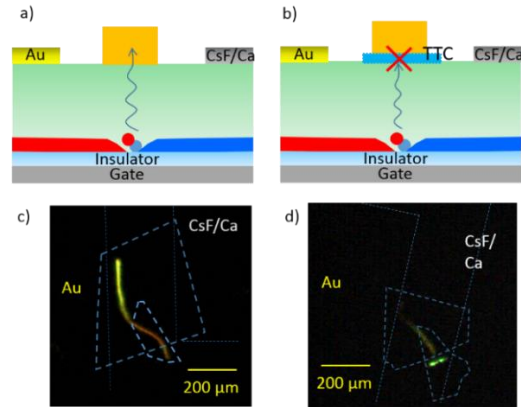


Figure 2. Schematic side-view diagram and top view photography of bilayer transistors (a), (c) without TTC and (b), (d) with TTC, respectively.

Furthermore, the current density in ambipolar region of this bilayer transistor was evaluated to be 532 A/cm², which is 83 times higher than that in BP3T (6.4 A/cm²), and is surely promising for laser.

Conclusions

I fabricated a bilayer transistor based on tetracene and its co-doped crystals, the separation of carrier transport and light-emission function was successfully realized, and the current density which can provide exciton density for population inversion was dramatically increased.

Publication lists

- [1] H. Shang *et al*, submitted to *Adv. Funct. Mater.*
- [2] H. Shang *et al*, to be submitted.
- [3] H. Shang *et al*, *CrystEngComm*, **2012**, *14*, 869.

Abstract

Organic semiconductors recently attract considerable attention for new kind of lasers. They have plastic-like and favorable optoelectronic properties, with prospects for low energy consuming laser. Despite the optically pumped organic semiconductor lasers have been demonstrated since the early history of the laser, electrically driven laser has not been realized. It is still a challenge that sufficient exciton density must be created for population inversion. Exciton density is determined by the mean factor i.e. charge-carrier mobility in organic light-emitting field-effect transistor (LE-FET). On the other hand, high luminescent efficiency is also a crucial factor for realizing lasers that they are capable to reduce the nonradiative losses caused by quenching and supplement the photo absorbed by electrodes.

In particular, the organic field-effect transistors based on semiconducting crystals had demonstrated charge carrier mobility value more than $10 \text{ cm}^2 \text{ V}^{-1} \text{ s}^{-1}$ and showed the intrinsic nature of the organic semiconductors. Moreover, optical properties, especially the luminescent efficiency, related with molecular packing were investigated.

This doctor research had challenged several alternatives, mainly focus on the exciton behavior in organic crystals, to pursuit the electrically driven organic lasers. For example, ASE behavior is due to interaction between photons and excitons; doping which can improve optical property is determined by energy transfer (exciton migration); also, singlet fission and its reverse process i.e. triplet fusion make the exciton diffusion length to be in micro-scale.

To realize laser, investigating gain property is a necessary process because laser contains only a gain media with a resonator. In chapter 3, we focused on specific analysis of gain properties of BP2T, BP2F and BPFT single crystals. By comparing both the absorption and fluorescence spectra of these three co-oligomers in both single-crystalline and deposited thin-film forms, we assigned the dual gain-narrowed peaks corresponding to the vibronic transitions from $S_{1,0}$

to $S_{0,n}$ state. Combining the transient absorption spectra with ground-state absorption spectra, we finally determined that the number of gain-narrowed peaks corresponding vibronic transitions is affected by the re-absorption from both the ground-state and excited-state molecules, and energy distribution of this gain behavior is determined by transition probability from $S_{1,0}$ to $S_{0,n}$ and bleaching of the ground-state absorption. Furthermore, gain with the highest efficiency can be expected when only the vibronic transition with the highest transition probability is confined in the window of absorption at both ground state and singlet state (figure I). This research is not only the first report of the mechanism describing energy efficiency and its distribution but also a good guide to design materials for laser.

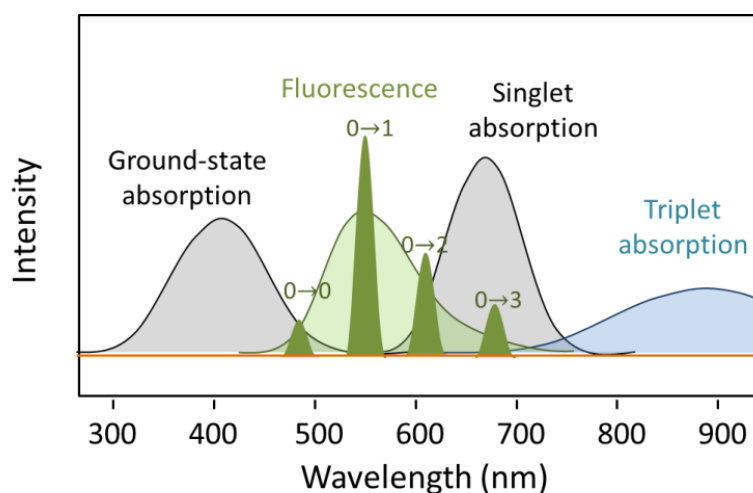


Figure I. Schematic spectra of idealized material with the most energy efficiency. The separated narrowed peaks correspond to vibronic transitions.

In chapter 4, tetracene-doped anthraene crystal is employed as a model for studying doping system based on RET theory. Both the fluorescent spectra and much more improved luminescent efficiency proved that there was an efficient energy transfer from the donor molecule to the acceptor molecule. Furthermore, we have successfully overcome the differences of molecular structures and their stacking modes, finally doped a certain quantity of CNDPASDB into *trans*-DPDSB by solution growth method, and maintained the original crystal structure of host crystal as proved by polarizing optical microscope analysis. Light emission color can be tuned by changing the doping ratio, due to intrinsically high

QY of the host material and efficient energy transfer from *trans*-DPDSB molecules to CNDPASDB molecules. Therefore, emission spectra can cover both the emission region of the host (blue color) and that of the guest (orange color). With suitable balance of the ratio between host and guest, white light emission was successfully obtained. Moreover, superb high EQY (~80%) comparable with that in solution was obtained by doping, and it slightly decreased with increasing the doping ratio due to the singlet-singlet annihilation. Finally, carrier transport characteristic was also investigated in both pure *trans*-DPDSB and its doped crystals. It is concluded that dopant with smaller energy band gap may introduce carrier-traps, which means if the problem of carrier-trap is overcome in the doping system, electrically driven laser may be realized.

As well known that high luminescent efficiency and high carrier mobility cannot coexist in one material. An idea came to us that we can separate these two factors into two layers, and assign the combination of these two layers as active layer. In this case, light-emission and carrier-transport functions can be separated. We fabricated such bilayer FET, and realized the separation of light-emission and carrier-transport functions. In chapter 6, we designed a novel device structure which can separate the carrier-transport and light-emission functions into two crystal layers (see figure II). This device structure can divide the two important yet conflicting factors, high luminescent efficiency and high carrier mobility, making the device promise to realize electrically driven lasers.

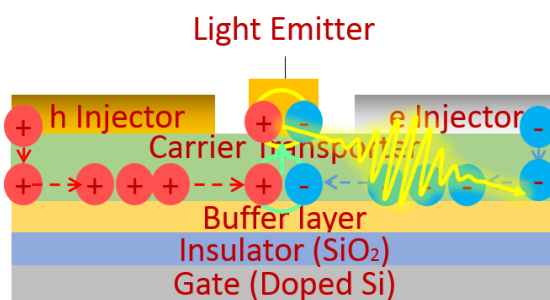


Figure II. Schematic side-view diagram of bilayer light-emitting transistors. Green layer at bottom stands for carrier transporter, top layer act as light emitter.

Mechanism can be described that after electrons and holes accumulation, they will have a recombination to form excitons, the excitons diffuse to the top layer with light emission.

Table of contents

Chapter I	1
Introduction	1
1.1 Backgrounds	1
1.2 Organic Semiconducting Crystals	3
1.2.1 General Properties of Organic Single Crystals.....	3
1.2.2 Methods for Organic Single Crystals Growth.....	4
1.3 Exciton Behavior in Organic Semiconducting Crystals	6
1.3.1 Exciton Generation.....	7
1.3.2 Exciton Behavior	8
1.4 Optical properties of Organic Semiconducting Crystals	9
1.4.1 Luminescence in Organic Single Crystals	9
1.4.2 Organic Single Crystals with High Luminescent efficiency	11
1.4.3 Optically Pumped Lasers	14
1.5 Electrically Driven Organic Lasers	17
1.5.1 Prospection of Electrically Driven Organic Lasers.....	17
1.5.2 Main Issues for Feasibility of Electrically Driven Lasers	18
1.5.3 Approaches for Realizing Electrically Driven OSLs	18
1.6 Research Approach of This Thesis	21
1.6.1 Research Motivation.....	21
1.6.2 Overview of this thesis	22
Chapter II	
Materials and General Experimental Techniques	25
2.1 Materials	25
2.1.1 BP2T, BPFT and BP2F	25
2.1.2 Anthracene and Tetracene	30
2.1.3 <i>trans</i> -DPDSB and CNDPASDB	33

2.1.4	DCM.....	36
2.2	General Experimental Techniques.....	37
2.2.1	Organic Single Crystal Growth.....	37
2.2.2	Optical Properties in Organic Single Crystals.....	39
2.2.3	Fabrication of Organic Single Crystal Transistor.....	40
2.2.4	Measurements of Field-Effect Transistors.....	43
Chapter III		
	Gain Properties of Thiophene/Furan/Phenylene Co-oligomer Single Crystals.....	45
3.1	Introduction.....	45
3.2	Experimental Section.....	46
3.3	Results and Discussion.....	49
3.3.1	Gain-narrowing behaviors.....	49
3.3.2	Reason for dual gain-narrowed peaks.....	51
3.3.3	Energy distribution and efficiency.....	55
3.3.4	Dependence on excitation density and area.....	59
3.3.5	Ideal material for laser.....	62
3.4	Conclusions.....	63
Chapter IV		
	Doped Crystals with Improved Optical Properties.....	65
4.1	Introduction.....	65
4.2	Experimental section.....	67
4.3	Results and discussion.....	69
4.3.1	Tetracene-doped Anthracene crystal.....	69
4.3.2	Optoelectronic properties of CNDPASDB-doped <i>trans</i> -DPDSB crystals.....	72
4.4	Conclusions.....	78
Chapter V		
	Long-Range Exciton Diffusion in Tetracene Crystal.....	81

5.1	Introduction	81
5.2	Experimental Section	82
5.3	Theoretical Basis	84
5.3.1	Polarized Absorption Coefficient	84
5.3.2	Photoconductivity	85
5.4	Results and Discussions	86
5.5	Conclusions	88
Chapter VI		
	Separation of Carrier-Transport and Light-Emission Functions	89
6.1	Introduction	89
6.2	Experimental Section	92
6.3	Results and discussion	94
6.3.1	DCM1-Doped Tetracene crystal	94
6.3.2	Bilayer light-emitting transistor	97
6.4	Conclusions	102
Chapter VII		
	General Conclusions and Future Perspectives	103
7.1	Conclusions	103
7.2	Future Perspectives	105
	<i>References</i>	107
	<i>Curriculum Vitae</i>	115
	<i>Publication List</i>	117
	<i>Acknowledgements</i>	121

Chapter I

Introduction

1.1 Backgrounds

Laser, which is shorten for light amplification by stimulated emission of radiation, is a relatively new artificial light source. It is a device that emits light through a process of optical amplification based on the stimulated emission of photons. The emitted laser light is notable because of the advantages such as its high degree of spatial and temporal coherence, unattainable using other technologies. The demonstration of the first laser, made with ruby in 1960^[1], has led to a revolution in science and technology. Lasers have transformed spectroscopy giving previously undreamed of insights into the physics and chemistry of the world around us, such as the direct observation of the vibrations of chemical bonds.^[2] They are used in a remarkable range of applications ranging from medicine to telecommunications. We now find them throughout everyday life in CD/DVD players, printers and supermarket scanners.

As we know, inorganic lasers are broadly commercially available now, also the combination of design and fabrication expertise, manufacturing infrastructure and strong market position makes this inorganic technologies unbeatable, but what behind these prosperously growth is highly wealthy cost. Inorganic lasers have irreplaceable status because of their sole wavelength and extremely high intensity, but the complex process of fabrication and the non-recyclable active gain materials also cannot be ignored. Facing with the aforementioned problems, organic semiconductors combine novel optoelectronic properties, with simple fabrication and the scope for tuning the chemical structure to give desired features, making them active candidates for laser materials. Especially, organics are a promising candidate for applications of color tunability, large active areas, mechanical flexibility or low-cost processing, as they combine the material properties of plastics with high optical cross-sections, large and ultrafast

nonlinear responses, and broad spectral tunability. In terms of fabrication, they can be solution-processed at low cost, allowing large-area deposition (roll-to-roll or contact printing, for example) on non-standard substrates. In addition, because organics allow dipole optical transitions between confined states, they tend to have large optical cross-sections (typically 10^{-15} cm² for peak absorption)^[3], which provides a distinct advantage when interacting with light in either emission, absorption or non-resonant modulation processes.

Due to the achievement of amplified spontaneous emission (ASE), optically pumped organic semiconductor laser has been demonstrated clearly by some groups; Hide et al.^[4] observed gain narrowing from a optically pumped thin-film waveguide, while Tessler et al.^[5] made the first vertical microcavity laser based on conjugated polymers as gain materials. Subsequently, optically pumped laser action has been demonstrated in a broad range of conjugated polymers and oligomers.^[6]

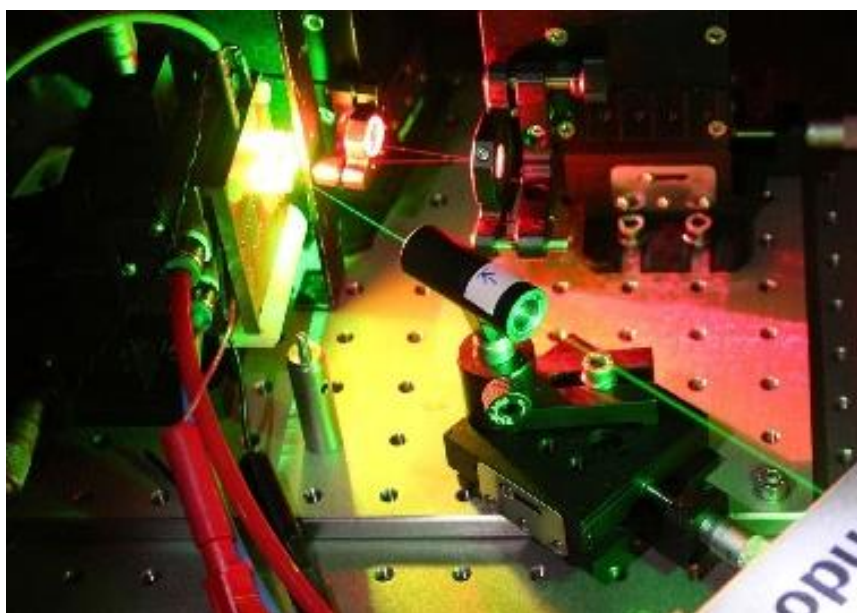


Figure 1.1. Photography of optically pumped organic semiconductor laser

However, electrically driven lasers based on organic semiconductor is still a challenge. Scientists from physics, chemistry as well as materials spared no efforts to realize it, but no one has succeed to date. There are still some criterial to be satisfied. For example, population inversion must be provided by sufficient

current and exciton density, also clear gain-narrowing and threshold behavior must be obtained. Therefore, optoelectronic properties of organic materials treated as candidates for laser must be deeply studied.

Organic semiconducting crystals are treated as good candidates for investigation of optoelectronic property. Due to the highly-ordered molecular aggregation, intrinsic properties of organic materials can be well understood. In this dissertation, based on organic semiconducting crystals, exciton behaviors as forms of gain-narrowed behavior, exciton transfer in doped systems, exciton diffusion length are studied. Finally, a novel configuration of light-emitting device towards electrically driven lasers is fabricated.

1.2 Organic Semiconducting Crystals

The investigation of organic single crystals applying in optoelectronics has caught the eye of scientists since 1960s. M. Pope *et al.* firstly found the electrically driven light emitting of anthracene single crystal in 1963.^[7] Later, optically pumped laser emission in anthracene single crystal and some other doped molecule crystals has been reported.^[8-10] With the development of organic single crystal growth, some organic single crystals with high quality and large enough size have shown superb both optical and electrical properties, therefore become excellent candidates for the active layer roles in OLEDs,^[11-13] OFETs^[14-16] and lasers.^[17-19] Compared with amorphous organic thin films, organic single crystals have countless advantages, such as much higher thermal stability and carrier mobility, superb self-waveguide effect.

1.2.1 General Properties of Organic Single Crystals

Because of the definite molecular structure, long-range order, and absence of grain boundary, organic single crystals offer not only an unique opportunity to investigate the intrinsic charge transport.^[20-22] but also a shortcut to study the optoelectronic properties of the molecule, and become one of the strongest performers in the field of organic semiconductor materials.

Due to the low carrier mobility (10^{-4} - 10^{-5} cm^2/Vs)^[23, 24] in the organic thin film, higher performance in devices has been confined, especially for realizing electrically driven lasers, which demand the density of electrical current to reach the level of hundreds KA/cm^2 .^[25] In the case of organic single crystals, the carrier mobility can be largely improved due to the intrinsic advantages of long-range order, and absence of grain boundary. For example, the FET carrier mobility of rubrene single crystal can reach $20 \text{ cm}^2/\text{Vs}$,^[26] and the density of electrical current in LE-FET device is about $4 \text{ KA}/\text{cm}^2$.^[27] Another example we want to illustrate in this section is the single crystal of 5,5''-bis(bi-phenyl)-2,2';5',2'-terthiophene (BP3T), whose density of electrical current can even reach about $12 \text{ KA}/\text{cm}^2$ when applying 400 V voltage.^[28] If we keep sparing no efforts on improving the contact condition between single crystals and metallic electrodes, the injection of carrier will be improved, also the expedition of improving density of electrical current will be further realized.

1.2.2 Methods for Organic Single Crystals Growth

The growth of high-quality organic single crystals has already been considered as an essential step in integrated research. Various reliable methods have been proposed. Physical vapor transport (PVT) method,^[29] which is already widely used in the field of conjugated oligomers, provides higher surface quality, and can produce crystals suitable for use in FETs.^[30, 31] The schematic diagram of PVT method is illustrated in Fig. 1.7, and the principle will be described in chapter 2.

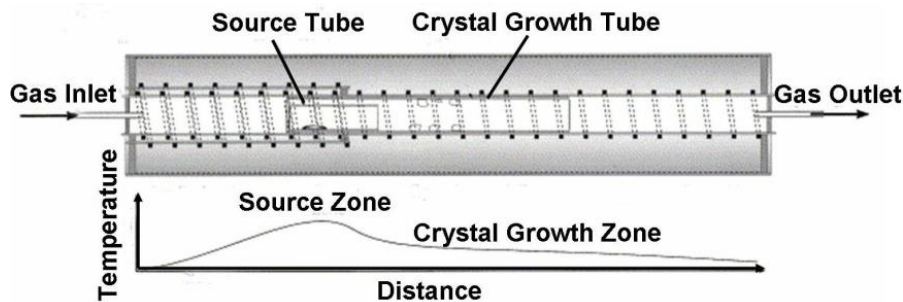


Figure 1.2. Schematics of the crystal growth apparatus for PVT method, and the temperature gradient distribution with distance.

Since the PVT method relies on sublimation of the materials, some good materials may pyrolyze before their phase transition. Provided that a suitable solvent can be found, the solution growth (SG) method is a natural alternative to PVT. Commonly, the level of supersaturation achieved in solution is far lower than that in PVT, allowing a reduction of the nucleation rate and an increase of the size of the crystals.^[32-34]

It cannot be doubted that both of the methods have disadvantages. Besides the aforementioned problem, most of the crystals obtained by PVT method are so thin that they are too brittle to be transferred to the substrates. This problem will cause a significant effect on the further progress in the fabrication of devices. Also for SG method, the solvent may significantly influence the morphology of the crystalline material during the growth process. Consequently, finding an effective method to provide single crystals with perfect morphology and controllable thickness is extremely important.

In my previous research,^[35] I have described a gas–liquid interface crystal growth technique optimized for organic single crystals with superb morphology and controllable thickness. Using this method with carefully selected solvents, we succeeded in growing large organic single crystal sheets. Based on this method for the growth of crystals at the gas–liquid interface, we also obtained crystals firmly attached to a substrate using drop casting (see figure 1.3). The characterization of these samples confirmed that such a gas–liquid–solid method represents a potential candidate for the fabrication of organic single crystal based devices such as light-emitting diodes and field effect transistors.

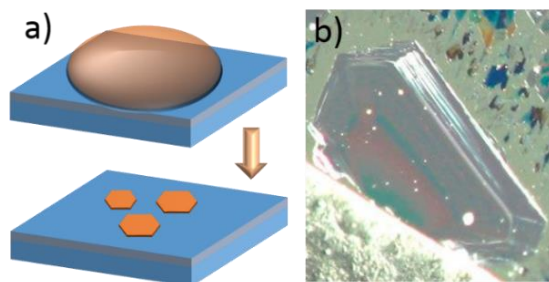


Figure 1.3. a) Schematic diagrams and b) photograph of crystal growth on silicon substrate by using drop-casting method.

1.3 Exciton Behavior in Organic Semiconducting Crystals

There are general three types of excitons (see figure 1.4): Frenkel excitons (also called tight bound excitons) are the excited states of electron and hole that can be localized on the same molecular site moves as a unit through the crystal lattice. The radius of exciton is small ($< 5 \text{ \AA}$), and the molecules are far apart compared with the orbit of electron in the exciton state. Wannier-Mott excitons (also called free excitons), are results from interaction of holes and electrons separated over several atoms. Wannier excitons are most common in inorganic systems, where the interaction energy is great and the dielectric constant is high. Charge-transfer exciton in organic systems are electrically excited, neutral, polar crystal states, the exciton radius is only one or two times the nearest-neighbor intermolecular distance.

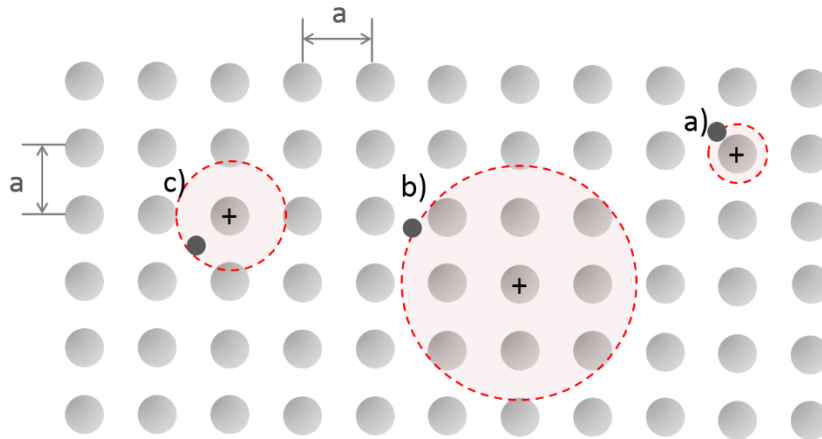


Figure 1.4 (a) The small-radius Frenkel exciton in which the radius R_F is small in comparison with a lattice constant a . (b) The large-radius Wannier-Mott exciton in which the radius R_w is large in comparison with a lattice constant a . (c) the intermedia or charge-transfer exciton, in this case, a nearest neighbor.

In this dissertation, only Frenkel excitons which generated by light illumination or electron-hole recombination will be discussed. The movement of these excitons can be due to the overlapping of orbitals between corresponding

sites. For adjacent molecules of different types, the excitation energy transfer mechanism happens with Forster or Dexter exciton transfer mechanisms.^[36]

1.3.1 Exciton Generation

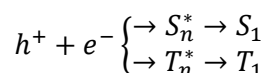
Excitons can be generated in any of the ways that an excited electronic state can be generated. There are many ways to generate the excitons: generation by radiation (light or high-energy ray), by carrier-recombination, or by other excitons and so on.

Direct Optical Excitation

Direct optical excitation is the most convenient way to generate excitons. By choosing the appropriate wavelength of the incident light, a specific exciton can be generated. This exciton will relax to the lowest excited state within a picosecond. A limitation of the optical method is that sometimes the desired state represents a forbidden transition from the ground state. This transition is forbidden caused by molecular aggregation in organic crystals will be discussed afterwards (see 1.3.1).

Generation by Carrier Recombination

The recombination of charge carriers results in electronically excited crystal states via



(Equation 1.1)

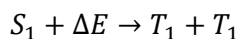
Where S_n^* and T_n^* are highly excited singlet and triplet exciton states and S_1 and T_1 denote lowest singlet and triplet exciton states. It is possible to generate electrons and holes individually, in separated regions of the crystals, and to use an electric field to bring these carriers together. This process is referred to as electroluminescence.

Generation by Indirect Excitation

This process mostly happened in a doped system, in which excitons are generated in host molecules and transferred with a distance to the guest molecules. This process will be studied in detail in chapter 4.

Generation by Other Excitons

Transitions from a singlet state to a triplet state are not spin-allowed, so efficiency of such process is only a few percent. But there are several special cases, for example in tetracene single crystals, one singlet exciton can decay into a pair of triplet excitons. This process is called singlet-singlet fission. This fission of a singlet exciton is a spin allowed process. The equation governing thermally induced singlet fission can be written



(Equation 1.2)

It is also possible for two triplet excitons to fuse upon contact, producing a singlet exciton, and this process is called triplet fusion. The distinguishing feature of the fluorescence from the S_1 state generated by the fusion process is that its apparent lifetime is determined by a two-stage process involving the triplet excitons and hence is much longer than the fluorescence lifetime. This is the reason that triplet fusion is also called delayed fluorescence.

1.3.2 Exciton Behavior

Exciton Relaxation

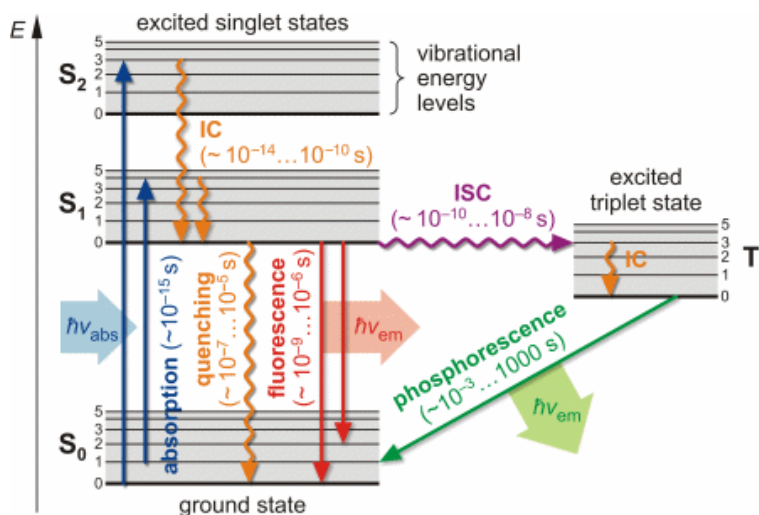


Figure 1.5. Jablonski Diagram which illustrates the electronic and vibrational states of a molecule and the transitions between them.

The excited state relaxes eventually to the ground state, and the time scale for a relaxation depends on the degree of allowedness of each transition to a lower-lying level. This process can be radiative or radiationless. The radiative processes are in the forms of fluorescence or phosphorescence. On the other hand, radiationless process is always in the form of heat.

Förster Energy Transfer

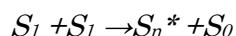
It is also called resonance energy transfer, which is a nonradiative process resulting from long range transition dipole-dipole interactions between the donor and acceptor. In this process, it demands for a nonzero overlap between the fluorescent spectrum of donor and the absorption spectrum of acceptor. Moreover, the separation between donor and acceptor as well as direction of transition dipole are also crucial factors.

Dexter Energy Transfer

Dexter transfer is a fluorescence quenching mechanism in which an excited electron is transferred from a donor molecule to an acceptor molecule via a non-radiative path. This process requires a wavefunction overlap between the donor and the acceptor, which means it can only occur at short distances (typically within 10 Å). The excited state may be exchanged in a single step, or in two separate charge exchange steps.

Reaction with Other Excitons

Besides singlet fission and its reverse process triplet fusion describe the inter-exciton reaction, another process which is much more common is singlet-singlet annihilation.



(Equation 1.3)

As described in equation 1.3, a higher excited state S_n^* is generated in this process, but it will soon relax back to S_1 state.

1.4 Optical properties of Organic Semiconducting Crystals

1.4.1 Luminescence in Organic Single Crystals

It is well known that obtaining organic crystal with high luminescent efficiency is a tough task, which is due to the H-aggregation of the molecules in the crystal. H-aggregation (see Fig. 1.11) is a common type for organic molecular packing in crystal, in which the long axes of molecules parallel with each other, making a strong interaction between the dipoles of the molecules, finally result in an energy splitting of the molecular state. After the energy splitting, the more stable energy level of excited state is optically transition forbidden, making the luminescent efficiency low. Facing with the aforementioned problem, the essential way is tuning the interaction between the dipoles of the molecules, such as enlarging the distance between molecules, or forming a cross-like aggregation (X style), “brick wall” motif (J style) is also an efficient way.^[37]

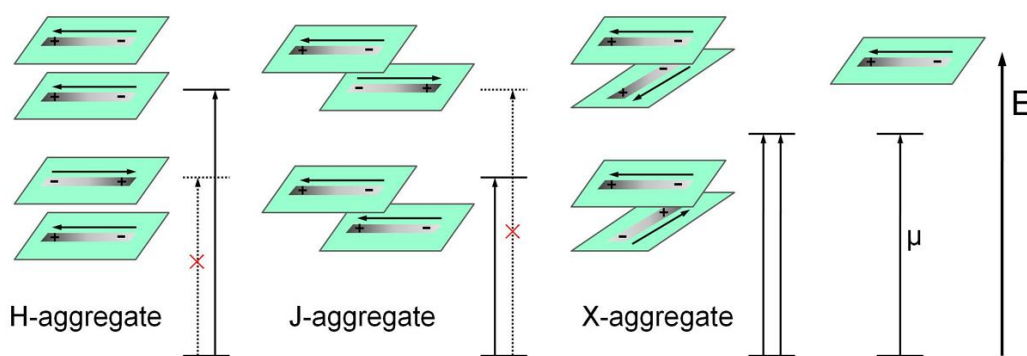


Figure 1.6. Schematics of H-aggregate, J-aggregate and X-aggregate and the energy splitting of the optically allowed transitions of a single chain (left) in configurations.

When we focus on tuning the interaction between the dipoles of the molecules to increase the luminescent efficiency, unexpectedly the carrier mobility decreases because of the less overlap of the conjugated π orbital. It means that J-aggregation is an ideal style in which high luminescent efficiency with high carrier mobility can be realized. Z. Q. Xie *et al.* has designed and synthesized a material *trans*-DFPDSB, the molecular stacking follows the J-aggregation style. In addition, the luminescent efficiency in the single crystal is about 50%, through the theoretical calculation, the crystal shows superb ambipolar behavior with the electron and hole mobility 0.36 cm²/Vs and 0.88 cm²/Vs, respectively.

Another way to increase the luminescent efficiency is electronic doping. Electronic doping is a very efficient way to dilute the concentration of guest

molecules, which can avoid the interaction between the dipoles of the guest molecules to increase the luminescent efficiency. Doped organic molecular crystals have been paid much attention as early as 1970's and stimulated emissions in some systems were observed in succession.^[38] Further in-depth photophysical characterizations of doped systems revealed the relationships between basic optoelectronic functions and molecular structures.^[39]

1.4.2 Organic Single Crystals with High Luminescent efficiency

As we mentioned before, an efficient way to improve the luminescent efficiency is enlarging the molecular distance. A Commonly used method to achieve this aim is introducing larger substituent groups in the main chain, making a space steric for molecular packing. Zhao, C. H. et al. reported a material named 2B2N-DSB^[40] in whose crystal the molecular distance is 8.3 Å (see Fig. 1.7a), and the luminescent efficiency in the single crystal is about 73%. Another example, CNDPDSB^[41], is reported by Ma group, the molecular distance is 6.6 Å (see Fig. 1.7b), and the luminescent efficiency in the single crystal is about 80%.

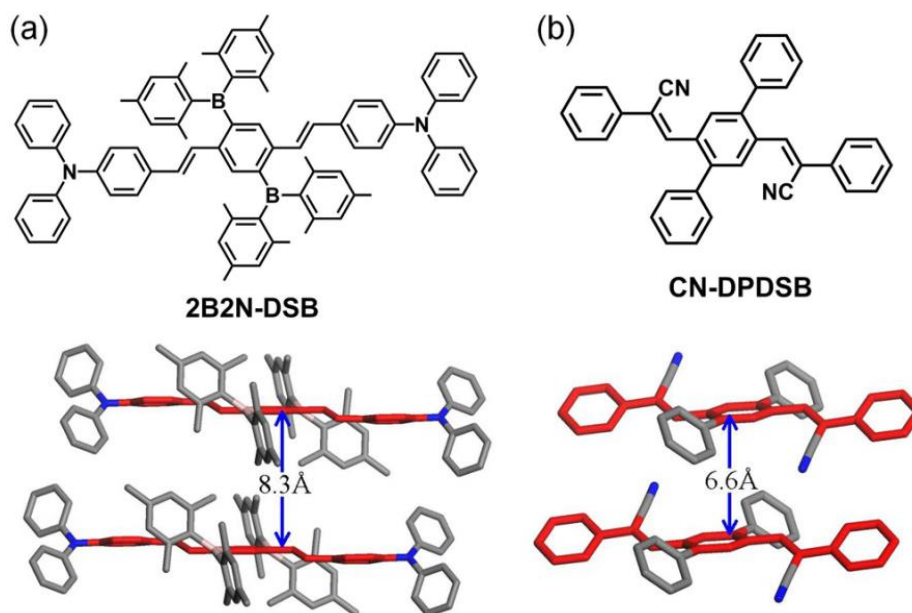


Figure 1.7. Molecular structure and packing mode in crystals of (a) 2B2N-DSB and (b) CNDPDSB, respectively.

In the J-aggregation, as illustrated in Fig. 1.8, the more stable energy level in energy splitting of excited state is optically transition allowed, which can avoid the luminescent quenching happened in the H-aggregation. As we mentioned before, the *trans*-DPDSB crystal obtained from solution is needle-like because of the X-aggregation, while by PVT method, we can obtain slice-like crystal with J-aggregation (see Fig. 1.8a), in which the luminescent efficiency can reach 48%.^[42] Feast, W. J. also reported a J-aggregated material, 10F-DSSB crystal,^[43] and the driven force for molecules forming such kind of aggregation is O \cdots F hydrogen bond between the adjacent molecules (see Fig. 1.8b).

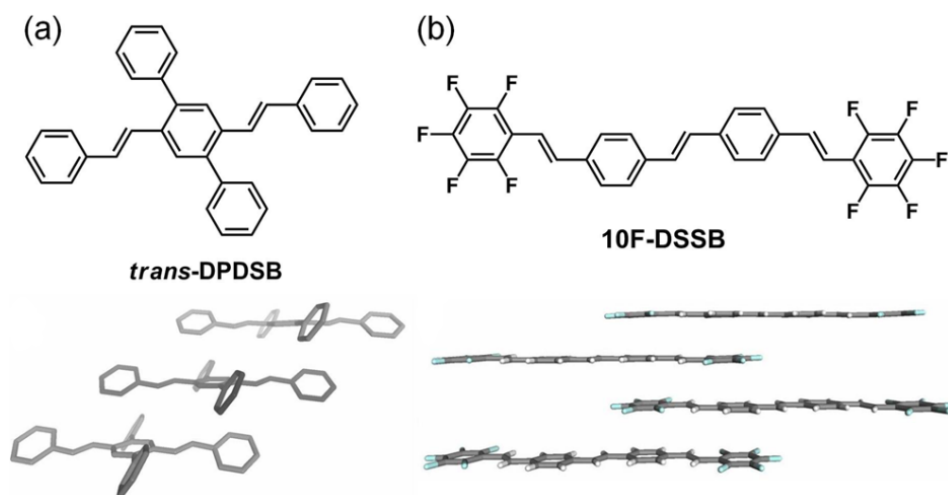


Figure 1.8. Molecular structure and packing mode in crystals of (a) *trans*-DPDSB (obtained from PVT method) and (b) 10F-DSSB, respectively.

Also, X-aggregation can efficiently decrease the interaction between molecular dipoles, benefiting high luminescent efficiency. Though J. Cornil *et al.* has estimated the aforementioned hypothesis through theoretical calculation,^[44] few materials have been reported because it needs special molecular interaction for molecules to form X-aggregation. Ma group reported a material *trans*-DPDSB, whose crystal obtained from solution showed such X-aggregation forming a needle-like shape (see Fig. 1.9a). Affected by the C–H \cdots π interaction between the adjacent molecules, X style of the molecular aggregation is formed with the luminescent efficiency reaching to about 60%.^[45] One year later, N. Sanyal *et al.*,^[46, 47] also reported a material 2O-DEB with X-aggregation in the single crystal, and

the driven force for molecules forming such kind of aggregation is O \cdots H hydrogen bond between the adjacent molecules (see Fig. 1.9b). The luminescent efficiency in crystal was more than 50%.

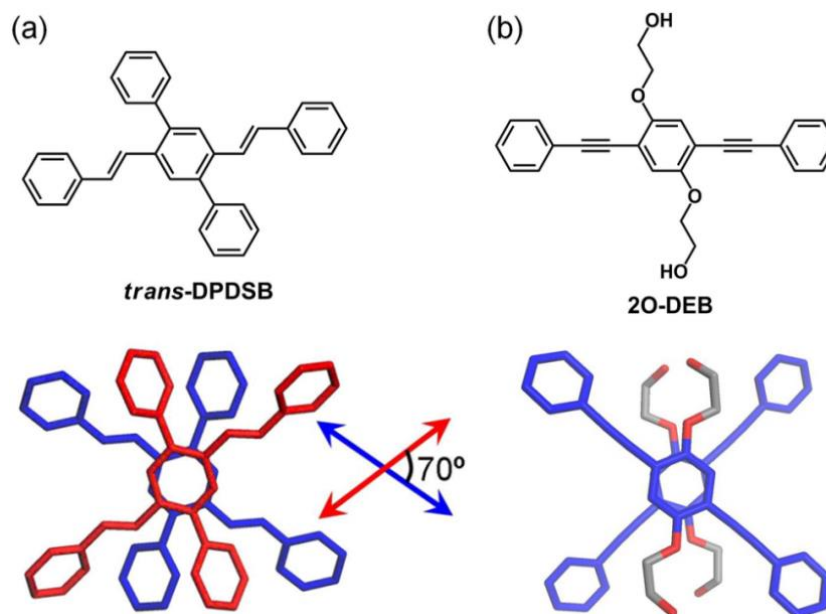


Figure 1.9. Molecular structure and packing mode in crystals of (a) *trans*-DPDSB (obtained from solution) and (b) 2O-DEB, respectively.

For the traditional organic optoelectronic polycene materials such as tetracene, pentacene, it is difficult to get high-luminescent-efficiency crystals and their crystals are hardly applied in electroluminescence or lasers. As we known, doping dye molecules into certain host materials is a general method to increase the luminescent efficiency of the guest molecules for the organic amorphous materials.^[48] Physical vapor transport (PVT) method is the common one to obtain high-quality and large-size organic single crystal,^[31] and based on the principle of structural comparability (including molecular structures and their stacking modes) and spectrum overlap between the host and guest (ensuring efficient energy transfer), Ma group has successfully doped a certain quantity of tetracene or pentacene into *trans*-1,4-Distyrylbenzene (*trans*-DSB) crystal by PVT method, and maintain the structural orderings of doped crystals (see Fig. 1.10). These doped crystals have large sizes, tunable light-emission and high luminescent efficiencies.

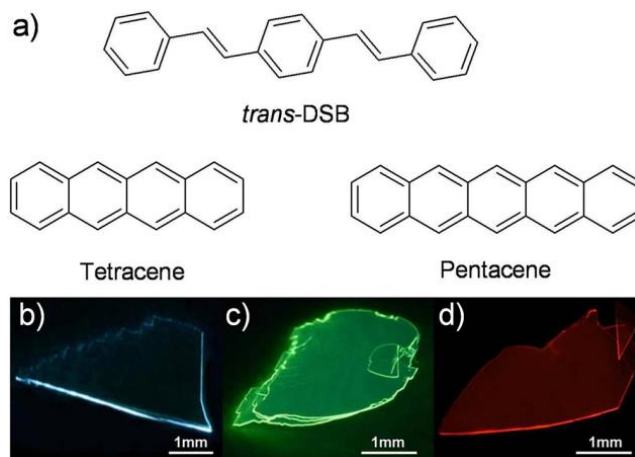


Figure 1.10 (a) The molecular structures of *trans*-DSB, tetracene, pentacene. (b) The pure *trans*-DSB crystal; (c) and (d) Tetracene/Pentacene -doped *trans*-DSB crystals.

1.4.3 Optically Pumped Lasers

A laser consists of a material capable of amplifying light in a cavity (or resonator), which applies feedback. The amplification occurs by the process of stimulated emission. Here, I would like to introduce the origin and properties of the gain in organic semiconductors first. When a photon is incident on a material, it can cause an electron to be excited from a lower to a higher energy level, the process we know as absorption. Similarly, when a photon is incident on a material that has already been excited, it can cause an electron to fall from a higher to a lower energy level and the emission of another photon. This process is known as stimulated emission, and its existence was first proposed by Einstein based on thermodynamic considerations. A crucial point is that the photon emitted has the same phase, frequency, and direction as the incident photon. The fact that an additional photon is released means that there has been amplification of the incident photon. So as light travels through a gain medium, it stimulates the emission of more and more photons and (for small signals) its intensity, $I(z)$, increases exponentially with distance:

$$I(z) = I(z=0) \exp(gz)$$

(Equation 1.3)

where g is the wavelength-dependent gain coefficient of the medium. Einstein showed that for a particular transition, the cross sections for absorption and stimulated emission are the same. This means that in order to get more stimulated emission than absorption at a given wavelength, we need to have more molecules excited to the upper state than are in the lower state, a situation known as a population inversion. The gain coefficient is simply the product of the stimulated emission cross section, σ , and the population inversion density, N , that is, $g = \sigma N$.^[19]

As we mentioned before, optically pumped organic lasers fabricated by single crystals have already been realized for many years. In 1972, N. Karl *et al.*^[8] described a tunable organic crystal laser, in which cleaved platelets of fluorene containing 2×10^{-3} anthracene emitted polarized light pulses at $\lambda = 408$ nm, with a pulse amplitude of 10 W and a pulse duration of ≤ 3 ns, when pumped by a 1 kW nitrogen laser. This process can be simplified as the following description (see Fig. 1.11). Because of the stimulated emission, when a photon passes through an exciton, the electron will drop back to the ground state with another photon emits. The stimulated emitted photon possesses the same phase and frequency as the incident photon. This process will be repeated and multiplied when photons pass through the whole crystal. As the cleaved faces of the crystal parallel with each other, they can be treated as Fabry-Perot resonator and the amplified light will propagate back and forth, making a decrease of the threshold. Then light with laser behavior will emit from the organic single crystal.

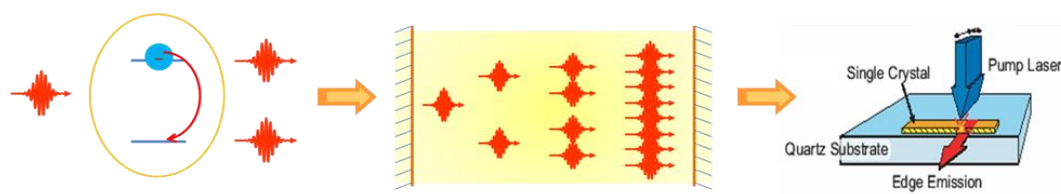


Figure 1.11 Schematic diagram of optically pumped organic laser by using single crystal. First schematic illustrates the stimulated emission process.

In 2005, M. Ichikawa *et al.* reported a P6T single crystal with a natural F-P cavities formed by crystal facets.^[49] The laser emission spectrum showed a

progression of extremely narrow emission lines, and the FWHM of these individual lines is narrowed to 38 pm, with an interval of 121 pm.

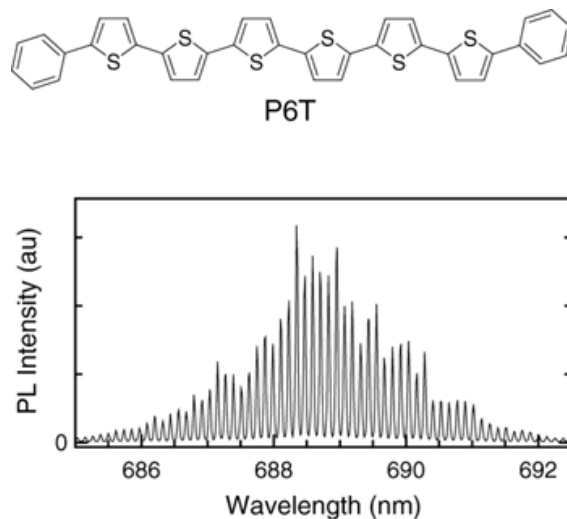


Figure 1.12. Molecular structure of P6T, and its laser oscillator behavior in single crystal form.^[49]

In 2012, X. Li *et al.* also demonstrated the optically pumped organic crystal lasers of CNDPASDB using a symmetric waveguide structure.^[50] Comparing with the ASE from the asymmetric waveguide structure, the threshold is reduced by a factor of 0.38.

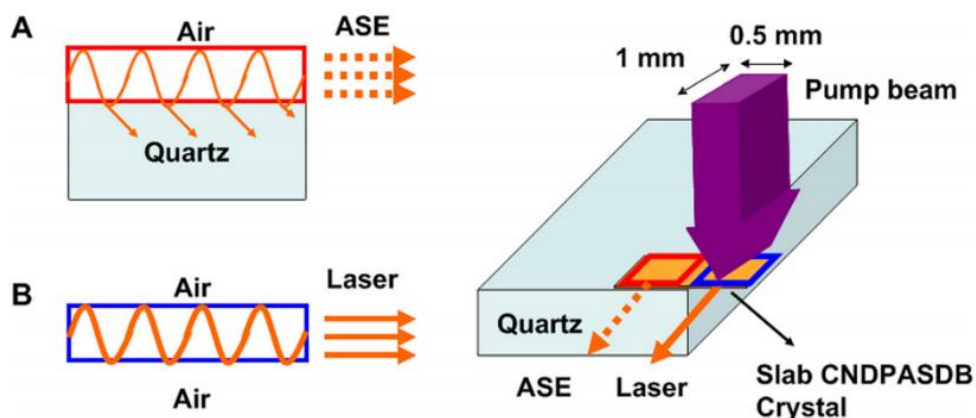


Figure 1.13. Scheme of the structures of waveguide A (quartz/crystal/air) and waveguide B (air/crystal/air), and measurement setup for slab CNDPASDB crystal.^[50]

Moreover, distributed feedback (DFB) directly fabricated in BP2T crystal by using laser interference ablation method was reported by H. H. Fang and his co-workers.^[51] Figure 14c shows the laser spectrum from the DFB BP2T single crystal laser.

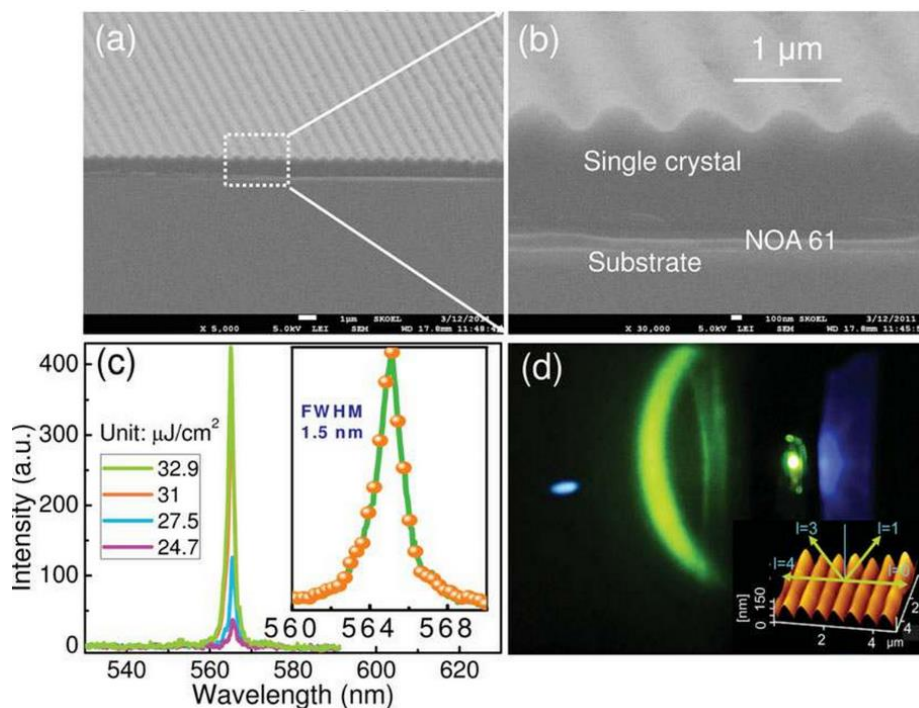


Figure 1.14. (a) and (b) are images of thin film crystals fabricated with 800 nm period grating. (c) Measured spectra of the lasing emission of the laser at different pump influence. (d) Photographs of the operating single crystal laser based on 1D DFB structure.

1.5 Electrically Driven Organic Lasers

1.5.1 Prospection of Electrically Driven Organic Lasers

Almost all the organic semiconductor lasers reported are optically pumped, which means that we need to apply another laser to pump them to reach lasing threshold. This is a cumbersome and expensive configuration that has limited their usefulness. There is, therefore, great interest in developing an electrically driven organic lasers as it would provide a new class of convenient and easy-to-manufacture laser. Such lasers could readily be made in arrays and have

the potential to be tunable, flexible, biocompatible and easily integrated into plastic optoelectronics.

1.5.2 Main Issues for Feasibility of Electrically Driven Lasers

Table 1.1. Main issues to be considered and resolved for optical and electrically driven organic lasers.

Losses	Photo absorption processes	Exciton quenching Processes
Optically Pumped Lasers	Absorption by excitons Self-absorption (defects, low energy states) Mirror losses Waveguide losses	Exciton-singlet annihilation
Additional Electrically Driven Lasers	Absorption at contacts (ITO, metals...) Absorption by polarons	Exciton-contact quenching Exciton-polaron quenching Exciton-triplet Annihilation

Recently, excellent reviewing papers have been published addressing this still open problem of constrains for such a challenging goal.^[6, 19, 52] There are three main key-points to be considered relating to the feasibility of electrically pumped organic lasers, namely, i) the current densities required, ii) the additional losses due to the contacts, and iii) the additional losses due to the injected charges and triplet formation. In table1.1, R. Zamboni *et al.*^[53] have summarized the main issues for both optical and electrically driven organic lasers.

1.5.3 Approaches for Realizing Electrically Driven OSLs

The aforementioned issues are a very challenge problem for the OLED. A typical inorganic semiconductor diode laser operates at a current density of KA cm⁻² whereas a typical OLED works in the range of mA cm⁻². So it is not possible to pass KA cm⁻² through current OLEDs continuously because they would

overheat and be destroyed. This limitation relates to the low charge mobility of OLEDs compared with their inorganic counterparts. Another problem should be On the other hand, organic single crystal based light-emitting field-effect transistors (LE-FET)^[54, 55] are treated as a novel approaches to construct a working electrically driven organic laser, which includes the redesign on the device structure that will have merit both electrically and optically, as well as new material design rules. These single crystal devices have high carrier mobilities (over $1 \text{ cm V}^{-1} \text{ s}^{-1}$). Moreover, this device structure drastically reduce the influences of exciton quenching and photon losses.^[27, 56, 57] Figure 1.15 has illustrated the schematic diagram of LE-FET device structure form the cross sectional view.

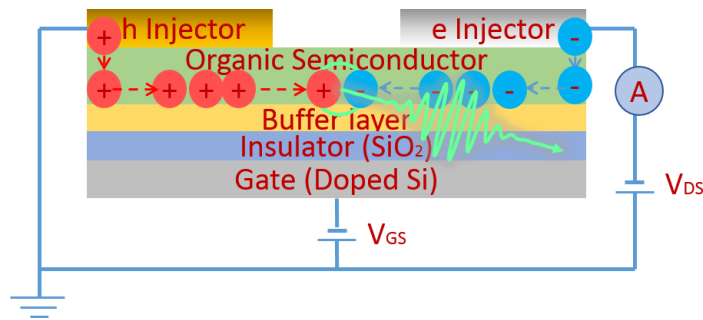


Figure 1.15. Schematic diagram showing light-emitting transistor operation, in which holes and electrons are independently injected from opposing electrodes and accumulated at the interface of crystal and buffer layer; subsequently, they recombine within the conduction channel and with light emission.

From a theoretical viewpoint, pure organic semiconductors should support electron and hole conduction equally.^[58] Ambipolar conduction offers remarkable advantages in LE-FETs: the gate bias minimizes the imbalanced number of holes and electrons, a crucial factor for obtaining high exciton density. Furthermore, gate bias allows us to control the location of the exciton recombination region in the transistor channel to minimize exciton quenching at metal electrodes.

Many groups have spent a lot of efforts on challenging this tough task. Takenobu group reported the spectral evolution accompanied by the spectral narrowing in 2009 (see Fig. 1.16a)^[55, 59, 60], but that narrowing was incomplete (no specific number being given in the literature). They used crystals of 5,5''-bis(4-

biphenyl)-2,2':5',2''-erthiophene (BP3T)^[61] for the organic semiconductor layer. On the basis of the results of a pulsed UV laser excitation they estimated the threshold current density needed for the amplified spontaneous emission and concluded that the current density attained on the LE-FET was two orders of magnitude lower than that for the threshold.

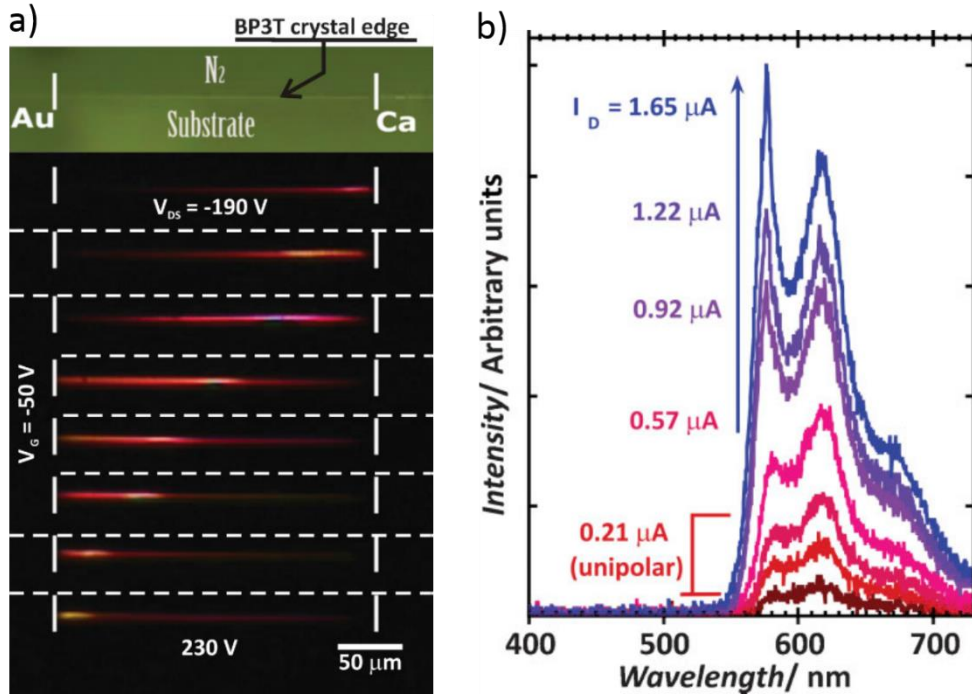


Figure 1.16. a) Edge emission, observed in the horizontal direction, moves by drain voltage (V_D) sweep under ambipolar operation of a BP3T single crystal LET; b) Current-dependent spectral evolution, measured in real time, with 1s time-domain windows, during a drain voltage (V_{DS}) sweep leads to spectral narrowing at a high current regime with brighter emission.

Furthermore, LE-FET with additional resonators were reported by Hotta and Takenobu, both of whom achieved the spectral narrowing emission (SNE) using a feedback configuration (see Fig. 1.17).^[62, 63] However, they did not observe the spectral evolution, which means the narrowed spectra were due to the selection rule of Bragg diffraction law.

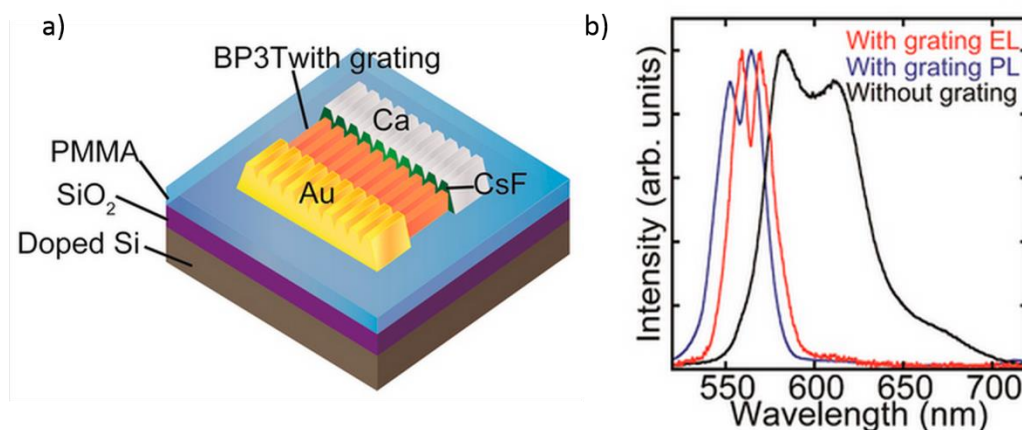


Figure 1.17 (a) Schematic structure of the BP3T SCLET with the 1D grating. And (b) An EL spectrum from a BP3T single-crystal SCLET during ambipolar operation with 350-nm period 1D grating (red line) and a PL spectrum from the same device (blue line). A PL spectrum from a BP3T single crystal without grating is also shown by the black line.^[63]

1.6 Research Approach of This Thesis

1.6.1 Research Motivation

As mentioned above, realizing electrically driven lasers is still a challenge that sufficient exciton density must be created for population inversion. Exciton density is determined by the mean factor i.e. charge-carrier mobility in LE-FETs. On the other hand, high luminescent efficiency is also a crucial factor for realizing lasers that they are capable to reduce the nonradiative losses caused by quenching and supplement the photo absorbed by electrodes.

Based on the aforementioned statement, we found that the exciton behavior in organic semiconducting crystal is a crucial factor for realizing lasers. For example, ASE behavior is due to interaction between photons and excitons, doping which can improve optical property is determined by energy transfer (exciton migration), also, singlet fission and its reverse process i.e. triplet fusion make the exciton diffusion length to be in micro-scale.

To realize laser, investigating gain property is a necessary process because laser contains only a gain media with a resonator. However, there is still some issues not to be determined. For example, some materials show two gain-narrowed peaks

but others show only one, and investigating this reason is one part (chapter 3) of the dissertation.

As well known that high luminescent efficiency and high carrier mobility cannot coexist in one material. An idea come to us that we can separate these two factors into two layers, and assign the combination of these two layers as active layer. In this case, light-emission and carrier-transport functions can be separated. We will fabricated such bilayer FET, and realized the separation of light-emission and carrier-transport functions.

1.6.2 Overview of this thesis

This dissertation is divided into seven chapters that include the overview of the scientific background of the problem; the basic physics foundation and general experimental procedures required for deeper understanding of the whole research process; as well as the results of the detailed study. Several specific experimental studies that strongly correlated are elaborated and discussed. Finally, the drawn general conclusions of this study, which become the main output of this whole scientific process, will be explained.

Chapter 2 introduces the general properties of materials used and general experimental approach in this dissertation. The general physical properties of the materials include crystal structure, carrier mobility and frontier orbitals calculated by using density functional theory (DFT). General experimental techniques, such as single crystal growth, characterization of luminescence efficiency, absorption and fluorescence spectra in ground state, and fabrication route of LE-FETs will be described.

In Chapter 3, we focus on specific analysis of gain properties of BP2T, BP2F and BPFT single crystals. We will investigate the reason for the number of gain-narrowed peaks, as well as the energy competition between them.

In chapter 4, we would like to study energy transfer in a doped system, and focus on the changing of optical properties between pure and doped crystals, such as light emission color, photo-luminescent efficiency and so on.

In chapter 5, exciton diffusion length along c axis of tetracene crystal is studied. Combining the data of polarization-dependent absorption coefficient and photo

current characterizations, we finally obtained the exciton diffusion length along c axis to be in micro-scale.

In chapter 6, based on chapter 4 and 5, we designed a novel device structure which can separate the carrier-transport and light-emission functions into two crystal layers. This device structure can divide the two important yet conflicting factors, high luminescent efficiency and high carrier mobility, making the device promise to realize electrically driven lasers.

Finally, in chapter 7, all of the experimental results are summarized and general conclusion is sort out. From this point, further possible strategies and milestones for the development of real operational electrical driven organic laser will be discussed.

Chapter II

Materials and General Experimental Techniques

In this chapter, we will explain the physical properties of the organic semiconductors used in this research. There are eight compounds, which can be ascribed into four series: thiophene/furan/phenylene co-oligomers (BP2T, BPFT and BP2F), derivatives of oligo(p-phenylene vinylene) (OPV) (trans-DPDSB and CNDPASDB), acenes (anthracene and tetracene) and doping dyes DCM. These materials are selected based on their superior performance in optical properties, electronic transport properties as well as laser capabilities.

The second part of this chapter will explain about the general experiment methods to character the optical properties, including luminescence efficiency, absorption spectra in ground state, fluorescence spectra, as well as processes of fabricating field-effect transistor.

2.1 Materials

2.1.1 BP2T, BPFT and BP2F

As I described in Chapter 1, our group has designed and synthesized new series of materials based on BP2T^[64] in the aim of realizing electrically driven laser.^[65] These three materials have similar molecular structure, which is a good way to have a comparative characterization among them. They can also give us a clue when we design new materials for realizing electrically driven lasers. Also we want to investigate how the optoelectronic properties change when the thiophene

units replaced by similar analogue of furan units one by one. In this part, I will introduce the materials: BP2T, BPFT and BP2F. Also I will illustrate how the physical properties change among these three materials.

2,5-bis(4-biphenyl)bithiophene (BP2T) is one molecule that is a member of thiophene/phenylene co-oligomers (TPCO) family. TPCO family^[49, 55, 66, 67] is a set of molecules which are built from series of thiophene and phenylene rings, connected with simple C-C bonds. This kind of co-oligomers has demonstrated higher mobilities in the thin film transistors in comparison with oligothiophenes molecules. They are characterized by variations of π -conjugation extension along the molecular back bone and take variations in molecular shapes (straight, bent or zigzag), depending on the arrangement of the thiophene and phenylene rings. Several molecules from this family are known to support laser capability.

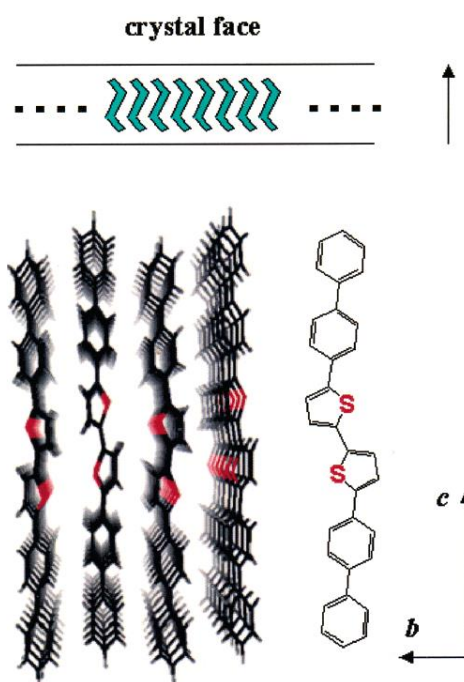


Figure 2.1 Face-to-face molecular stacks of BP2T viewed along the x -axis. Sulfur atoms are marked red. The upper inset schematically represents in a cross section the perpendicular disposition of the molecules (depicted as thick zigzags) in a flake crystal. Its crystal faces and the molecular long axis are indicated with two horizontal lines and a vertical arrow, respectively. The arrow and lines cross each other nearly at a right angle.

The BP2T molecule is categorized as the zigzag form of molecules.^[68] The core has two thiophene rings, which are capped with biphenyl ligands at both ends. It crystallized in a monoclinic lattice with a space group of $P2_1/c$ with a unique b -axis and four molecules inside a single lattice. The BP2T crystal is also characterized as a molecular layer structure for every half lattice, in which the molecules form a herringbone (angle of 61.0°) spreading along the ab -plane. Fig.2.1 displays the face-to-face molecular stacks of BP2T that develop along the a -axis. This figure schematically depicts the perpendicular disposition of the molecular long axes. The thiophenes core and the biphenyl wings individually form columns.

Table 2.1 BP2T lattice parameter

Parameters	Values
formular	C ₃₂ H ₂₂ S ₂
formula weight	470.65
crystal class	Monoclinic
space group	$P2_1/c$ (No. 14)
color of crystal	pale yellow
cell constants	
a (Å)	5.7081 (7)
b (Å)	7.6036 (3)
c (Å)	52.869 (7)
\hat{a} (deg)	97.147(6)
V (Å ³)	2276.8 (4)
D_{calc} (g/cm ³)	1.373

About our newly synthesized materials, BP2F possesses a zigzag form of molecule, while BPFT shows bent form because of the asymmetrical molecular structure.^[65] Figure 2.2 illustrates the simulative molecular structures in crystal of BP2T, BPFT, BP2F, respectively, by using DFT method.

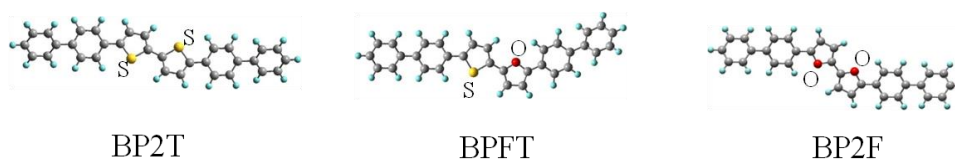


Figure 2.2 The simulative molecular structures in crystal of BP2T, BPFT, BP2F, respectively.

Further characterizations like carrier mobility also have been done by our group. By using the classical ambipolar FET device structure, we have obtained the carrier mobilities of these three materials. Figure 2.3 illustrates the bottom-gated top-contact FET device structure. Here, a SiO₂/Si substrate is used as the gate electrode; PMMA coating layer provides nearly trapless interface; calcium (Ca) is used as source electrode and gold (Au) is used as drain electrode.

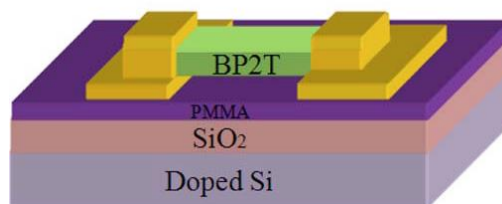


Figure 2.3 The bottom-gated top-contact FET device structure.

Furthermore, we have calculated the carrier mobilities from the results of single crystal FET characterization that BP2T has the hole mobility at the value of $2 \times 10^{-2} \text{cm}^2 \text{V}^{-1} \text{s}^{-1}$, and the electron mobility is $4 \times 10^{-4} \text{cm}^2 \text{V}^{-1} \text{s}^{-1}$. As for the other two newly synthesized material, BPFT and BP2F, the hole mobilities has a obvious increase (BPFT: $\mu_{\text{hole}} = 5 \times 10^{-2} \text{cm}^2 \text{V}^{-1} \text{s}^{-1}$ and BP2F: $\mu_{\text{hole}} = 12 \times 10^{-2} \text{cm}^2 \text{V}^{-1} \text{s}^{-1}$), while for the electron mobilities, it shows decreased tendency that μ_{electron} of BPFT single crystal is $1 \times 10^{-4} \text{cm}^2 \text{V}^{-1} \text{s}^{-1}$, and unfortunately we cannot obtain the electron mobility value of BP2F. Here, what we want to emphasize is that because of the absent device fabrication technique, the value of electron mobility is about two orders lower than the common value obtained by other groups, but the tendency of our results is convincing enough to reach the conclusion that after the

substitution of furan units one by one, the hole mobility decreases while the electron mobility increases.

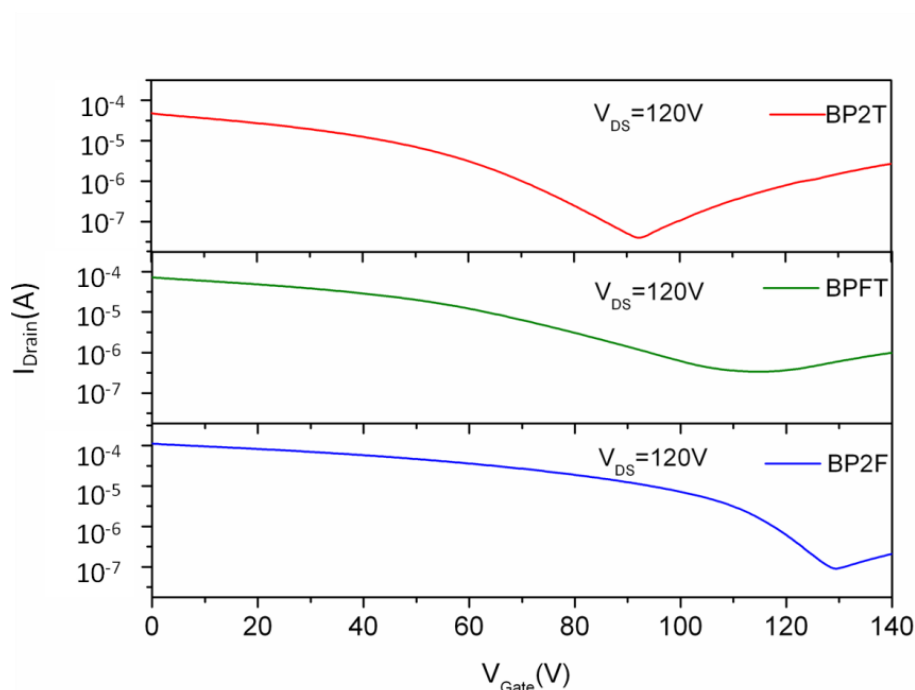


Figure 2.4 The carrier (both electron and hole) injection curve of BP2T, BPFT, BP2F crystals, respectively.

To investigate the tendency change of carrier mobility after substitution by furan units, we have calculated the frontier orbitals of these three materials by DFT method at the B3LYP/6-31G**, (details have been illustrated in Fig. 2.5). We also illustrate the work function of the source and drain metal electrodes as a comparison. The highest occupied molecular orbitals (HOMOs) has an increasing tendency among BP2T (-4.98 eV), BPFT (-4.90 eV) and BP2F (-4.83 eV), which means the injection of hole become easier comparing the work function of gold (source electrode) which is about -5.10 eV. We also believe that because of the increase tendency of HOMO level, the effect of hole-trappers like impurities and defects are effectively whittled. On the other hand, the lowest unoccupied molecular orbitals (LUMOs) also show an increasing tendency of BP2T (-1.98 eV), BPFT (-1.84 eV) and BP2F (-1.68 eV), which brings a difficulty for electron injection, plus the increasing disturbance of electron-trappers near LUMO level, the mobility of electron therefore have a decrease tendency. We also note that the

energy gap of these three materials also shows increasing tendency (BP2T: 3.00 eV, BPFT: 3.06 eV and BP2F: 3.15 eV), which can be attributed to less π -conjugation of furan unit.

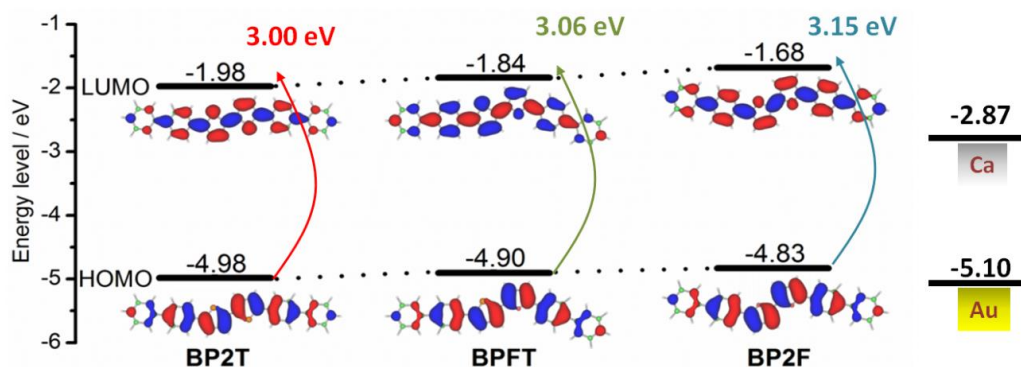
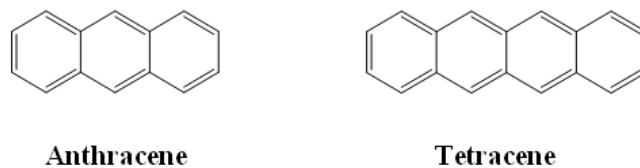


Figure 2.5 The energy diagram of frontier orbitals of BP2T, BPFT, BP2F molecules, respectively, calculated by DFT method at the B3LYP/6-31G**.

In chapter 3, we will have a comparative characterization of optical properties among the aforementioned materials, BP2T, BPFT and BP2F single crystals towards organic electronic organic lasers. In addition, we will analyze the gain property by both ASE and transient absorption characterization, by which we have solved a pendent problem raised for more than 20 years. As we mentioned before, this comparative research will have a great contribution for molecular design, give us a clue to realize organic electronic organic semiconductor lasers.

2.1.2 Anthracene and Tetracene

Both anthracene and tetracene belong to acenes (or polyacenes) which are a class of organic compounds and polycyclic aromatic hydrocarbons made up of linearly fused benzene rings. The larger representatives have potential interest in optoelectronic applications and are actively researched in chemistry and electrical engineering. Scheme 2.1 illustrates the molecular structures of these two materials.



Scheme 2.1. Molecular structures of anthracene and tetracene.

Table 2.2. Cell Parameters of anthracene and tetracene crystal structures.

	a (Å)	b (Å)	c (Å)	α (°)	β (°)	γ (°)
anthracene	8.55	6.02	11.17	90	126.6	90
tetracene	7.90	6.03	13.53	100.3	113.2	86.3

Table 2.2 and figure 2.6 illustrate cell parameters and crystal structures of both anthracene and tetracene.^[70] Anthracene crystallizes in space group $P2_1/a$, and tetracene has space group $P\bar{1}$, but the structure has a symmetry close to $P2_1/a$. Both of the two material show herring-bone aggregation in their crystalline state.

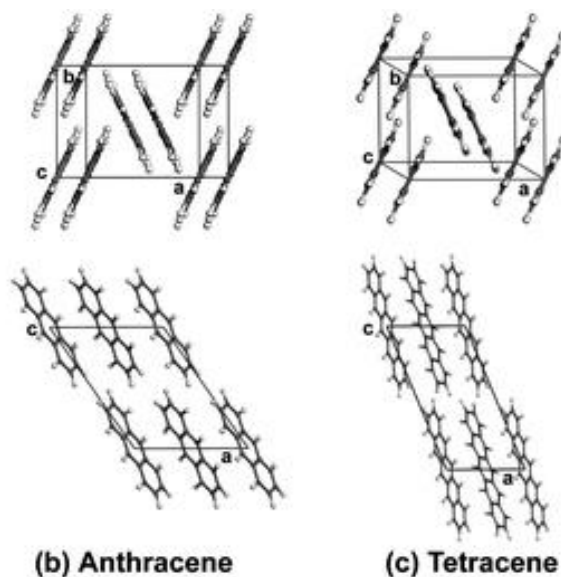


Figure 2.6. Crystal structures of anthracene and tetracene.

Anthracene

Anthracene single crystal with peculiar optical and electronic properties might be the first organic crystal attracted much attention and has been a long-time

subject of the solid-state studies.^[70] The structure–property relationship has been well-established. It was reported that the optical and electronic properties of anthracene solids depend on a number of factors, such as the ordering of molecular arrangement, the structural defects, the existence of trace impurity and/or doped guest molecules, and the dimension of anthracene solids. Furthermore, fast radiative recombination on a nanosecond timescale corresponding to a very small diffusion length of 10–50 nm was determined by Y. Nozue.^[71-73]

On the other hand, anthracene is a molecular solid with a band energy gap E_g : 3.9 eV composed of molecules which held together by weak van der Waals forces, thus it has rather low melting points, 217 °C and poor electrical conductivity.^[74] The charge carrier transport in anthracene single crystals by means of field-effect transistor structure was studied by A. N. Aleshin and his co-workers.^[75] The FET mobility revealed the non-monotonous temperature dependence with the maximum mobility about $0.02 \text{ cm}^2\text{V}^{-1}\text{s}^{-1}$. The space-charge-limited current was determined the dominant transport mechanism in FET structures based on anthracene single crystals.

Meanwhile, tetracene doped in anthracene is a superb good model for studying exciton behavior.^[76-81] In chapter 4, exciton behavior in tetracene-doped anthracene crystal will be studied for understanding doping system.

Tetracene

As mentioned before, tetracene is treated as an excellent dopant for enhancing photo-luminescent efficiency. On the other hand, tetracene single crystal itself is also treated as a good media for optoelectronics study. For instance, tetracene single crystal is the most thoroughly investigated for singlet fission. The notion that singlet fission represents a decay channel for singlet excitons in tetracene single crystal was first proposed in 1968.^[82] Much subsequent work of tetracene crystal has supported the notion that both the fission of the singlet exciton into two triplet excitons and the reverse process of fusion of two triplet excitons into one singlet exciton are fast at room temperature.^[83] As for the electronic transport characteristic, Figure 2.7 illustrates ambipolar light-emitting transistor based on tetracene fabricated by T. Takahashi *et al.* in 2007.^[54] In 2008, T. Takenobu *et al.* reported a tetracene crystal based light-emitting FET,^[27] the mobilities for hole

and electron are 2.3 and $0.12 \text{ cm}^2\text{V}^{-1}\text{s}^{-1}$, which was treated as comparable with those of rubrene. Furthermore, they investigated the current-density dependence of external quantum yield in single-crystal light-emitting transistors. High current and exciton densities were realized in the ambipolar region mobility in both tetracene and rubrene single crystals. In chapter 5, exciton diffusion length in tetracene single crystal was studied based on the theory of singlet fission and its reverse process. In chapter 6, bilayer light-emitting FET towards electrically driven organic lasers was fabricated, and the active layer was based on tetracene single crystal.

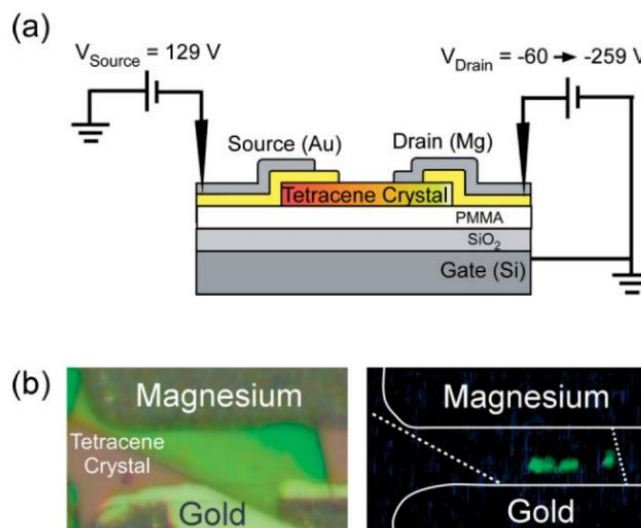
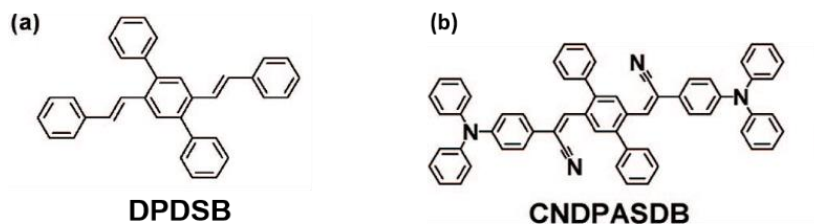


Figure 2.7. a) Schematic representation of a bias condition for light-emitting experiments. b) CCD images of a tetracene single-crystal transistor in the light (left) and in the dark (right). The white solid and dotted lines serve as visual guides.

2.1.3 *trans*-DPDSB and CNDPASDB

Oligo(*p*-phenylene vinylene) (*OPV*) derivatives are treated the most promising materials for realizing electrically driven organic lasers, and these oligomers compose one important class of building materials for laser crystals.^[84] They possess superb high PL quantum yields as high as 80%, also self-waveguide effect is also excellent in some of their single crystals due to the uni-axis molecular aggregation.^[41, 46, 85]



Scheme 2.2. Molecular structure of (a) *trans*-DPDSB and (b) CNDPASDB

trans-DPDSB

It was reported that *trans*-DPDSB (2,5-diphenyl-1,4-distyrylbenzene with two *trans* double bonds) crystal was the first example of cross dipole stacking of conjugated molecules in solid states, and the molecular packing mode led to a needle-like crystal morphology.^[43]

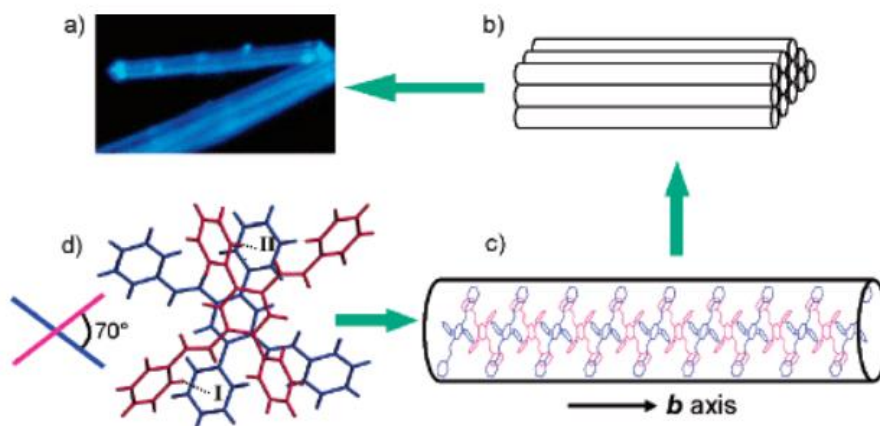


Figure 2.8. (a) Crystals of *trans*-DPDSB under UV light (365 nm). (b) Stacking of 1D molecular columns. (c) Cross-stacking molecules in 1D molecular column. (d) Schematic of the aromatic CH/ π hydrogen bonds between two adjacent molecules. Interaction distances for I and II are 3.08 and 2.67 Å respectively. Conformation 1 is drawn in blue and 2 in red.

In our recent research, we investigated morphology of *trans*-DPDSB crystals by using transmission electron microscope (TEM), and size-controllable crystal can be obtained by controlling the time of crystal growth (see figure 2.9). Furthermore,

amplified spontaneous emission (ASE) threshold are much decreased from reported 680 $\mu\text{J}/\text{pulse}$ (corresponding to 13600 $\mu\text{J}/\text{cm}^2$) to 238 $\mu\text{J}/\text{cm}^2$.

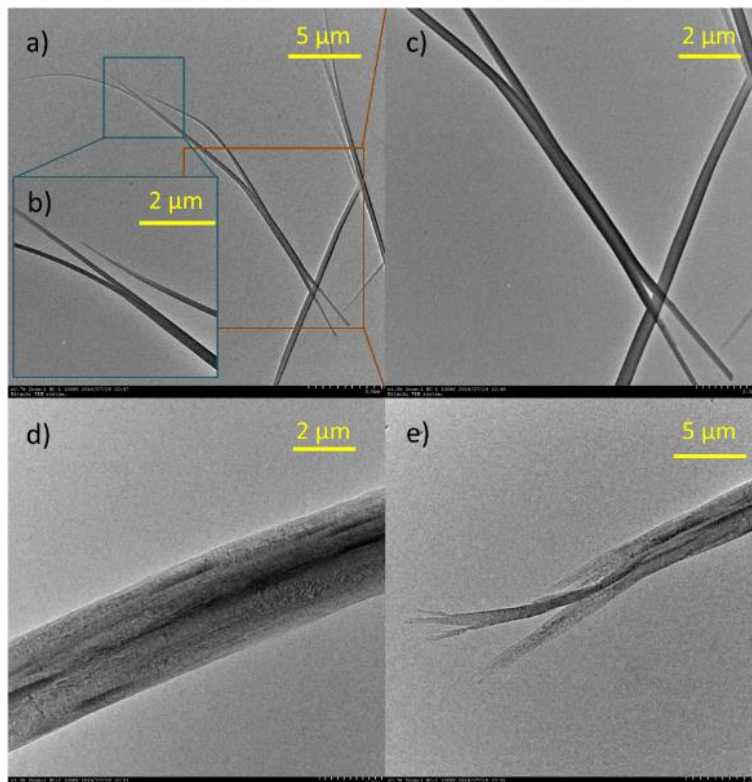


Figure 2.9. TEM profiles of *trans*-DPDSB crystals: Crystals in (a), (b) and (c) were taken out 22 hours after solvent prepared; Crystal in (d) and (e) was taken out seven hours later than (a).

CNDPASDB

Due to the size-controllable characteristic, *trans*-DPDSB as host matrix with attractive crystal structure that the molecules are packed in one-dimension along the b axis can make doped crystals intrinsically form into nano/microwires. From the CIE (Commission Internationale de l'Eclairage) chromaticity diagram, blending an orange or a yellow dye into blue matrix is treated as a brilliant method not only for tuning the light emission but with which white luminescence can also be achieved. Therefore, a material with orange light emission, cyano substituted oligo(*p*-phenylene vinylene)1,4-bis(R-cyano-4-diphenylaminostyryl)-2,5-diphenylbenzene (CNDPASDB), was chosen as luminescence center.^[85] In

chapter 4, we have successfully overcome the differences of molecular structures and their stacking modes, finally doped a certain quantity of CNDPASDB into *trans*-DPDSB by solution growth method, and maintained the original crystal structure of host crystal as proved by polarizing optical microscope analysis. These doped 1D crystals have ultra-long size, high luminescent efficiency (~80%) and color tunable light emission.

2.1.4 DCM

4-(dicyanomethylene)-2-methyl-6-(*p*-dimethylaminostyryl)-4H-pyran (DCM) is always used as a dopant in OLED for increasing the external quantum efficiency (EQE). R. Capelli *et al.* reported a multilayer light-emitting transistor, in which DCM was doped into host *tris*(8-hydroxyquinolato)aluminium (Alq_3).^[56] The devices were >100 times more efficient than the equivalent OLED, >2× more efficient than the optimized OLED with the same emitting layer and >10 times more efficient than any other reported OLETs. In chapter 6, we fabricated a bilayer FET, and DCM-doped tetracene crystal are employed as top crystal in the purpose of light emission.

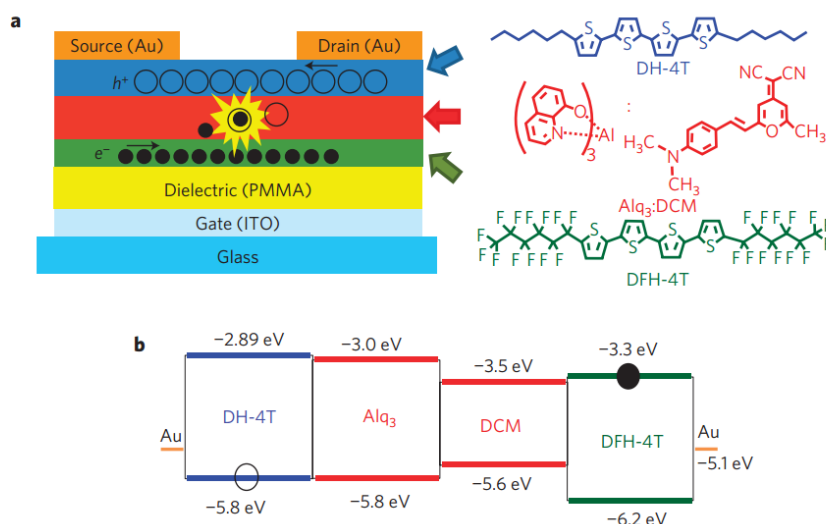


Figure 2.10. a) Schematic representation of the trilayer OLET device with the chemical structure of each material making up the device active region. b) Energy-level diagram of the trilayer heterostructure.

2.2 General Experimental Techniques

2.2.1 Organic Single Crystal Growth

In this research, most of the organic single crystals (chapter 3 and chapter 5) were grown by using physical vapor transport (PVT) method.^[31, 56] This method are preferred for growing organic single crystal for electronic applications, because the highest purity of the produced crystals. We used the PVT in horizontal tube configuration.^[31] The schematic of this system is drawn in figure 2.11. The furnace we used has three heating zones, which can make the temperature curve change more smoothly. The material source was placed in the area where the temperature was set higher, and the crystals grow in the area in lower temperature. Pure argon gas was used as the carrier gas.

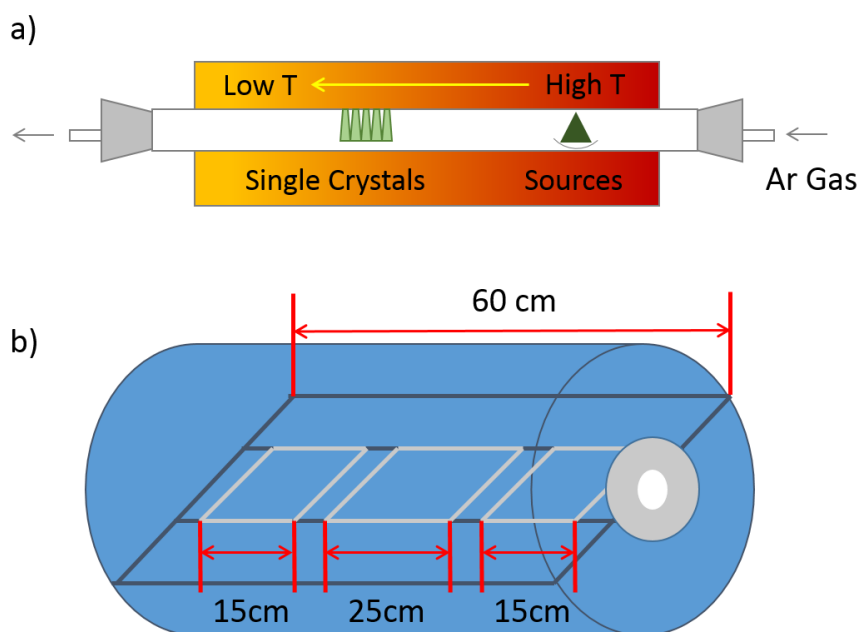


Figure 2.11 Schematic diagrams a) showing the process mechanism of crystal growth by using PVT method and b) three-zone furnace applied in PVT method of crystal growth.

The principle behind the PVT method is that the source material (powder) is evaporated through thermal and the flow of the carrier gas. Source material was heated up close to its sublimation point. And then, the flow of the carrier gas

created lower surface pressure on the source material and increased the vapor pressure of the material. Subsequently, the surface of the material will sublime, as the surface sublimation temperature will be decreased. In addition to initial gas flow (forced convection), buoyancy driven convection also occurs in the tubes as a result of applied temperature gradient from the hot zone to the cold zone. The combination of these two convection process are advantage in carrying away impurities and decomposition products. Even buoyancy-driven convection alone is actually enough to transport the mass of deposited crystals. The organic gas molecules start condensing when it enters the crystallization zone. Nucleation process was assisted by gravity and mostly happened on the zone wall. Thin needle-like or platelets of single crystals are produced by this method. The travel distance of the molecules is also determined by the molecular mass, gravity and molecular viscosity relative to the surrounding. Therefore, impurity materials or decomposed species of the can be separated from the re-crystallization zone. In most of the case, these impurities can be observed nearby the cold end of the tube.

Table 2.3 Tabulation of the optimized crystal growth conditions

Materials	PVT $T_{\text{zone-1}}$ (°C)	PVT $T_{\text{zone-2}}$ (°C)	PVT $T_{\text{zone-3}}$ (°C)	Q.Ar ($\text{cm}^3 \text{min}^{-1}$)
BP2T	240	275	365	46
BPFT	250	280	365	40
BP2F	260	285	330	42
Tetracene	215	150	120	46

We note that BP2T and BPFT have platelet-like shape, while BP2F shows both platelet-like shape and needle-like shape. What we use for research are all in platelet-like shape. Here, we want to emphasize that for BP2F, crystals in both the platelet-like shape and needle-like shape have the same fluorescent spectra, which means they are in the same crystal structure, and platelet-like crystals are the predecessor of the needle-like crystals. Tetracene and DCM-Doped Tetracene crystals reported in chapter 5 are also obtained by using PVT method.

2.2.2 Optical Properties in Organic Single Crystals

Luminescent Efficiency

As we mentioned before, luminescent efficiency in crystal is a crucial factor for the active layer of LE-FET to realize electrically driven organic lasers, which can supplement the losses of photon cost by exciton annihilation and electrode absorption. This is the reason why materials in active layer of LE-EFT device must have high enough luminescent efficiency.

Figure 2.12 has illustrated the photo of integrating sphere which is used for luminescent efficiency characterization. After crystal growth, we collected the crystals with superb quality and put them in a cylindrical quartz container. Then the container was put in the integrating sphere. The schematic diagram of integrating sphere is illustrated in figure 2.12b. With excitation light (blue beam) from light source illuminating on the samples, emission lights (red beams) from the samples in each direction will be reflected by the sphere wall and finally be collected by the detector.

After everything was settled down, both absorption and fluorescent spectra will be measured. The cross section ratio of fluorescent spectra and absorption spectra is just the luminescent efficiency.

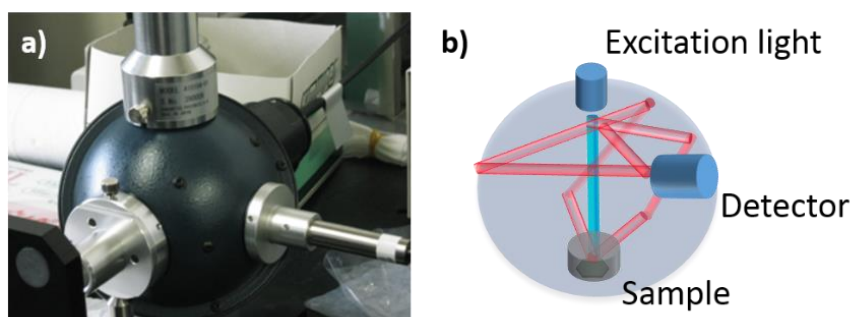


Figure 2.12. Photograph and schematic diagram of integrating sphere for luminescent efficiency characterization.

Absorption and Fluorescent Spectra

Because of the interaction between electronic state and vibration state, vibronic state is the unique character of organic single crystals. From the absorption and

fluorescent spectra, we can detailedly investigate the optoelectronic property of the organic materials.

The absorption spectra were obtained from ultraviolet-visible spectrophotometer (Shimadzu: UV-3100). By using methanol, the samples (single crystals) were attached on a quartz substrate which cannot absorb light. Fig. 2.13 illustrates the schematic diagram of the double beam spectrophotometer.

The fluorescent spectra were obtained from fluorescent spectrophotometer (Shimadzu: RF5301PC). Crystals with superb quality were collected and put in a cylindrical container. Wavelength of excited light was chosen as 380nm.

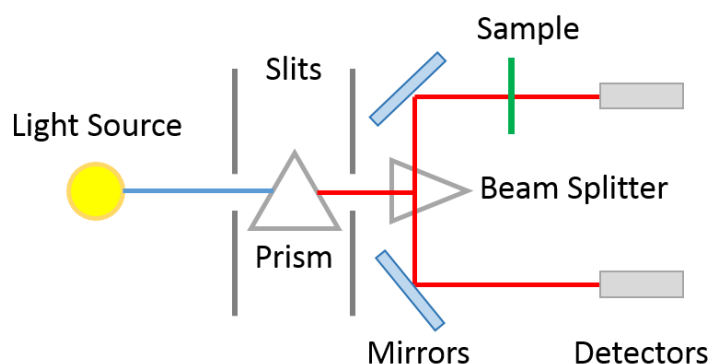


Figure 2.13. illustrates the schematic diagram of the double beam ultraviolet-visible spectrophotometer.

2.2.3 Fabrication of Organic Single Crystal Transistor

The design for ambipolar light-emitting transistors of organic single crystals has been optimized in the last decade years. The most difficult issue is pick-up a single crystal and laminated it on substrates. In our experiment, crystals were pick up by using horse hair tip due to electrostatic effect,^[86] which reduced the chance to damage the crystals during transfer. Moreover, bottom gated with dielectric substrate which able to provide enough carrier density and survive high voltage application was employed.^[87, 88] Here, a thermally SiO₂/Si wafer is a commercially available substrate that is suitable for this purpose where single crystal can be laminated on. The reason behind the application of top contact

electrode is because this contact relationship can assist better charge carrier injection.

Firstly, procedure of preparing substrate for ambipolar device is introduced. A 300 nm thick SiO_2 on metal-like n-type silicon substrate (100) was used as the platform of the device. A polymethylmethacrylate (PMMA, $M_w=120\,000$) was used as a buffer layer. SiO_2/Si substrate was cleaned by using the method of bath ultrasonication with acetone and 2-propanol solvents alternately. Two times later, the fatty dirt was able to be removed. A PMMA solution was prepared by dissolving 8 mg PMMA into 5 ml toluene, so the concentration was 0.18% (wt). This PMMA solution was spin-coated onto the prepared silicon substrate by using a programmable spin-coater. Two steps spinning were performed: 2500 rpm for the initial 5 s after solution dropping, continued by 5000 rpm for the subsequent 45 s. the coated substrate was annealed overnight on a covered hot-plate at 75 °C in order to remove the remaining toluene solvent in PMMA film. Films with thickness of 5-10 nm can be obtained finally. The grown organic single crystal was laminated on top of prepared PMMA/ SiO_2/Si substrate by using an electrostatic bonding lamination method. The processes are illustrated in figure 2.14.

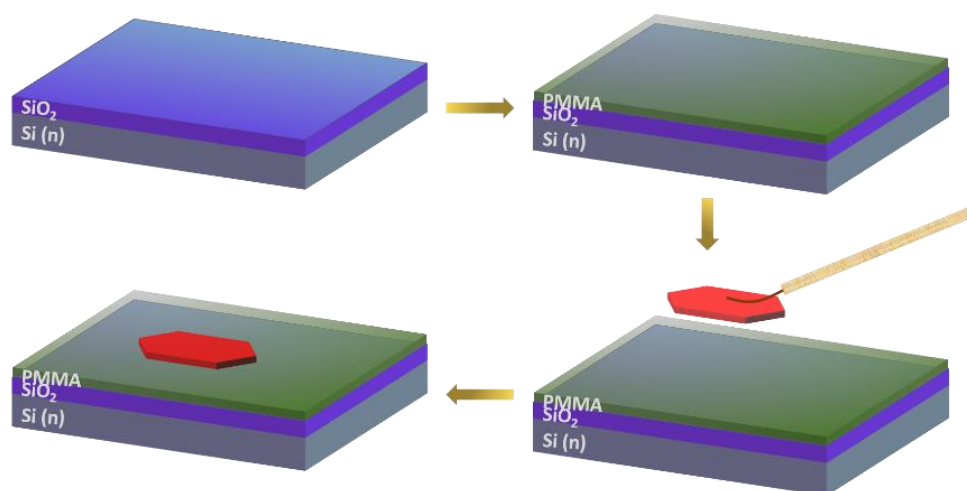


Figure 2.14. Schematic diagrams of preparation of PMMA/ SiO_2/Si substrate and crystal lamination.

Secondly, the source-drain electrodes were fabricated by evaporating metal balls through a shadow mask into the single crystals by means of vacuum thermal evaporation method.

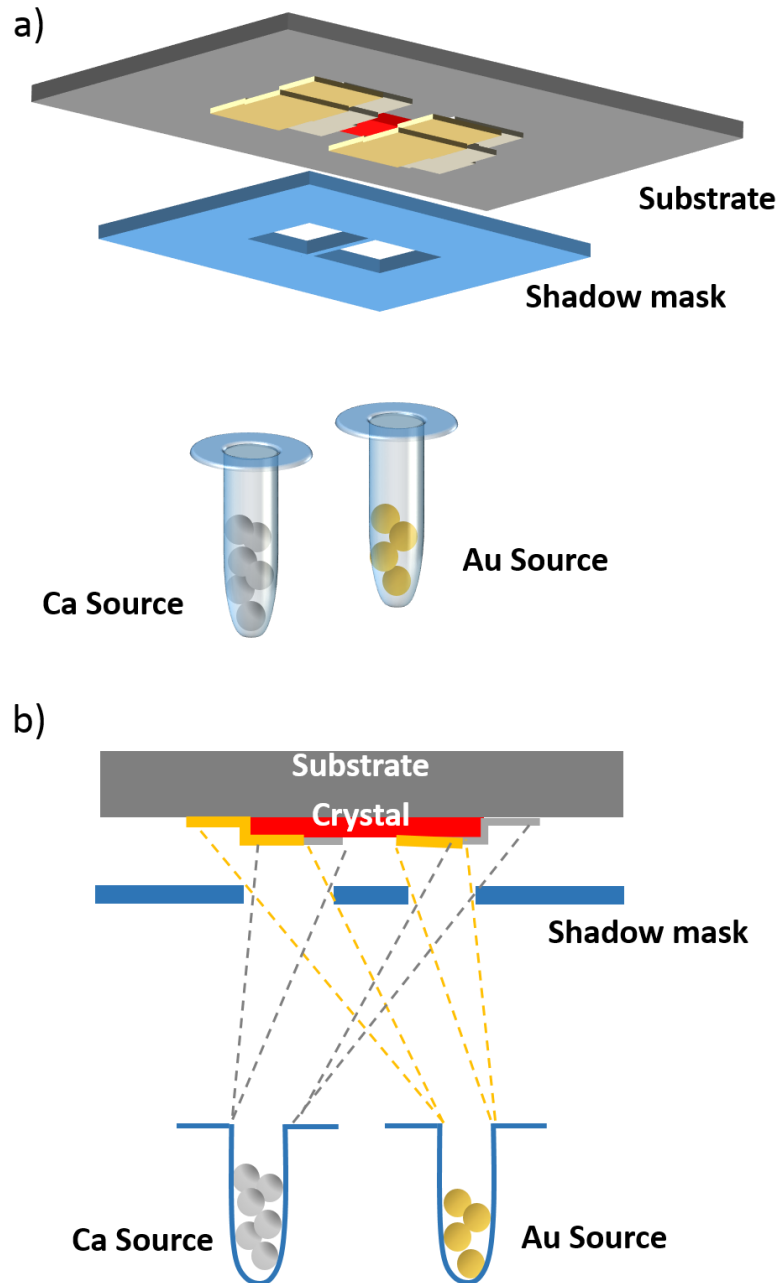


Figure 2.15. a) schematic diagram and its side view of asymmetric electrode fabrication process by depositing Ca and Au through a shadow mask.

The metal electrodes were selected based on the work-function matching with the HOMO/LUMO level of the organic semiconductor. Au ($\varphi = 5.1$ eV) electrode has been known to perform good hole carrier injection to many organic semiconductors. As for electron injector, low work function metal must be employed. Ca with a work function $\varphi = 2.87$ eV is in the vicinity of LUMO levels of many luminescent organic semiconductors. Therefore, all processes of our experiment are operated in Ar glove-box to avoid oxidation of Ca.

Two different metal electrodes should be deposited in different end of the transistor channel for realizing ambipolar transport. As illustrated in figure 2.15, asymmetric electrodes were fabricated by using an offset, leaving some part of Ca under layer in direct contact with the single crystal acting as electron injector. On the other side, an overlaid Au layer acts as a hole-injector. As for the deposition of the metals, Au layer was deposited to 100 nm at the rate of 0.4 Å/s; thickness of Ca layer was about 500 nm with depositing rate of 6 Å/s.

2.2.4 Measurements of Field-Effect Transistors

All the devices were measured in the atmosphere of Ar gas in the glove-box. The field-effect transistor measurement was performed using a probing system in dark condition. A semiconductor parameter analyzer (Agilent E5207) was used for device measurements.

Two terminals field-effect transistor characterization was performed for all devices. I_D - V_D output and I_D - V_G transfer characteristics were obtained. These characteristics contain hole- and electron-mobility as well as their accumulation threshold voltage (V_{th}) parameters. The value of charge carrier mobility were extracted from local regression of $I_D^{1/2}$ - V_G transfer characteristics by using following equation

$$\mu = \frac{2L}{W} \frac{1}{C_i} \left[\frac{d(I_{D,sat}^{1/2})}{dV_G} \right]^2$$

(Equation 1.3)

On the other hand, the accumulation threshold voltage can be estimated from the intersection between the interpolation of the regression function and zero current value.

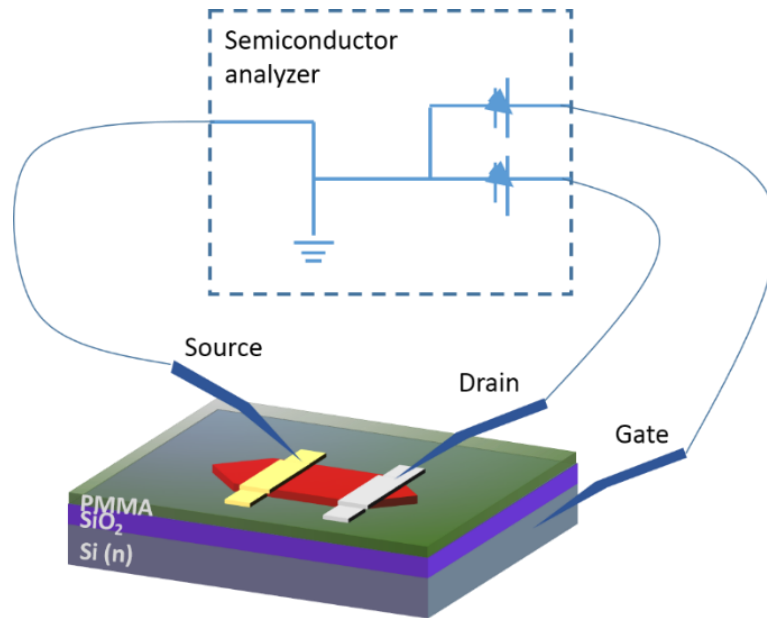


Figure 2.16. Schematic diagram of the ambipolar FET device and its measurement.

The light emission measurement was also performed inside the glove-box with atmosphere of Ar gas. An optical microscope connected to a CCD camera was used for imagery observation from the top view of the device. The standard light-emitting transistor measurement was performed so different that charge carrier injected into different electrodes, and accumulation layer of two different carriers were formed in the vicinity of each charge carrier injector. The carrier recombination happened at the crossover between electron and hole accumulation layer.

Chapter III

Gain Properties of Thiophene/Furan/Phenylene Co-oligomer Single Crystals

3.1 Introduction

Compared with inorganic lasers, organic lasers have been broadly admitted to have advantages of low money-cost, easy-to-make and wavelength-tunable.^[51, 89, 90] Optically pumped organic lasers have been realized and broadly reported for almost twenty years,^[4, 5, 50] from which thiophene/phenylene co-oligomer (TPCO) has been recognized as one of the most effective gain media.^[49, 66] While on the other hand, scientists from physics, chemistry and materials research have also spared no efforts on realizing electrically driven lasers as it would provide a new class of convenient and easy-to-manufacture lasers, but no one has realized it to date.^[55, 91]

A laser consists of nothing but a gain medium in a resonator, investigating the gain properties of materials in the device active layer is definitely a crucial factor. Moreover, during the gain processes, both how efficient the energy from incident light converts to gain emission and gain competition among different wavelength are well worthy to investigated. Among numerous reports on gain-narrowing behavior in organic single crystals, some of the materials showed dual gain-narrowed peaks, and the gain behavior of these peaks was investigated, but no one has given an exact mechanism of this dual peaks phenomena so far.^[92-97]

Recently, we have reported a series of newly synthesized thiophene/furan/phenylene co-oligomers (2-(4-biphenyl)-5-[5-(4-biphenyl)-2-thienyl] furan: BPFT and 2,5-bis(4-biphenyl)bifuran: BP2F),^[65] which are designed based on 2,5-bis(4-biphenyl)bithiophene (BP2T).^[63, 67] During our comparative laser pumping characterization of these three materials, we also observed dual gain-narrowed peaks in BPFT single crystal (see figure 3.3a).

Considering this phenomenon involves the issue of energy efficiency and distribution, both of which are extremely important to laser, we believe investigating the phenomenon will give us a positive hint for material design for lasers. The above three materials are suitable for comparative studies to accomplish the purpose because of their similar molecular structures. Comparing both the gain-narrowed and fluorescence spectra of these three thiophene/furan/phenylene co-oligomers in single-crystalline and in deposited thin-film forms, we assigned that the dual gain-narrowed peaks correspond to the vibronic transitions from $S_{1,0}$ to $S_{0,n}$. Combining the transient absorption spectra, regular absorption spectra and gain-narrowed spectra, we finally concluded that the number of gain-narrowed peaks is affected by the self-absorption of molecules in both the ground-state and the excited-state. Energy distribution among the vibronic bands is determined by many factors, such as transition probability from $S_{1,0}$ to $S_{0,n}$, self-absorption, density of pump laser and so on. Furthermore, by characterizing gain behavior depending on excitation energy and on energy density, the two gain-narrowed peaks in BPFT crystal have been attributed to amplified spontaneously emission (ASE) and super-fluorescence (SF), respectively. Finally, it is suggested that gain behavior with the highest energy efficiency can be expected when only the vibronic transition with the highest transition probability is confined in the window of absorption by ground-state and singlet-state molecules.

3.2 Experimental Section

Preparation of Samples - BP2T was purchased from Aldrich (99.5%), while BPFT and BP2F were synthesized by us. All these three materials were purified by sublimation method. Single crystals were grown by physical vapor transport in a stream of argon gas (99.9999%). These high quality crystals were firmly attached

on highly doped silicon wafer with 200 nm thermally oxidized SiO₂ layer because of electrostatic force.

Absorption and Fluorescence Spectra - Absorption spectra were obtained from UV/vis spectrophotometer (JASCO: V-650DS). Fluorescent spectra were obtained from fluorescent spectrophotometer (HITACHI: F-7000) with the excitation wavelength at 380 nm.

Laser Pump (1) - Figure 3.1 illustrated the schematic and laser route of laser pump excitation. A nitrogen nanosecond-pulsed laser at 337.1 nm (Stanford Research Systems, NL100) was employed as the pump source, the frequency of the laser pump was 1 Hz, and the duration time is 100 ms. The spot size of the pump laser on the samples was estimated to be about 0.5 mm in radius. The pulse energy is controlled by sending the beam through a neutral density filter. The signal of emitted light was detected by the optical fiber spectra meter (HAMAMATSU, PMA-12 photonic multi-channel analyzer). The crystals used during this characterization were picked by electrostatic-bonding manipulation and put on the plasma matched Si/SiO₂ substrate. For easy comparison, all the chosen single crystals are at the size of about 1 μm in thickness and 0.4 mm² in area.

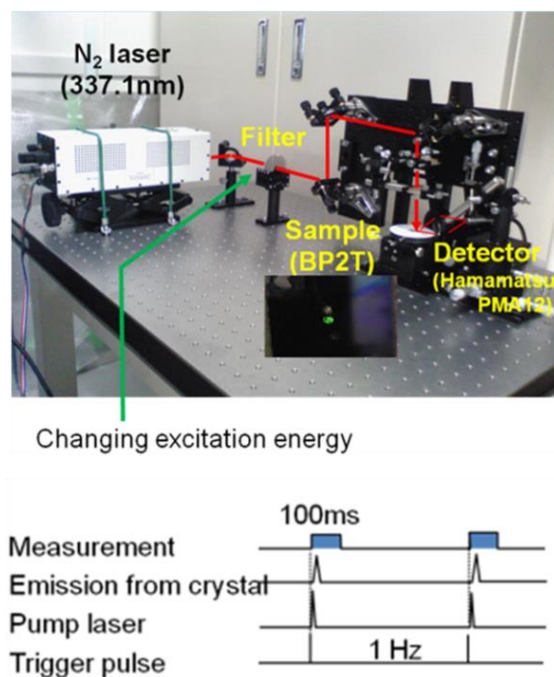


Figure 3.1. The schematic and laser route of laser pump excitation.

Laser Pump (2) - The same laser source and spectra meter was used as the aforementioned laser pumping characterization. Schematic diagram of laser pump (2) is shown in figure 3.2. By tuning position of cylindrical lens 1, shape of laser beam can be narrowed in vertical direction. Table 3.1 shows the sizes of laser beam when lens 1 changes positions.

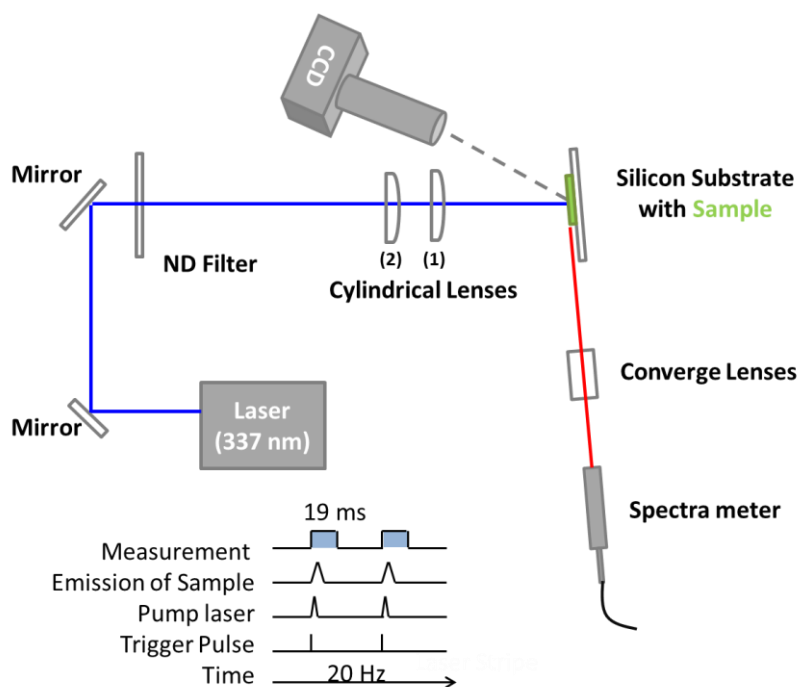


Figure 3.2. Schematic diagram of laser pump (2). Sample is not vertical to the laser beam. This is because the transition dipoles of molecules in crystals are vertical to the *ab* plane, and it is easier excited with some angle to the laser.

Table 3.1. Shape changes of laser beam with tuning position of lens 1

Position	30mm	31mm	32mm	33mm	34mm	35mm	36mm	37mm
Width (μm)	228.2	264.2	403.5	518.6	661.9	824.9	1046.3	1178.2
Area (cm^2)	0.003	0.00347	0.0053	0.00682	0.0087	0.01084	0.01375	0.01549
Photo								

*This value is only numbers shown on the setup track, which is smaller than the distance from lens 1 to the sample.

Transient Absorption - Figure 3.3 illustrates the schematic diagram of transient absorption characterization. Laser beam at the wavelength of 400nm was used for exciting the crystal sample to the excited state. The duration of the laser beam (energy density: $760 \mu\text{J}/\text{cm}^2$) pulse is 100 fs. And 0.5 ps later, white-light probe beam was applied as incident light, photodiode detector was used for spectra detection.

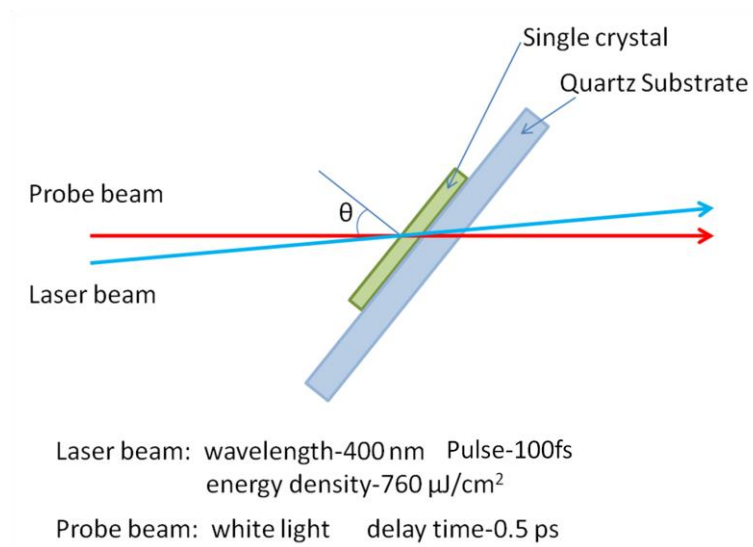


Figure 3.3. Schematic diagram of transient absorption characterization.

3.3 Results and Discussion

3.3.1 Gain-narrowing behaviors

In laser-induced photoluminescence measurements, all the single crystals used in present studies showed gain-narrowing behavior, which can clearly be evidenced by gain-narrowed peaks at 555 nm and 516 nm for BP2T and BP2F, respectively (see figure 3.4a), also it is interesting that BPFT shows two gain-narrowed peaks (512 nm and 544 nm).

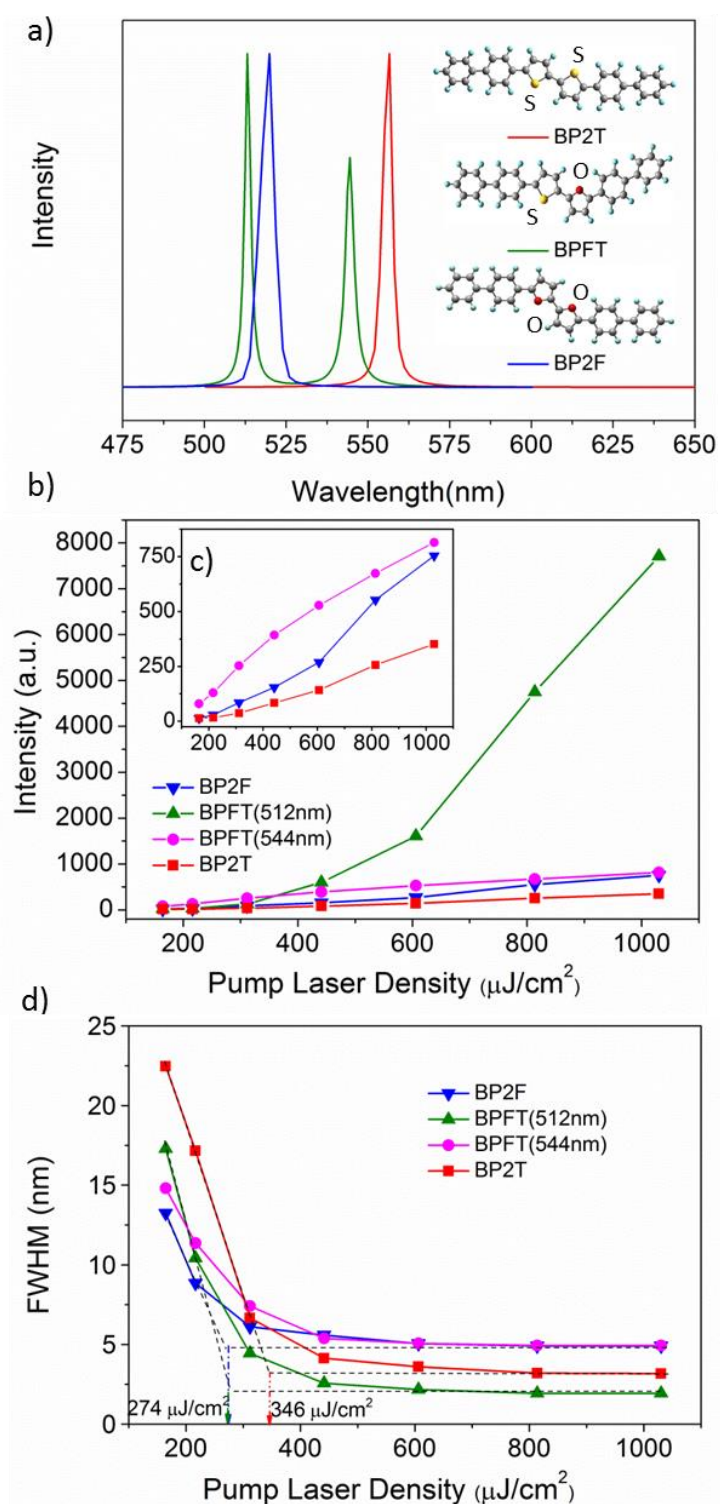


Figure 3.4. a) Gain-narrowed spectra in single crystals and molecular structures of BP2T, BPFT and BP2F; b), c) gain intensity and d) FWHM variation by increasing the pump laser energy of BP2T, BPFT at 512 nm, BPFT at 544nm and BP2F, respectively.

From figure 3.4b-d, BPFT (at 512nm) and BP2F single crystals showed smaller threshold (both are $274 \mu\text{J}/\text{cm}^2$) than that of BP2T ($346 \mu\text{J}/\text{cm}^2$). Being compared with other three gain peaks, a striking emphasis should be given to the fact that the gain peak intensity of BPFT at 512 nm increased sharply with increasing the pump laser energy. Because the crystals of the three materials are in similar size (area: 0.4 mm^2 , thickness: $1 \mu\text{m}$), this result corresponds to the much higher luminescent efficiency of BPFT single crystal.^[65, 98] In addition, the full width at half maximum (FWHM) of the gain peaks for BP2T, BPFT and BP2F single crystals are 4.0, 1.93 (at 512nm) and 4.91 nm, respectively (see Fig. 3.4d). All these phenomena demonstrate that the newly synthesized materials (especially BPFT single crystal) have better properties of both lower threshold and higher emission efficiency. BPFT single crystal is consequently more promising for application as gain media for laser.

3.3.2 Reason for dual gain-narrowed peaks

One possible reason of the fact that only BPFT showed dual gain-narrowed peaks is that the excited state configuration of BPFT molecule formed two parts of delocalized conjugation of electrons. However the hypothesis can be excluded by comparing their fluorescence spectra.

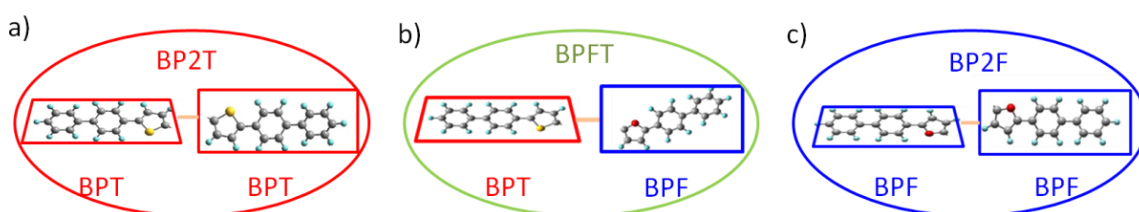


Figure 3.5. Schematic diagram of the twisted excited state configuration of a) BP2T, b) BPFT and c) BP2F molecules in crystals, the red part represents the plane of BPT, the blue part is the plane of BPF, and the orange line represents the carbon bond between these two parts which are not in the same plane.

As mentioned before that BPFT single crystal shows dual gain narrowing peaks, and the 512 nm one is near that of BP2F (516 nm), and the 544 nm one is near

that of BP2T (555 nm). The direct explanation is that because the single carbon bond between thiophene unit and furan unit can freely roll, the excited state configuration of BPFT molecule in crystal is possibly twisted and form two parts of delocalized conjugation of electrons (see Fig. 3.5b), one is the part of BPT (the same as those in BP2T), the other is BPF (the same as those in BP2F). This assumption suggest that these two parts of delocalized conjugation of electrons (BPT and BPF) will respectively have fluorescent emission, which can induce the behavior of dual gain narrowing peaks in BPFT single crystal.

The wavelength of fluorescent transition is determined by particular electronic structure of conjugated fragment, which means if our hypothesis was true, the fluorescent spectrum of BPFT must be simply multiplied by those of BP2T and BP2F. However, such expected phenomenon could not be observed in fluorescent spectra (see figure 3.6) of these three materials in thin films (thickness is 30 nm), which means this hypothesis about two parts of delocalized conjugation of electrons is wrong.

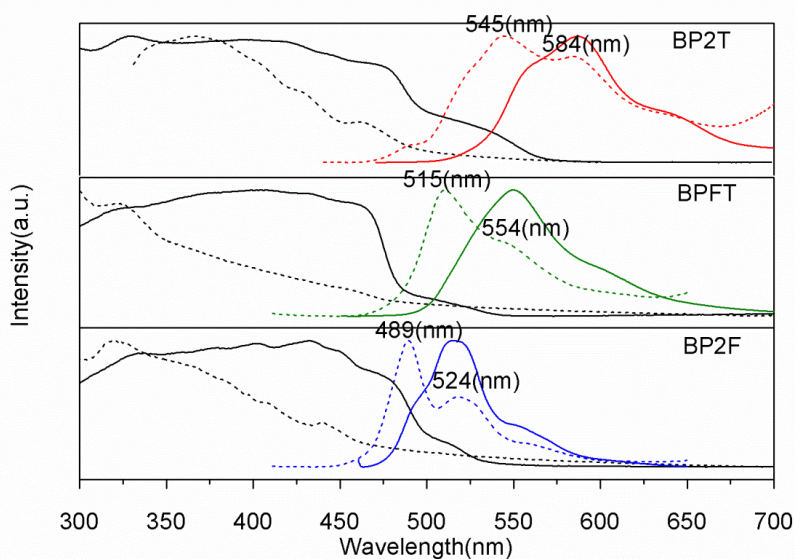


Figure 3.6. Absorption and fluorescent spectra of BP2T, BPFT and BP2F in both single crystals and thin films. Black solid lines are absorption spectra in crystals; black dashed lines are absorption spectra in thin film (30 nm); colored solid lines are fluorescent spectra in crystals; colored dashed lines are fluorescent spectra in thin film (30 nm), respectively.

Another reason to be considered is weaker self-absorption in BPFT single crystal than those in the other crystals, which is treated as the most probable reason for BPFT illustrating dual gain-narrowed peaks. Ground-state and transient absorption and ASE spectra of BP2T, BPFT and BP2F single crystals and their fluorescence spectra both single-crystalline and in thin-film forms are shown in figure 3.7. A large difference in the fluorescence spectra between single crystals and thin films indicate the self-absorption plays a prominent role in their luminescence properties. Because the transition dipole moments are along the long axes of these molecules which are almost perpendicular to the *ab* plane in single crystal phase of thiophene/furan/phenylene co-oligomers, the direction of light propagation is almost along the crystal faces.^[65, 99] Furthermore, the refractive index of organic single crystal is so high that the fluorescence has to be confined in the parallel crystal faces and propagate by a waveguide effect.^[35, 100] The two reasons described here are important to cause the effective self-absorption during light propagation. Figure 3.6 illustrates that the absent of luminescent peaks at 559, 515 and 487 nm for BP2T, BPFT and BP2F single crystals, respectively, corresponds to larger absorption at these wavelength in single crystals being compared with those in thin films. Figure 3.7 shows the absorption of BPFT at 515 nm, corresponding to the wavelength of gain-narrowed emission, is the weakest among the three bands. Therefore, we get the hypothesis that appearance of the gain-narrowed peak is determined by the intensity of absorption at the same wavelength.

Figure 3.4b shows photoluminescence intensities plotted against the pump power density. Behavior of BPFT single crystal illustrates that the peak intensity at 512 nm is weaker than that at 544 nm at low pump densities (smaller than the ASE threshold), while it dramatically increases when the excitation density is beyond the gain threshold. The observed phenomenon indicates that the peak at 512 nm amplitude is hardly amplified by low pump density due to the self-absorption, but the gain emission can grow up when the stimulated emission surpasses the weak self-absorption, which is partially bleached by the pump laser, in the case of relatively high pump density. This understanding also corresponds well to our hypothesis that the number of gain peaks is influenced by self-absorption.

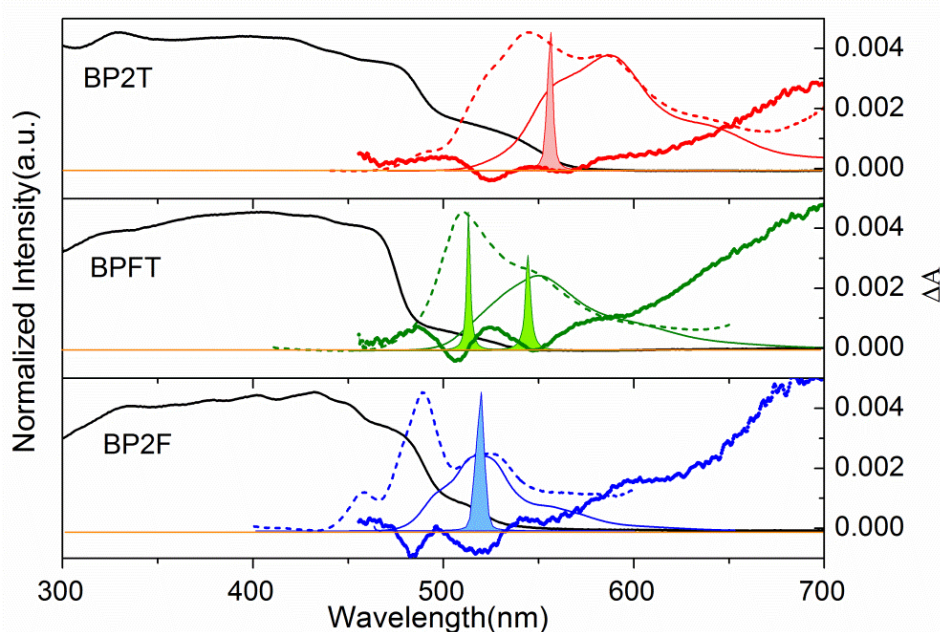


Figure 3.7. Combination of transient, absorption and fluorescence spectra of BP2T, BPFT and BP2F in both single-crystalline and thin-film forms. The black solid lines correspond to absorption of single crystals, color-dashed lines are fluorescence spectra of thin films, color-solid lines are fluorescence spectra of single crystals, gain-narrowed spectra are presented by color filled lines, and the colored lines with symbols correspond to transient absorption spectra.

In order to make further proof of this hypothesis, we have made transient absorption characterization for these three materials. The transient absorption spectra in figure 3.7 show that these three single crystals have two dips corresponding to amplification of the probe white light by stimulated emission. Accordingly, we can reach a reasonable conclusion that all three materials should have two gain-narrowed peaks corresponding to their two dips easily detected in the transient absorption spectra. However, only BPFT showed the expected result, while BP2T and BP2F showed only one gain-narrowed peak as we reported above. By comparing their intensities of the absorption at the shorter wavelength dips, we got the results that the intensities at the shorter wavelength dips of BP2T and BP2F is much stronger than that of BPFT, so the gain-narrowed peaks at shorter wavelength dips of BP2T and BP2F cannot grow because of strong self-absorption.

3.3.3 Energy distribution and efficiency

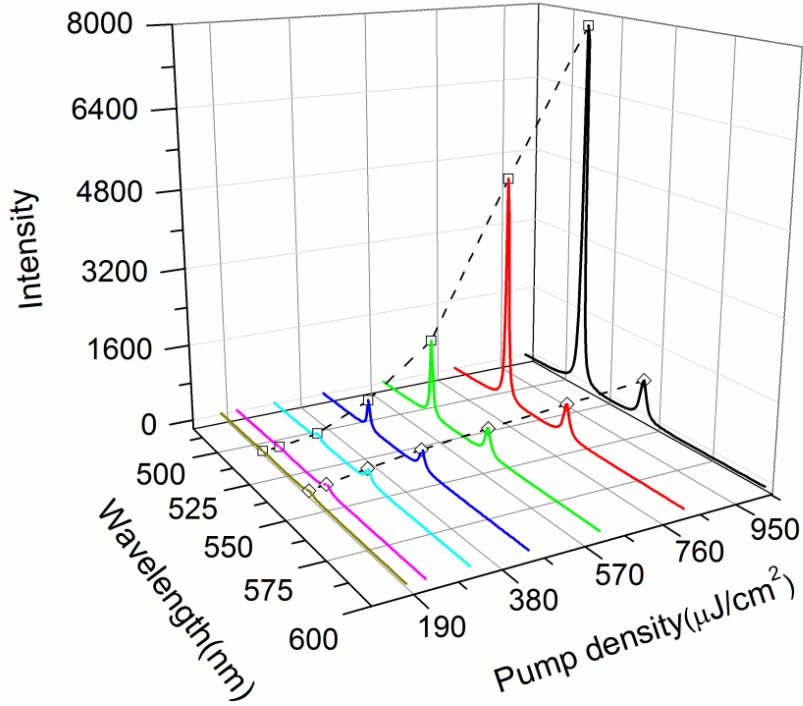


Figure 3.8 Pump energy dependence of the two gain-narrowed peaks of BPFT single crystal recorded at 512 nm and 544 nm.

Figure 3.8 shows a pump energy dependence of the two gain-narrowed peaks of BPFT single crystal recorded at 512 nm and 544 nm. The intensity of the gain-narrowed peak (I_{SE}) at 512 nm can be well explained in terms of population rate equation 3.1 constructed by an exponential function associated with the gain phenomenon. On the other hand, the gain-narrowed peak at 544 nm shows saturated behavior.

$$I_{SE} = I_{SE,0} \exp(\sigma_{1-0} N y I_p / I_{p,sat})$$

(Equation 3.1)

in which $I_{SE,0}$ is I_{SE} at $y = 0$, N the density of molecules, σ_{1-0} the SE cross-section, y the gain length, I_p the pump intensity, and $I_{p,sat}$ the pump intensity at saturation. The aforementioned phenomena easily drive us to the potential reason of singlet-singlet annihilation, the process of which will be illustrated as follows:

$$S_1 + S_1 \rightarrow S_n^* + S_0$$

(Equation 3.2)

To prove the hypothesis that singlet-singlet annihilation happened during laser pump in BPFT single crystal, we have compared the molecular density (10^{17} molecules/cm²) and photo density (5.29×10^{14} photos/cm²).

As for calculation of exciton diffusion in BPFT single crystal, we treat our crystal as layer-by-layer model along *ab* plane. According to the lattice constant of BPFT single crystal, (see reference 35), we got the molecular density in one layer:

$$M.D. = N / (nab) = 4.523 \times 10^{14} \text{ cm}^{-2}$$

Where N is the molecular number and n is the number of molecular layer in one cell. When the incident laser irradiates *ab* layer of BPFT single crystal, all the molecular in the laser spot will be excited. The thickness of our crystal is about 1 μm , $c=49.762 \text{ \AA}$, so one single crystal contains 200~300 layers of molecules, and the molecular density in our BPFT single crystal is:

$$M.D._{(all)} \approx 10^{17} \text{ cm}^{-2}$$

For exciton density, the energy of one photon is:

$$\varepsilon = hc / \lambda = 5.897 \times 10^{-13} \mu\text{J}$$

So at the pump density of $312 \mu\text{J}/\text{cm}^2$, the photon density is about 5.29×10^{14} photons/ cm².

Considering that the exciton diffusion radius is about to 5 nm and corresponds to about one hundred molecules in the diffusion sphere. Then, singlet-singlet annihilation implies that we only need to excite approximately 1% of the molecules to reach saturation, in good agreement with the ratio between the numbers of photons and molecules (see figure 3.9). However, singlet-singlet annihilation cannot explain different behavior of these two peaks that the saturated behavior shows at peak 544nm, while peak at 512 nm has exponential behavior.

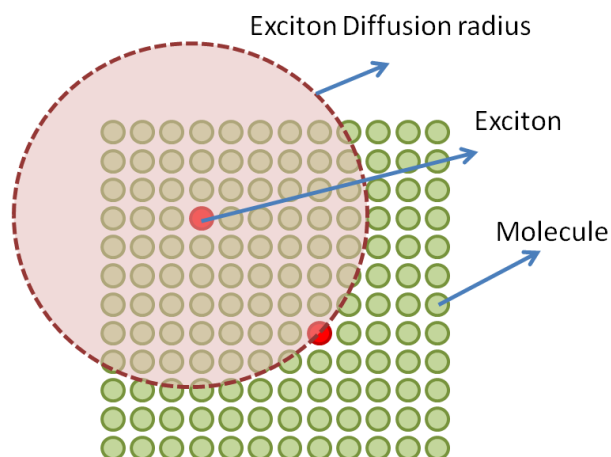


Figure 3.9. Schematic diagram of exciton diffusion in BPFT single crystal at 312 $\mu\text{J}/\text{cm}^2$ pump laser density.

Since photo-luminescent property (especially for gain emissions) strongly relates with vibronic transitions, here we assigned the positions of vibronic emissions of these three materials. The optical transitions between the coupled vibrational-electronic levels of a molecule can be understood by invoking the Frank-Condon principle, whose configuration diagram is shown in figure 3.9. This energy diagram illustrates the vibronic transitions in a molecule with Morse-like potential energy functions in both the ground and excited electronic states.

According to reference 101, BP2T has vibronic emissions $S_{1,0}$ - $S_{0,0}$ at 485 nm, $S_{1,0}$ - $S_{0,1}$ at 524 nm and $S_{1,0}$ - $S_{0,2}$ at 564 nm. Correspondingly, vibronic emissions for BPFT are $S_{1,0}$ - $S_{0,0}$ at 481 nm, $S_{1,0}$ - $S_{0,1}$ at 515 nm and $S_{1,0}$ - $S_{0,2}$ at 544 nm; vibronic emissions for BP2F are $S_{1,0}$ - $S_{0,0}$ at 459 nm, $S_{1,0}$ - $S_{0,1}$ at 487 nm and $S_{1,0}$ - $S_{0,2}$ at 516 nm. It means that the peaks at 512 nm and 544 nm in BPFT can be ascribed to vibronic transitions from $S_{1,0}$ to $S_{0,1}$ and $S_{0,2}$ state, respectively.

Energy distribution between these two vibronic peaks is mainly determined by the transition probabilities from an excited state to the ground state, which is proportional to the square of the overlap of the vibrational wave-functions.^[102] The fluorescence spectra of BPFT thin film shows that the transition probability from $S_{1,0}$ to $S_{0,1}$ (512 nm) is markedly larger than that from $S_{1,0}$ to $S_{0,2}$ (544 nm). However, probabilities of these two vibronic transitions cannot be constant owing

to self-absorption. The process can be described that the photoluminescence peak at 512 nm is suppressed by self-absorption when the pump energy density is low, and become predominant transition because of the largest transition probability when the self-absorption is partially bleached with the high pump energy density.

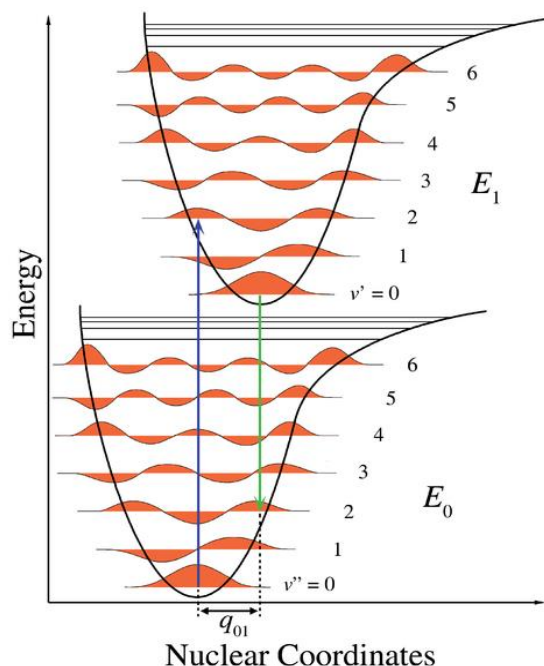


Figure 3.10. Configuration diagram for two electronic states in a molecule.

Vibrational-electronic (vibronic) transitions are indicated by colored vertical arrows.

From the viewpoint of energy distribution, optical gain simultaneously occurring in dual peaks seems to be a disadvantage for realizing laser because gain-narrowed peak at 544 nm will divide some energy from that at 512 nm. However, when compared with the gain observed for BP2T and BP2F, each of which only shows a single gain-narrowed peaks, BPFT performed distinctly with much higher emission intensity. It can be considered to be a reason that the vibronic band with the largest transition is available for ASE in a BPFT single crystal because of the smallest overlap with the ground-state absorption, which can be bleached with the high pump energy density, and the energy loss to the peak at 544 nm is saturated owing to the competition with the peak at 512 nm. As for BP2T^[19] and BP2F (supporting information), strong self-absorption prevents

ASE of vibronic transition $S_{1,0}$ - $S_{0,1}$, and low transition probability from $S_{1,0}$ - $S_{0,2}$ causes quite low gain intensity.

3.3.4 Dependence on excitation density and area

Gain behavior can be attributed to either well-known ASE or SF.^[103-107] Florov *et al.* observed ASE and SF process from 2,5-dioctyloxy poly(*p*-phenylene-vinylene) (DOO-PPV) thin film at room temperature.^[106] Hiramatsu *et al.* elucidated ASE and SF contributions to the gain emission of 5,5"-bis(4-biphenyl)-2,2':5'2"-terthophene (BP3T) single crystal.^[107] Both of the two reports argued that the most intuitive difference between these two processes is that threshold of ASE depends upon excitation density while SF follows excitation energy dependence.^[106, 107]

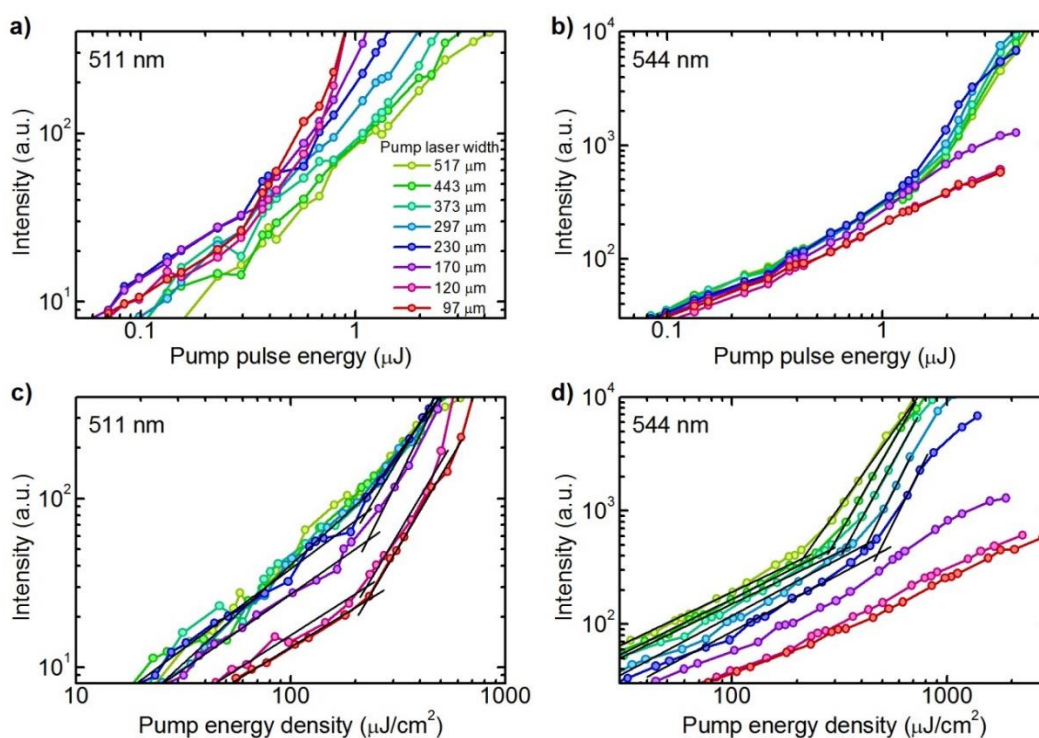


Figure 3.11. Gain-narrowing behavior of BPFT single crystal varies with excitation energy and pump laser width. (a), (b) are intensities of peaks at 511 nm and 544 nm plotted against excitation energy; (c), (d) are those plotted against excitation density.

For further understanding of this dual gain-narrowing behavior in BPFT single crystal, the dependence of gain narrowing on excitation energy and on energy density was characterized (Refer to figure 3.2 for experimental setup). In this characterization, the width of the strip laser beam was varied from 97 to 517 μm by defocusing a condensing cylindrical lens keeping the total energy constant. Figure 3.12 illustrates the intensity of the dual gain-narrowed peaks against excitation energy (figure a and b) and energy density (figure c and d) of laser pump, and threshold was observed for the peak at 511 nm when laser was irradiated to a relatively small area, while when a wide laser beam was used, no threshold was observed. The intensities of the peak at 511 nm were plot against excitation density in figure 3.11c, and curves with relatively smaller excitation widths showed similar behaviors. The threshold at around $226 \mu\text{J}/\text{cm}^2$, did not change with excitation beam width as shown in figure 3.12. This phenomenon indicated that the peak at 511 nm behaved as an ASE process. In ASE process which is a direct result of stimulated emission, as observed for the peak at 511 nm of BPFT, the spontaneous emission from individual molecules is amplified as it propagates through the population-inverted molecules. And population inversion is governed by density of excited molecule, which means excitation density is a key factor of ASE process.

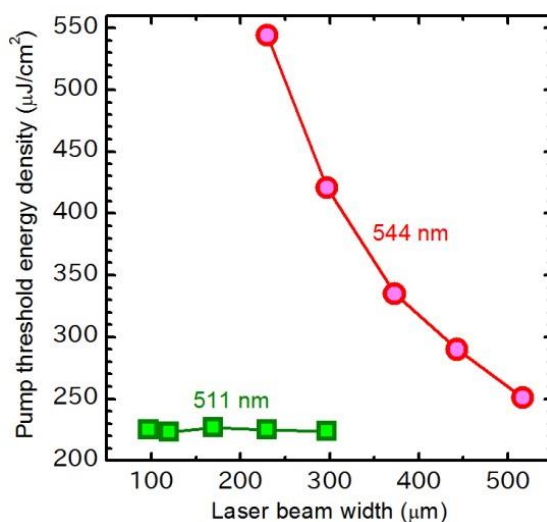


Figure 3.11. Changes in threshold of pump energy density for peaks at 511 nm (green squares) and 544 nm (red circles) as a function of excitation laser beam width.

On the other hand, peak at 544 nm shows an opposite behavior that showed a threshold only when the excitation width was wide enough, and these curves had almost the same behavior in figure 4b, which was plotted as a function of excitation energy. In the case of behavior against excitation density, threshold of the peak at 544 nm decreased with increasing the excitation width (red curve in figure 3.13). This phenomenon indicated that a SF process involved with peak at 544 nm. In the cooperative process, such as SF, the excited molecules participate in building up of macroscopic dipole moment in a crystal, and such process is governed by the total number of excited molecules. In other words, a SF process requires enough excitation energy so that the number of excited molecules can reach to the threshold.

Accordingly, ASE requires superior optical confinement in the gain media while SF can occur even with serious radiation leakage.^[104, 106, 107] BPFT single crystal is in the similar situation with BP3T that the $S_{1,0}$ - $S_{0,1}$ emission at shorter wavelength (511 nm) is more confined in the crystal cavity, while in the $S_{1,0}$ - $S_{0,2}$ emission (544 nm), a considerable amount of radiation maybe leaked from the crystal.

As described earlier, the peak at 511 nm showed threshold when the width of laser beam is small; while threshold was also observed for peak at 544 nm when laser beam became wider. This indicates that energy competition occurs between these two vibronic transitions processes. Before coherent dipole moment builds up in a microscopic scale in SF process, spontaneous emission can be amplified when laser beam is small, i.e., excitation density is high. On the other hand, when laser beam became wider, the excitation area is large and excitation density could not satisfied ASE requirement, prior to the condition that the excited molecules reached the threshold number for SF.

BP2T single crystal also showed dual gain-narrowing peaks, and their behaviors are shown in figure 3.13. As shown in figure 3.13, intensity of gain-narrowing peak against excitation density, almost all the curves overlapped with each other, and their thresholds are about $250 \mu\text{J}/\text{cm}^2$. As for peak 589, the value of threshold cannot be perorated because saturation behavior was observed. However, similar behaviors in figure 3.13b indicated that excitation density is the mean influencing factor. The aforementioned behaviors indicated that both peaks

of 563 nm and 589 nm were affected by excitation density instead of excitation area, in other words, both of these two peaks followed behavior of ASE.

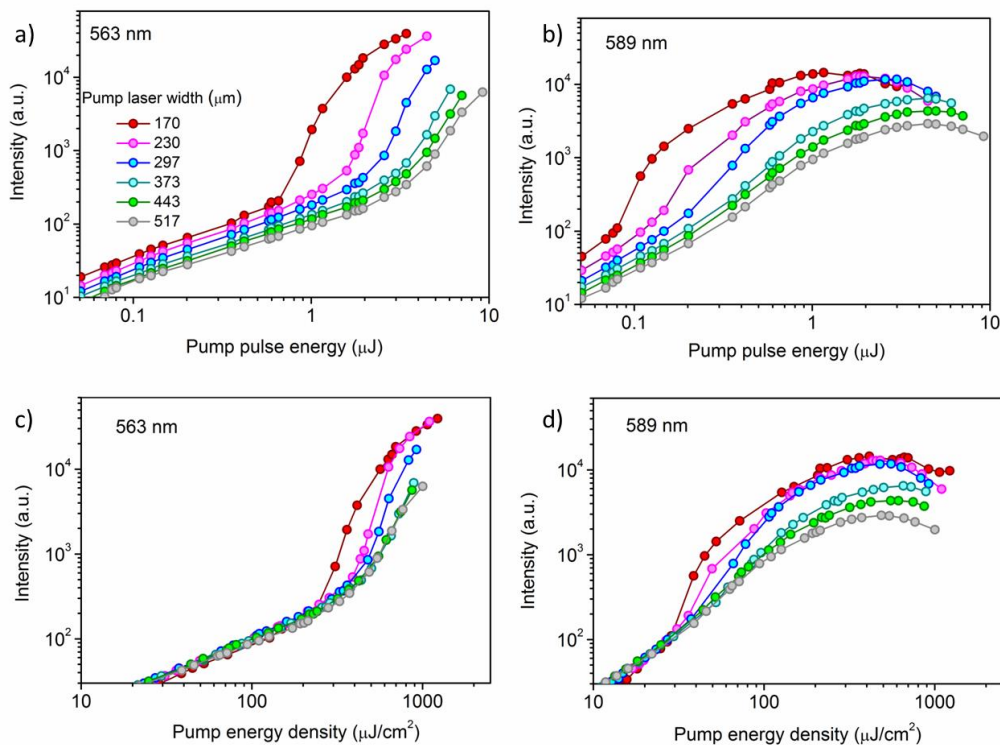


Figure 3.13. Gain-narrowing behavior of BP2T single crystal varies with excitation energy and pump laser width. (a) and (b) are intensities of peaks at 563 nm and 589 nm plotted against excitation energy; (c) and (d) are those plotted against excitation density.

3.3.5 Ideal material for laser

All the aforementioned phenomena give us important information to be considered on the preferable conditions of organic semiconducting materials for lasers. Figure 3.14 illustrates spectra of an idealized organic semiconducting material, from which we can see that absorption in the ground state and singlet state act as a casement, only vibronic transitions in the gap between these two absorptions can be a gain-narrowed peaks, in other words, the number of gain-narrowed peaks is confined by the gap. Moreover, when only a vibronic transition with the highest transition probability (transition S_{10} to S_{01} in the

schematic spectra) shows in the window, energy will be concentrated and gain behavior with the most efficiency can be expected.

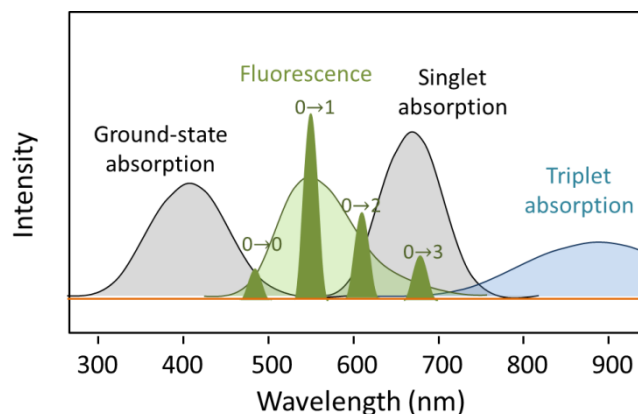


Figure 3.14. Schematic spectra of idealized material with the most energy efficiency.

The separated narrowed peaks correspond to vibronic transitions.

3.4 Conclusions

By comparing both the absorption and fluorescence spectra of these three thiophene/furan/phenylene co-oligomer in both single-crystalline and deposited thin-film forms, we assigned the dual gain-narrowed peaks corresponding to the vibronic transitions from $S_{1,0}$ to $S_{0,n}$ state. Combining the transient absorption spectra with ground-state absorption spectra, we finally determined that the number of gain-narrowed peaks corresponding vibronic transitions is affected by the re-absorption from both the ground-state and excited-state molecules, and energy distribution of this gain behavior is determined by transition probability from $S_{1,0}$ to $S_{0,n}$ and bleaching of the ground-state absorption. ASE and SF processes have been attributed to vibronic transition $S_{1,0}$ - $S_{0,1}$ and $S_{1,0}$ - $S_{0,2}$ in BPFT single crystal, respectively. Furthermore, gain with the highest efficiency can be expected when only the vibronic transition with the highest transition probability is confined in the window of absorption at both ground state and singlet state.

Chapter IV

Doped Crystals with Improved Optical Properties

4.1 Introduction

Doping is widely used in electroluminescent (EL) devices to modulate the emission of fluorescent materials.^[48] Due to the lattice mismatch and the weak intermolecular interactions in organic crystals, most reports of doping were amorphous materials^[108-110] till Wang et al. reported acene-doped OPV crystals with large size, good crystal quality and improved photo-luminescent properties.^[111] The principle of improving optical properties is based on resonance energy transfer (RET), which is a nonradiative process resulting from long range transition dipole-dipole interactions between the donor and acceptor.^[112] Tetracene-doped anthracene crystal is a good model for understanding exciton behavior in the doping system, because it has advantages of easy-manufactured, commercial available, simple molecular and crystal structure. In this chapter, optical property of tetracene-doped anthracene crystal was firstly studied, by which exciton behavior will be understand furtherly. One-dimensional nano-/microcrystals were prepared and investigated afterwards.

One-dimensional (1D) organic materials have been attracting considerable attention during the past decade,^[113-115] because these highly ordered functional materials in their characteristics structures possess intriguing optical and electronic properties.^[116-119] Their two-dimensional quantum confinement effect makes them promising building blocks for high performance electronics including chemical sensors,^[120, 121] organic light-emitting diodes (OLEDs),^[122] organic field effect transistors (OFETs),^[123] optical waveguide fibers,^[124] lasers,^[125-127] and so on. However, organic π -conjugated systems usually exhibit low efficiencies of light

emission on formation into solid-state 1D micro/nanostructures because of strong intermolecular π - π stacking interactions resulting in the concentration quenching of luminescence, which restricts the use of these materials in solid-state optical devices.^[128,129] To date, examples of one-dimensional organic nano/microcrystals with strong light emission are still limited,^[130-132] but the photo-luminescent efficiencies in these reported works were even less than 50%, not mention to compare with those in solutions. In the year of 2005, Xie and his co-works reported a *trans*-DPDSB (2,5-diphenyl-1,4-distyrylbenzene with two *trans* double bones) crystal with strong fluorescence emission.^[43] It was the first example of cross dipole stacking of conjugated molecules in solid states, and this molecular pecking mode led to needle-like crystal morphology. On the other hand, research of one-dimensional doped crystals is still a relatively blank space to be filled. Zhao *et al.* reported rubrene-doped TPP nanorods with tunable light emission color.^[133] Wu *et al.* prepared tetracene-doped enthracene nanowires and investigated homogeneity against doping concentration.^[134] However, neither of them paid attention to the change of luminescent efficiency.

In this contribution, we investigated morphology of *trans*-DPDSB crystals by using transmission electron microscope (TEM), and size-controllable crystal can be obtained by controlling the time of crystal growth. Furthermore, amplified spontaneous emission (ASE) threshold are much decreased from reported 680 $\mu\text{J}/\text{pulse}$ (corresponding to 13600 $\mu\text{J}/\text{cm}^2$) to 238 $\mu\text{J}/\text{cm}^2$. As for doping, host matrix *trans*-DPDSB with attractive crystal structure that the molecules are packed in one-dimension along the b axis makes our doped crystals intrinsically form into nano/microwires. From the CIE (Commission Internationale de l'Eclairage) chromaticity diagram, blending an orange dye into blue matrix is treated as a brilliant method not only for tuning the light emission but with which white luminescence can also be achieved. Therefore, a material with orange light emission, cyano substituted oligo(*p*-phenylenevinylene)1,4-bis(R-cyano-4-diphenyl-aminostyryl)-2,5-diphenylbenzene (CNDPASDB),^[41] was chosen as luminescence center. We have successfully overcome the differences of molecular structures and their stacking modes, finally doped a certain quantity of CNDPASDB into *trans*-DPDSB by solution growth method, and maintained the original crystal structure of host crystal as proved by polarizing optical microscope analysis. These doped 1D crystals have ultra-long size, high luminescent

efficiency (~80%) and color tunable light emission. Charge carrier mobility also has been characterized for the feasibility of these doping crystals for realizing electroluminescent (EL) devices.

4.2 Experimental section

Tetracene-doped Anthracene crystal

Sample Preparation - Materials were purchased from Aldrich (99+%), the solvents were technical grade. To begin, some CH₃OH solvent was added to the beaker, containing the mixture of AN and TE. The CH₂Cl₂ solvent was then added gradually until the material dissolved completely. The mixture was injected into a 25 ml flask, with some cotton plug filling the mouth. Finally, 100ml methanol was poured in a 500 ml wide-mouth bottle, and then the flask was put in this bottle, and covered the cap.

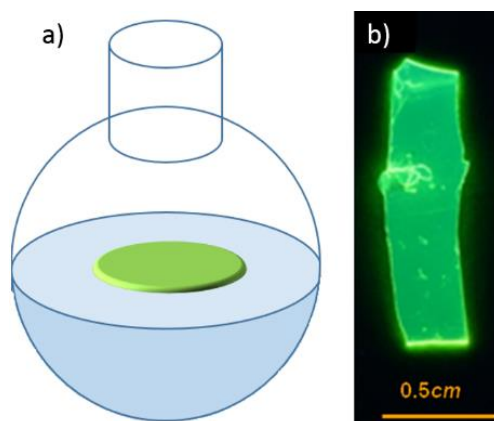


Figure 4.1. a) Schematic representation of growing crystals from the gas-liquid interface. Photographs under 365 nm UV light of (b) a TE-doped AN single crystal.

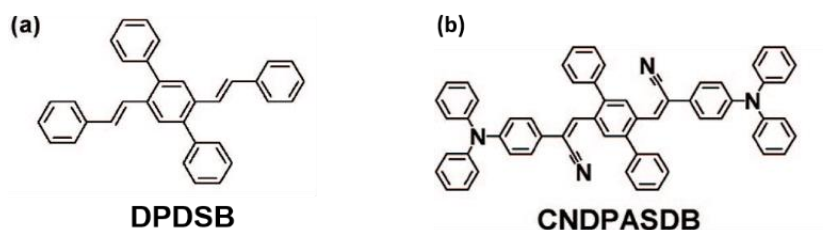
Crystal Quality - Wide-angle X-ray diffraction was measured using a Rigaku X-ray diffractometer (D/Max-rA, with Cu K α radiation of wavelength 1.542 Å).

Optical Properties - Photoluminescent spectra were collected at room temperature by an RF-530PC spectrophotometer. Crystalline state PL efficiencies were measured in an integrating sphere.

Time-Resolved Fluorescence - The measurements of both anthracene and doped anthracene crystals were performed using the time-correlated single photo counting (TCSPC) system under right-angle sample geometry. A 379 nm picosecond diode laser (Edinburgh Instruments EPL375, repetition rate of 20 MHz) was used to excite the sample. The emission was detected by a photomultiplier tube (Hamamatsu H5783p) and a TCSPC board (Becker&Hickel SPC-130). The instrument response function (IRF) is about 220 ps. All of the measurements were carried out at room temperature.

CNDPASDB-Doped *trans*-DPDSB crystal

Sample Preparation - *trans*-DPDSB and CNDPASDB were synthesized according to the previous published articles. Both pure and doped crystals were grown by vaporizing a mixture of dichloromethane and methanol slowly. Doping ratios were controlled by mixing solutions of DPDSB (2×10^{-3} mol/L) and CNDPASDB (5×10^{-4} mol/L) in particular proportion.



Scheme 4.1. Molecular structure of (a) *trans*-DPDSB and (b) CNDPASDB

Crystal Quality - The crystal size was controlled by growth time (22h, 29h and 42h). Crystalline phase were characterized by polarizing optical microscope.

Optical Properties - Absorption spectra were obtained from UV/vis spectrophotometer (JASCO: V-650DS), and fluorescent spectra were obtained by using fluorescent spectrophotometer (HITACHI: F-7000) with the excitation wavelength at 380 nm. PLQY were measured by a photo-counting method using an integration sphere on a Hamamatsu Photons C9920-02 spectrometer.

FET Device Fabrication - A highly n-type doped silicon wafer with a 300 nm thick SiO₂ film was used as a gate dielectric. For minimizing the electron traps at the

interface between the gate and organic semiconductor, a 30 nm thick Polystyrene film was spin-coated on the SiO₂ surface from the toluene solution as the buffer layer. The whole gate substrate was heated overnight at 90°C in the argon atmosphere. Doped crystals were drop-casted on the substrate by using methanol. Au (100 nm in thickness) and Ca (1 μm in thickness) for hole and electron injecting electrodes were deposited on the single crystal by vacuum evaporation with the shadow mask technique.

Theoretical Calculations - All quantum chemistry calculations were performed on the Gaussian 03 package. The molecular orbital energies were calculated by B3LYP/cc-pVDZ, which is a hybrid method of DFT and Hartree-Fock method.

4.3 Results and discussion

4.3.1 Tetracene-doped Anthracene crystal

XRD characterization

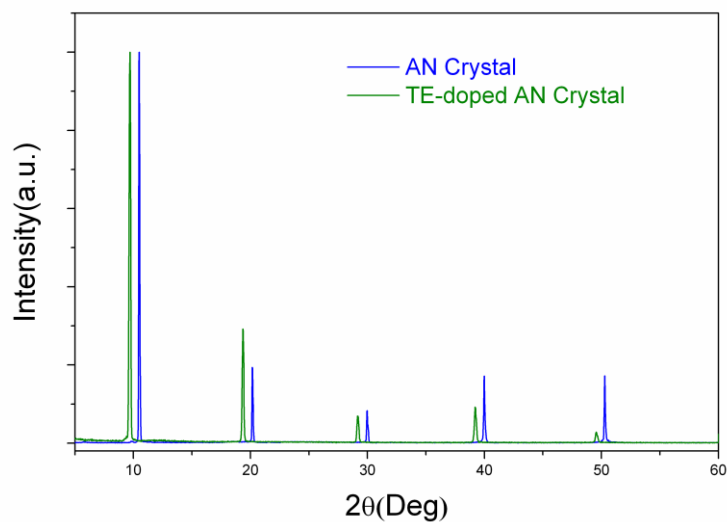


Figure 4.2. X-ray diffraction pattern of AN crystal and TE-doped AN crystal obtained by gas-liquid interface crystal growth method.

From the XRD patterns shown in Fig. 4.2, we can note that the crystals have a well ordered layer-by-layer structure, and we can easily calculate the distance

between two adjoining layers of the AN crystal and TE-doped AN crystal. These are found to be 0.901 nm and 0.903 nm respectively. Clearly, the layer spacing of the TE-doped AN crystal is a little bit larger than that of AN crystal. This may be due to the disturbance of the intrinsic AN crystal lattice caused by the embedding of doped TE molecules. This disturbance may also inhibit the formation of multi-layer crystallites leading to an area extend, that is why TE-doped crystals always show thinner but wider size than AN crystals.

Steady-State Fluorescence

Figure 4.3 shows the steady-state fluorescent spectra of AN single crystal and TE-doped AN single crystal, with peak positions of 444 nm and 532 nm, respectively. We noted that the peaks at 422 nm of AN single crystal and 509 nm of TE-doped AN single crystal are quenched, which may be caused by re-absorption. The reason of fluorescence re-absorption is that the refractive index of organic materials is so high that the fluorescence can propagate by a waveguide effect (discussed in chapter 3). As for the spectra of the TE-doped AN crystal, there is almost no emission at the position of the host, which indicates that the energy transfer from host to guest is extremely efficient.

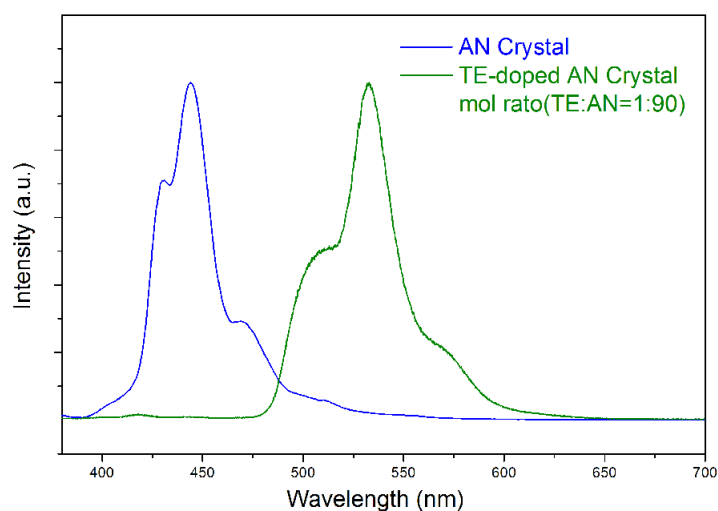


Figure 4.3. Fluorescence spectra of AN single crystal and TE-doped AN crystal obtained by the gas-liquid interface crystal growth method

The fluorescence quantum yield (Φ_f) of the crystals were also measured. As well known, Φ_f is reduced by chemical impurities, structural defects, and re-absorption of fluorescence. Usually the herringbone arrangement of AN and TE molecules in the solid state can sharply quench the luminescence, which is intrinsic to such kind of molecular aggregation. The Φ_f of crystals (AN and TE-doped AN) prepared were $34\pm 4\%$ and $89\pm 4\%$, respectively. This result indicated that the energy transfer from the AN molecules to the dopant TE molecules followed a very efficient process.

Time-Resolved Fluorescence

Time-resolved fluorescence is an effective method to explore the energy transfer in the doped system. Figure 4.4 shows the PL decay curves of the pure AN crystal and doped AN crystal, monitored at 432 nm that is one of the emission peaks of AN crystal. The decay time of the pure AN crystal is about 10.30 ns, while it is decrease to 0.11 ns for the doped crystal. The decreased decay time in the doped crystals clearly verifies the energy transfer process.

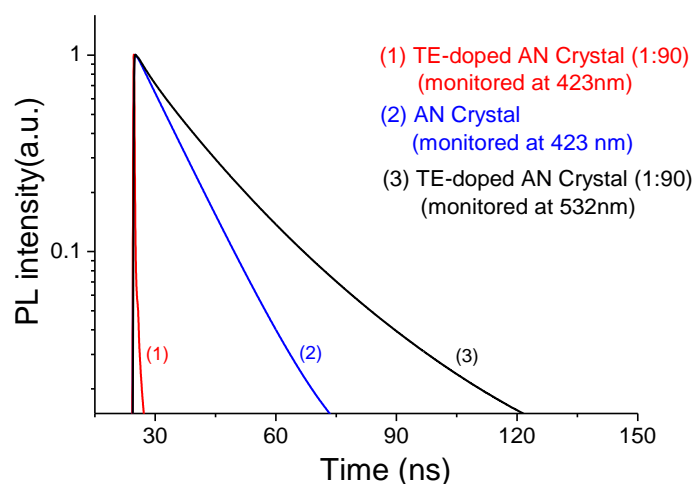


Figure 4.4. The time-resolved fluorescence of pure AN crystals and doped crystals at different emission wavelength $\lambda_{em}=423$ nm and 532 nm.

The rate of energy transfer from the donor to the acceptor $k_{ET} = 1/\tau_{DA} - 1/\tau_D$ is calculated from table 4.1, and the value equals to $8.99 \times 10^9 \text{ s}^{-1}$, and the efficiency of energy transfer $\Phi_{ET} = \tau_D k_{ET} / (\tau_D + k_{ET})$ is 98.9%, which is a superb high value explained all the aforementioned phenomenon.

Table 4.1. Decay data of the AN crystal and Doped crystal

Crystal	Decay time τ (ns)	Percentage (%)	Mean lifetime τ (ns)	λ (nm)
AN	10.30	100	10.30	423
TE-doped AN	0.083	97.34	0.11	423
	0.91	2.53		
	6.21	0.13		
TE-doped AN	2.76	9.56	18.79	532
	12.90	58.48		
	26.93	31.97		

4.3.2 Optoelectroic properties of CNDPASDB-doped *trans*-DPDSB crystals

Crystal quality of doped crystals

Crystal quality of doped crystals with the ratio of 1-200 (figure 4.5a, b) and 1-50 (figure 4.5c, d) were characterized by polarized optical microscopy. In this measurement, polarizer and analyzer are vertical with each other, light cannot transmit unless optical axis of anisotropic crystals have different angle with them. On the other hand, anisotropic crystals will turn into totally dark if their optical axis have the same direction with ether polarizer or analyzer. So if there is phase separation in a crystal, its polarized optical image cannot be totally dark due to the random optical axes of crystalline phases. Figure 4.5 illustrate that the guest content shows no evident influence on the shape and size of the as-prepared crystals. Furthermore, doping CNDPASDB (even in the high doping ratio of 1-50) caused no phase separation in *trans*-DPDSB because crystals in the red circles became totally dark when their long axes had the same direction with polarizer or analyzer. In other words, CNDPASDB molecules replaced those of *trans*-DPDSB in the crystal matrix instead of aggregating into their own crystalline grains.

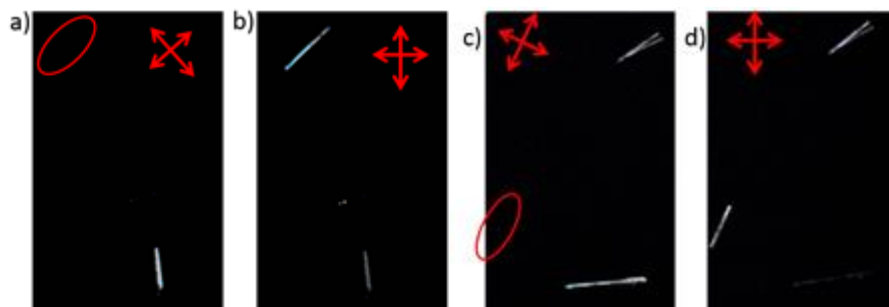


Figure 4.5. Polarizing optical images of doped crystals in the ratio of (a), (b) 1-200, and (c), (d) 1-50. (a) and (c) show crystals in the red circles turn into totally dark when optical axes of crystals parallel to polarizer or analyzer; (b) and (d) are the cases that optical axes have different angle with polarizer and analyzer.

Improvement of optical properties

Figure 4.6 displays the photoluminescence spectrum of pure *trans*-DPDSB (dark blue curve) and absorption spectrum of CNDPASDB (black curve). The good spectra overlap between them ensures efficient energy transfer from the host molecules to those of guest.^[135] Emission spectra of doped crystals with different doping ratio are also illustrated in figure 4.6. Pure *trans*-DPDSB exhibits its luminescence emission with the peak at 439 nm and a shoulder at around 462 nm. As for doped crystals, their emission spectra cover all over the region from 400 nm to 700 nm. All the spectra show the same shape as that of pure *trans*-DPDSB at blue light-emission region (400 nm-500 nm) in accompany with a broad peak at around 558 nm which booms with increasing the doping ratio. CNDPASDB single crystal shows an emission peak at 572 nm in our experimental result. Accordingly, aggregation will cause a red-shift of emission spectrum, which further proved CNDPASDB molecules disperse in the host matrix instead of aggregating into small crystalline grains. The emission spectra of different doping ratios also show distinctively different relative intensities at the region of 500-700 nm where guest material emits light, and the higher doping ratio is the stronger relative intensity at this region they have. Such special property insured color tunable light emission (including white light emission) in these doping systems being possible. Table 1 illustrates optical photographs of pure *trans*-DPDSB crystal and doped

crystals under the ultra-violet illumination. With increasing the doping ratio, light emission color are tuned from blue (pure *trans*-DPDSB) to blue-green (1-200), white (1-75) and pale yellow (1-50), which correspond well to the boom of broad peak at 558 nm with increasing the doping ratio.

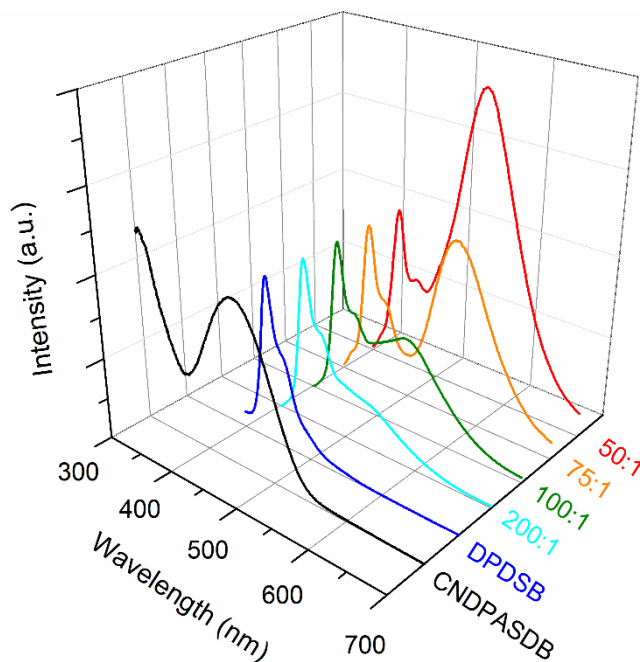
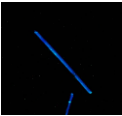
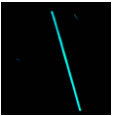



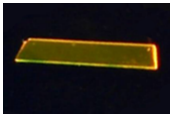


Figure 4.6. Absorption spectrum of CNDPASDB thin film (black line) and PL spectra of pure and doped DPDSB crystals (colored lines).

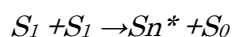
To investigate the luminescence efficiency of the doped crystals, the crystalline-state quantum yields of the pure and doped crystals were recorded. Table 4.2 shows the quantum yields of different doping concentrations excited by UV light at 380 nm. After doping, significant enhancement in quantum yield has been observed that about 20% of quantum yield has been improved after doping. This result indicated that the energy had been effectively transferred from the lower efficiency host material to the guest material with superb high luminescence efficiency. Such phenomenon just corresponds to the mechanism of Förster energy transfer which needs the efficient spectrum overlap between the donor emission and the acceptor absorption. In our doping system, the emission spectrum of DPDSB as host material is fully covered by the absorption spectrum which indicates that energy transfer will be superb efficient. The doped crystals

possess such high PL efficiency (about 80%) which can be comparable with that in solution. This is because of the relatively high PL efficiency in pure *trans*-DPDSB crystal (nearly 60%) that even energy transfer show superb high efficiency from the host molecules to the guest molecules, emission from host will not weaken.

Table 4.2. Optical photographs of crystals illuminated by ultra-violet light and external quantum yield (EQY) values of pure DPDSB crystal, CNDPASDB-doped DPDSB crystals and CNDPASDB crystal, respectively.

Ratio	DPDSB	1-200	1-100	1-75	1-50	CNDPASBSDB
PL Figure						
EQY (%)	58.1	82.9	80.2	79.7	77.1	30.3

Another issue must be figured out is that the quantum yield slightly decreases when the doping concentration rises. This phenomenon can be attribute to concentration quenching. According to the lattice constants of *trans*-DPDSB crystal, the molecular density is calculated to be $1.618E^{21}$ molecules/cm³. Exciton diffusion length in organic crystals is about 5 nm, which means that number of molecules in the sphere of this radius is 202. This result indicates that when the doping ratio is higher than 1:200, singlet-singlet annihilation will even occur between the doped molecules.^[3]



(Equation 4.1)

In this process, S_n^* will relax to S_1 in short order with radiation of heat, inducing decrease of luminescent efficiency.

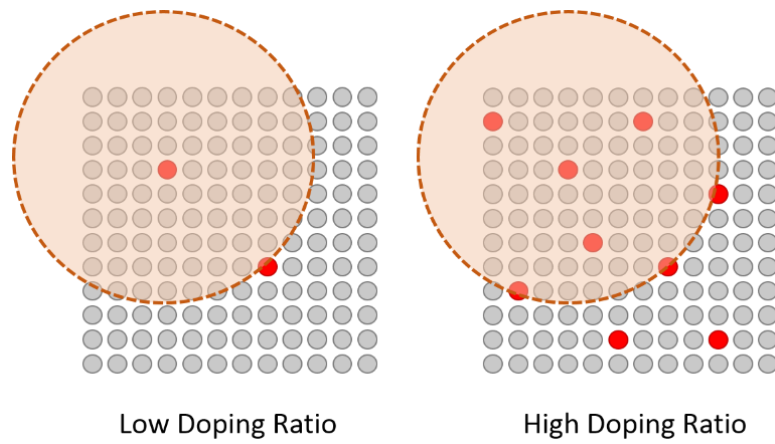


Figure 4.7. Schematics of the disturbance of crystal lattices when CNDPASDB molecules are doped into the *trans*-DPDSB crystal with low and high doping ratio.

Grey dots are *trans*-DPDSB molecules and red dots are CNDPASDB molecules.

Radius of the red circle is the excion diffusion length.

Transport properties after doping

The transport properties of both pure *trans*-DPASDB and doped crystals were characterized by FET device measurement. For enhancing the carrier injection, asymmetric electrodes (Au-Ca) were used and buffer layer were introduced between the gate electrode and organic semiconductor.

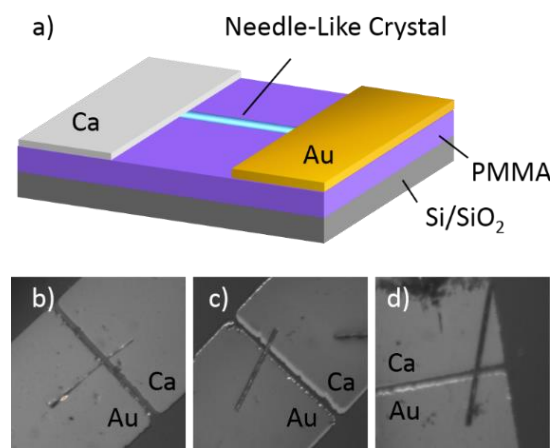


Figure 4.8. (a) Schematic diagram of device configuration and top-view photographs of devices: (b) pure *trans*-DPDSB crystal, (c) crystal with doping ratio of 1-200 and (d) crystal with doping ratio of 1-75.

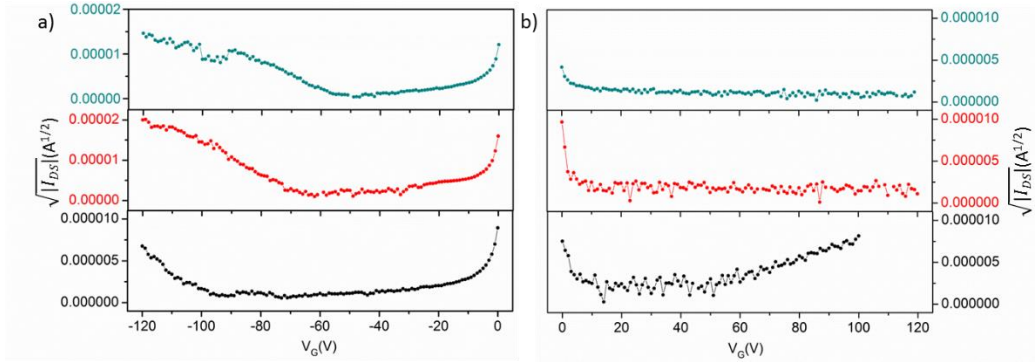


Figure 4.9. (a) p-type and (b) n-type FET transfer curves of pure (black), 1-200-doped (red) and 1-75-doped (dark cyan) DPDSB crystals, respectively.

Figure 4.9 shows the transfer characteristics of top-contact p- and n-type OFETs based on these one-dimensional crystals. For pure *trans*-DPDSB crystal, both n- and p-type FET operations were observed under applied negative and positive V_{GS} with a saturated hole mobility of $\mu_h = 1.09 \times 10^{-4} \text{ cm}^2\text{V}^{-1}\text{s}^{-1}$, and a saturated electron mobility of $\mu_e = 2.37 \times 10^{-5} \text{ cm}^2\text{V}^{-1}\text{s}^{-1}$. While only p-type characteristics showed in doped crystals, $\mu_h = 3.25 \times 10^{-4} \text{ cm}^2\text{V}^{-1}\text{s}^{-1}$ for the doping ratio of 1:200 and $\mu_h = 1.51 \times 10^{-4} \text{ cm}^2\text{V}^{-1}\text{s}^{-1}$ for the doping ratio of 1:75, which indicates the structural ordering maintenance of the doped crystals could ensure hole carrier mobility comparable to that of pure *trans*-DPDSB. Meanwhile, the electron mobility could not be observed because the dopant CNDPASDB molecules induces electron traps with a depth of about 0.57 eV. The non-balanced transport of hole and electron-carriers is unfavourable to realize a luminescence of doped crystal using light-emitting FET devices.

Here, the reasons why pure *trans*-DPDSB crystal exhibits low carrier mobility are discussed. Firstly, *trans*-DPDSB molecules follow a cross-stacking mode in this needle-like crystalline form. Though the overlapped central phenyl rings along b axis may form a transport channel for charge carriers, the mean interaction between two adjacent molecules is CH/ π hydrogen bonds, which cannot provide any carrier-transport channel. Secondly, the contact areas between crystals and substrates were much smaller than those we estimated (diameter \times channel length) due to their needle-like morphology. Moreover, diameters of crystals which were applied on the FETs are in the range of several

micrometers while thickness of electrodes are much thinner. Both field-effect and carrier injection could be problems for obtaining real carrier mobility.

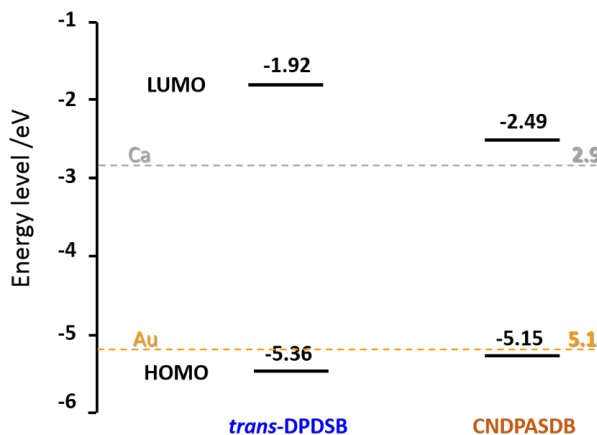


Figure 4.10. Calculated frontier orbitals of *trans*-DPDSB and CNDPASDB.

4.4 Conclusions

In this chapter, tetracene-doped anthraene crystal is employed as a model for studying doping system based on RET theory. Both the fluorescent spectra and much more improved luminescent efficiency proved that there was an efficient energy transfer from the donor AN molecule to the acceptor TE molecule. The efficient of energy transfer with superb high value was calculated from data collected in the measurement of time-resolved fluorescence.

Furthermore, we have successfully overcome the differences of molecular structures and their stacking modes, finally doped a certain quantity of CNDPASDB into *trans*-DPDSB by solution growth method, and maintained the original crystal structure of host crystal as proved by polarizing optical microscope analysis. Light emission color can be tuned by changing the doping ratio, due to intrinsically high QY of the host material and efficient energy transfer from *trans*-DPDSB molecules to CNDPASDB molecules. Therefore, emission spectra can cover both the emission region of the host (blue color) and that of the guest (orange color). With suitable balance of the ratio between host and guest, white light emission was successfully obtained. Moreover, superb high EQY (~80%) comparable with that in solution was obtained by doping, and it slightly decreased

with increasing the doping ratio due to the singlet-singlet annihilation. Finally, carrier transport characteristic was also investigated in both pure *trans*-DPDSB and its doped crystals. It is concluded that dopant with smaller energy band gap may introduce carrier-traps.

Chapter V

Long-Range Exciton Diffusion in Tetracene Crystal

5.1 Introduction

Exciton diffusion length (L_{EX}) is treated as an important parameter of organic semiconducting crystals, due to the significance to organic optoelectronics, such as organic photovoltaics, light-emitting devices and electrically driven lasers.^[136, 137] However, there was few ways to determine the exact value of exciton diffusion length.^[138, 139] The first reason is that the lifetime of singlet is too short in crystalline state to measure its diffusion length. The second reason is some organic crystals possess a fake long-range exciton diffusion length due to the trivial re-absorption in crystalline state, and anthracene is a typical example that the measured exciton diffusion length reached to micrometer-scale.^[71-73] Thirdly, the drawbacks of typical device construction induced inaccurate results which will be discussed afterwards.

Electronic devices based on molecular crystals emerged as a platform for investigation of intrinsic electronic properties of organic semiconductors. In 2010, H. Najafov *et al.* evaluated the excitonic energy transport in a disorder-free organic semiconductor.^[140] In their report, polarization- and wavelength-dependent photocurrent excitation spectra, photoluminescence (PL) quenching and time-resolved PL were investigated in highly ordered, ultrapure molecular crystals of rubrene. The horizontal device structure of photoconductivity measurement avoid the drawbacks in typical Schottky diode configuration.^[141] They concluded that the latter metal/organic/metal sandwich

construction usually leads to inaccuracies because of the optical interference effects, enhanced quenching of excitons near the metal/organic interface, as well as transmission losses through a metal film and considerable penetration of metal into the metal/organic layer during the contact deposition.^[142] The exciton diffusion length corresponding is found to be in the range of 3~8 μm . Furthermore, they confirmed the obtained result by simulations of photoconductivity accompanied with measurement of PL quenching and time-resolved photoluminescence. They also speculated that diffusion occurs by means of the Dexter process known to govern the motion of triplet excitons in organic semiconductors.^[143, 144] The triplet excitons are primarily generated by means of fission of singlet.

Singlet fission as introduced in chapter 1 is a process in which an organic chromophore in a singlet state shares its excitation energy with a neighboring ground-state chromophore and both are converted into triplet state.^[74, 145] This process can be treated as a special case of internal conversion, which is in a ps or even sub-ps time scale in molecular crystals.^[83] Singlet fission in tetracene single crystal was observed and proposed in 1968,^[146] which might be the first report in molecular crystal. In 2014, G. M. Akselrod *et al.* reported a spatial, temporal and spectral visualization of exciton transport in crystalline and thin-film state of tetracene.^[147] They revealed that exciton transport occurs by random walk diffusion. However, their report was about triplet excitation diffusion in (a, b) facet of tetracene crystal, no mention about that along the c axis which is vertical to the (a, b) facet.

In this chapter, we measured the exciton diffusion length along the c axis in tetracene single crystal. Combining the data of polarization-dependent absorption coefficient and photo current characterizations, we finally obtained the exciton diffusion length along c axis to be 1.87 μm . This result is significant to our following experiments in chapter 6, in which carrier-transport and light-emission functions can be separated into two crystalline layers, and this device configuration is a promising candidate for realizing electrically driven lasers.

5.2 Experimental Section

Crystal growth - Tetracene was purchased from Aldrich (99.9%). Single crystals were grown by physical vapor transport technique in a steam of argon gas (99.9999%). Three-zone electric furnace was employed and the condition of crystal growth was introduced in chapter 2.

Absorption coefficient - The angular dependence of absorption coefficient, $\alpha(\theta)$, measured by recording an optical transmission through a very thin platelet-like tetracene single crystal.

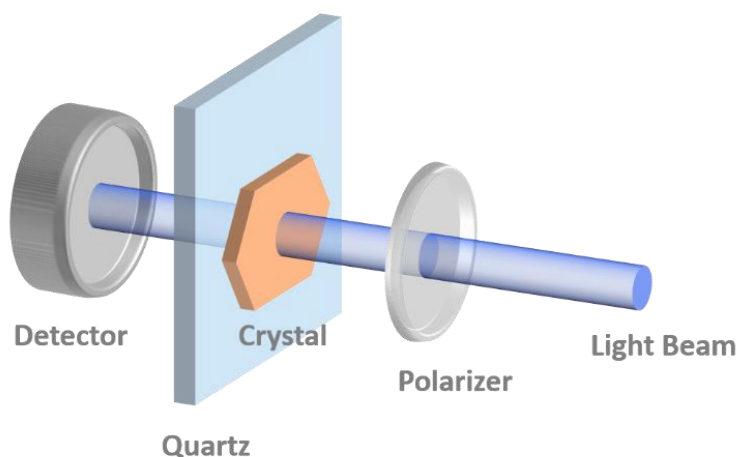


Figure 5.1. Schematic diagram of angular-dependent absorption coefficient measurement. Platelet-crystal was laminated on a quartz substrate. Light source with wavelength at 400 nm is provided by a continuous laser. A linear polarizer can produce angle-tunable polarized light. Light intensities of with- and without-tetracene are measured by a power detector.

Photocurrent - The measurements were carried out on the largest natural facet of the crystals, the (a, b) facet, in a coplanar contact configuration. Electrical contacts have been prepared by silver paste, and photocurrent was measured by source meter Keithley K2400. The crystal surface was illuminated at normal incidence using monochromatic light with wavelength at 400 nm obtained by a continuous laser emitter. A linear polarizer was used to produce polarized light.

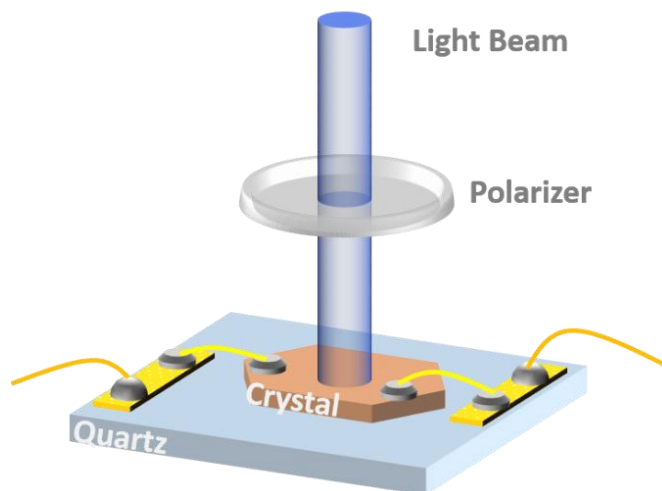


Figure 5.2. Schematic diagram of polarized dependent photocurrent measurement. Platelet-crystal was laminated on a quartz substrate. Gold and copper wires as well as circuit board stickers were used to connect crystal and the source meter. Gold wires were firmed by silver paste and copper wires were firmed by solder.

Crystal thickness - Crystal thickness was measured by a Veeco Dektak 150 surface profiler scanning over the whole length of the crystal placed on a quartz substrate.

5.3 Theoretical Basis

5.3.1 Polarized Absorption Coefficient

Due to the highly ordered aggregation of molecules, organic crystals has an optical anisotropy characteristic. Tetracene crystal has space group $P\bar{1}$, but the structure has a symmetry close to $P2_1/a$, and the largest natural facet is (a, b) facet in tetracene single crystal, these result in maximum and minima of absorption coefficient, $\alpha(\theta)$, occurring at polarizations along the b and a axes, respectively (see figure 5.3). This angular dependence of α allows us to modulate the characteristic depth of exciton photo-generation profile in the crystal α^1 .

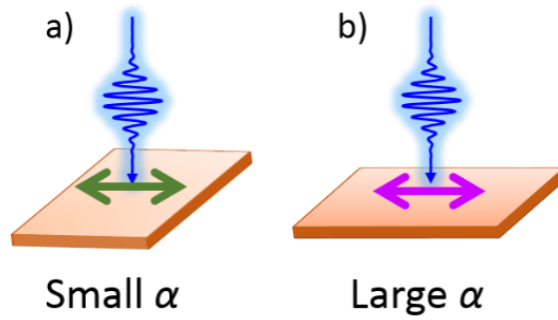


Figure 5.3. Schematic diagram of anisotropic characteristic of absorption coefficient. a) is the minima value occurring at polarizations along the a axis, b) is the maximum value along the b axis.

5.3.2 Photoconductivity

Corresponding to the polarized absorption coefficient, the photoconductivity in tetracene crystal also exhibits periodic modulations with polarization angle. It has been proved that photoconductivity in crystal is due to exciton migration through a surface layer of finite thickness L_{EX} and exciton dissociation.

Due to the Beer-Lambert law, light intensity in a medium has an exponential decay, the probability of this long-lived triplet excitons, created at a depth x from the surface, to reach the surface is $\exp(-x/L_{EX})$. Moreover, the portion of the photo flux absorbed within a layer of the crystal from x to dx is $d\Phi = \alpha \cdot \Phi_0 \cdot \exp(-\alpha x) \cdot dx$, where Φ_0 is the incident photo flux. Hence, photoconductivity will be proportional to an integral of $\alpha \cdot \Phi_0 \cdot \exp(-\alpha x) \cdot \exp(-x/L_{EX}) \cdot dx$ from $x=0$ to ∞ :

$$\begin{aligned}
 \sigma(\theta, \lambda) &= \sigma_0 + \sigma_{surf} \\
 &= \sigma_0 + \gamma_0 \chi_0 \Phi_0 \alpha \times \int_0^{\infty} \exp(-\alpha \cdot x) \\
 &\quad \cdot \exp\left(-\frac{x}{L_{EX}}\right) \cdot dx \\
 &\approx \gamma_0 \chi_0 \Phi_0 \frac{\alpha L_{EX}}{\alpha L_{EX} + 1}
 \end{aligned}$$

(Equation 5.1)

Where the quantum efficiency of generation of triplet excitons is χ_0 , the bulk σ_0 is negligible, and γ_0 is quantum efficiency of exciton dissociation at a free surface of rubrene. Therefore, the relative amplitude:

$$\eta_\sigma \equiv \frac{I_{MAX} - I_{MIN}}{I_{MAX}} = \frac{\sigma_b - \sigma_a}{\sigma_b}$$

$$1 - \frac{\alpha_a \cdot (\alpha_b L_{EX} + 1)}{\alpha_b \cdot (\alpha_a L_{EX} + 1)}$$

(Equation 5.2)

From the experimental result of η_σ , α and equation 5.2, L_{EX} will be obtained.

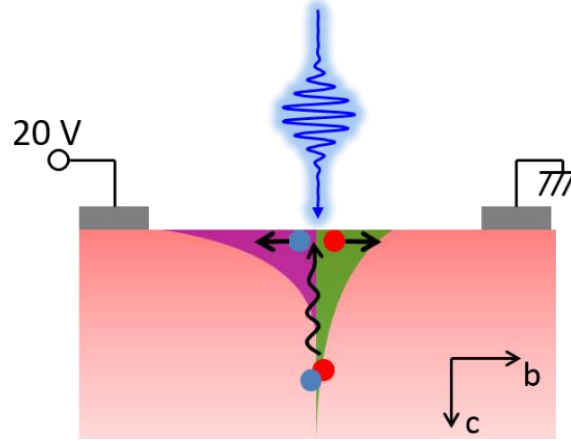


Figure 5.4. Schematic side view of the device showing electrical contacts at the (a, b) facet of tetracene crystal probing the photocurrent responds of the sample to the polarized incident light. An exponential profile of the photo-generated excitons is shown.

5.4 Results and Discussions

As mentioned above that polarization dependence of absorption coefficient was measured. Wavelength of incident light was fixed to 400 nm, and we measured the intensity of the incident light against polarization angle $I_0(\theta)$, then light intensity $I(\theta)$ transmission through tetracene single crystal was recorded.

$$\text{Abs} = \log\left(\frac{I_0}{I}\right) = 0.434\alpha l$$

(Equation 5.3)

Where α is the absorption coefficient and l is the light transmission length, here is the thickness of the tetracene crystal. Therefore, we can get the absorption coefficient, $\alpha(\theta)$:

$$\alpha(\theta) = \frac{1}{0.434l} \log\left(\frac{I_0(\theta)}{I(\theta)}\right)$$

(Equation 5.4)

The thickness of tetracene single crystal is $1.064 \mu\text{m}$ measured by surface profiler. Calculated result of $\alpha(\theta)$ is shown in figure 5.5, $\alpha_{\text{MAX}} = 12.2945 \times 10^3 \text{ cm}^{-1}$ and $\alpha_{\text{MIN}} = 6.649 \times 10^3 \text{ cm}^{-1}$.

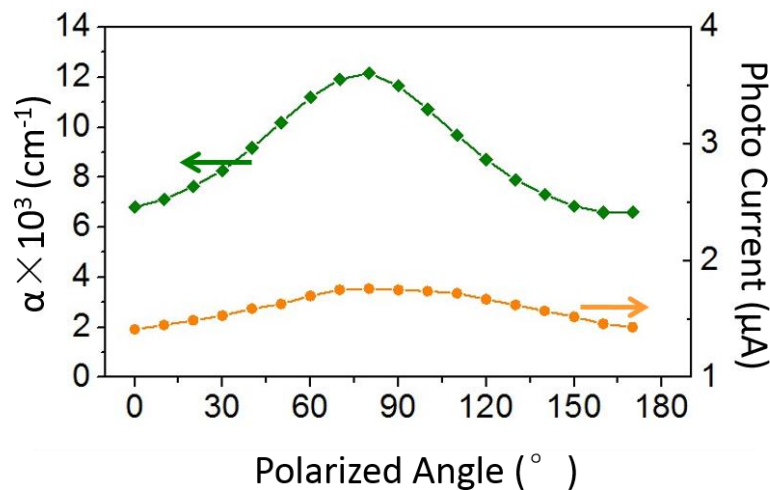


Figure 5.5. Angler dependence of the absorption coefficient illustrated by a 400 nm blue light source (filled olive squares). Also shown is experimental dependence of the photoconductivity on the polarization angle of a 400-nm excitation (filed orange circles).

Schematic diagrams of device configuration are shown in figure 5.2 and 5.4. The photocurrent in macroscopically thick tetracene crystals ($4.87 \mu\text{m}$) exhibits a periodic modulation corresponding to the polarization angle-dependence absorbance coefficient (figure 5.5, filed orange circles). The amplitude of this

modulation $\eta_0 = (I_{\text{MAX}} - I_{\text{MIN}}) / I_{\text{MAX}}$ was 20.45% calculated according to the as shown data. According to equation 5.2, the exciton diffusion length along c axis in tetracene crystal is calculated to be 1.8737 μm . This micro-scale result corresponds well to the reports about singlet fission in tetracene crystal, and triplet excitons are further generated with long lifetime and long diffusion range.

5.5 Conclusions

In this chapter, exciton diffusion length along the c axis in tetracene single crystal was determined. It is confirmed that due to the highly ordered molecular aggregation, tetracene single crystal has an optically anisotropic characteristic. The absorption coefficient in tetracene single crystal has a performance of polarization-dependence, which results in a similar modulation of photocurrent. Combining the data of absorption coefficient and photocurrent characterizations, the exciton diffusion length along c axis was calculated to be 1.87 μm . This micro-scale result corresponds well to the reports about singlet fission in tetracene crystal and triplet excitons are further generated with long lifetime and long diffusion range. Also, this long-range exciton diffusion length along c axis is significant to our following experiments in chapter 6, in which carrier-transport and light-emission functions can be separated into two crystalline layers, and this device configuration is a promising candidate for realizing electrically driven lasers.

Chapter VI

Separation of Carrier-Transport and Light-Emission Functions

6.1 Introduction

Electrically driven lasers based on organic semiconductor is still a challenge. Scientist from physics, chemistry as well as materials spared no efforts to realize it, but no one has succeed to date.^[59, 63, 148] There are still some issues to be satisfied. For example, population inversion must be provided by sufficient exciton density, which is governed by carrier mobility. On the other hand, high luminescent efficiency is also a crucial factor for realizing lasers that they are capable to reduce the nonradiative losses caused by quenching and supplement the photo absorbed by electrodes.

Many groups have spent a lot of efforts on challenging this tough task. Takenobu group reported the spectral evolution accompanied by the spectral narrowing in 2009, but that narrowing was incomplete (no specific number being given in the literature)^[55]. In their report, a 5,5''-bis(4-biphenyl)-2,2':5',2''-terthiophene (BP3T)^[149] single crystal was applied as the organic semiconductor layer. They concluded that the current density attained on the LE-FET 412 A/cm² was two orders of magnitude lower than that for the threshold 10.3 kA/cm².

Still materials with both high carrier mobility and high luminescent efficiency is demanded, but these two factors are conflicted with each other.^[150] High carrier mobility demands for large overlap of delocalized conjugation electrons, while high luminescent efficiency needs a certain distance between transition dipoles to reduce quenching. It means that material itself cannot solve the present challenge.

Therefore, a novel device configuration is demanded. Our basic concept is dividing the carrier-transport and light-emission into two layers and making the combination of these two layers act as the active layer in light-emitting transistors.

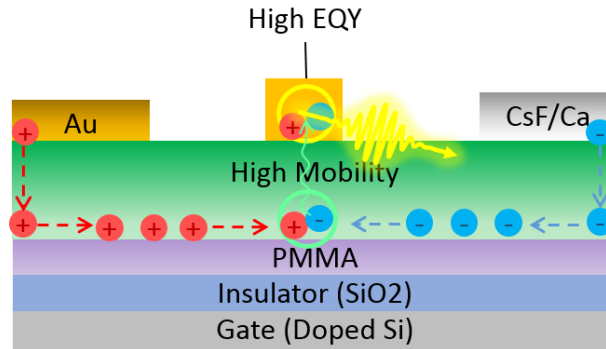


Figure 6.1. Schematic side-view diagram of bilayer light-emitting transistors. Green layer at bottom stands for carrier transporter, top layer act as light emitter. After electrons and holes accumulation, they will have a recombination to form excitons at bottom layer. Then excitons diffuse to the top layer with light emission.

Figure 6.1 illustrates the schematic diagram of bilayer transistors. The bottom crystal which has high carrier transport acts as carrier transporter and top crystal with high luminescent efficiency is assigned as light emitter. The working mechanism can be described as follows: after the electrons and holes accumulated at the interface between bottom crystal and PMMA layer, recombination occurs in the device channel and form excitons, formed excitons then diffused to the top crystal with light emission.

Two issues must considered of this device configuration: i) The accumulation layer of carriers is about 1 nm in thickness,^[60] which is much thinner than the crystal (several hundred nanometers). It means that the excitation diffusion length must be larger than the thickness of crystal, otherwise the excitons cannot survive to the top layer. ii) The energy bandgap of the top crystal must no larger than that of the bottom crystal. It is energy forbidden for an exciton transfer to a material with larger energy bandgap, and the generated excitons will be confined in the bottom crystal with waste of energy.

According to the results obtained in chapter 4, doping can increase the

luminescent efficiency.^[111] Moreover, there is no change of energy bandgap after doping. These two facts indicate us that doped crystal can be a good light emitter in our device construction. On the other hand, in chapter 5, due to the delayed fluorescence^[74, 83] (see figure 6.2) exciton diffusion length along the *c* axis in tetracene crystal was determined to be 1.87 μm , which is much larger than crystal thickness. Due to the high carrier mobility^[27, 54] (see chapter 2) and the long exciton diffusion length in crystalline state, tetracene crystal is chosen as bottom layer in our device structure, and doped tetracene crystal is assigned as light emitter.

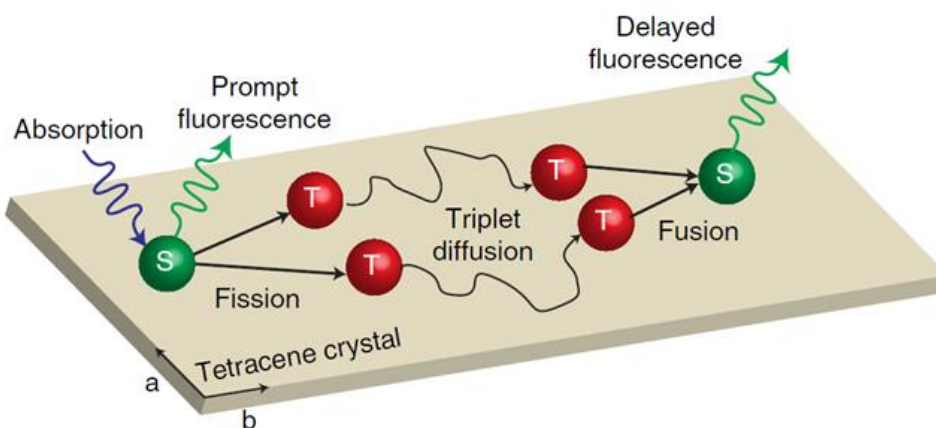


Figure 6.2. Schematic diagram of delayed fluorescence, i. e. singlet fission and triplet fusion. Incident light will generate a singlet, and this singlet will share energy with its adjacent molecule forming two triplets (red dots), which have long lifetime and diffusion length. Finally, two triplets can form one singlet after long-distance diffusion.

As for the dopant, 4-(dicyanomethylene)-2-methyl-6-(*p*-dimethylaminostyryl)-4H-pyran (DCM1) is a broadly used material in fabrication of both OLEDs^[151] and LE-FETs^[56] for increasing the external quantum efficiency (EQE). According to the energy band diagram illustrated in figure 6.3, the energy bandgap for tetracene and DCM1 are 2.74 eV and 2.1 eV, respectively. This energy bandgap difference indicates an efficient energy transfer^[135] from host tetracene molecules to the guest DCM1 molecules. Therefore, DCM1-doped tetracene crystal is employed as the light emitter.

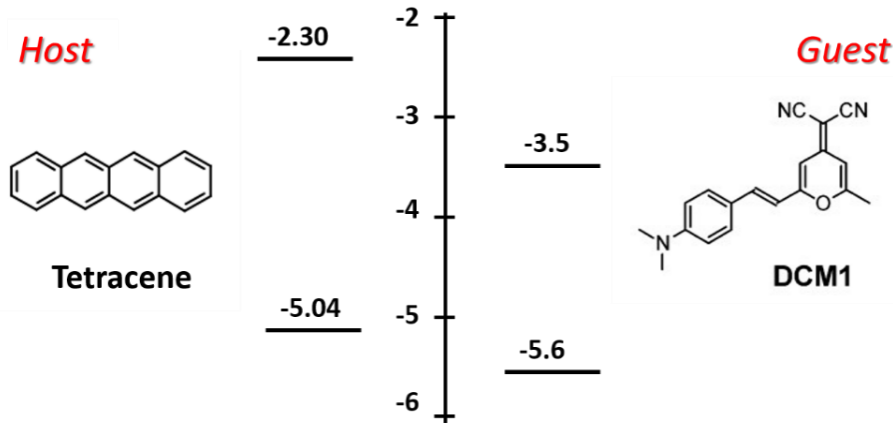


Figure 6.3. Calculated frontier orbitals of the host tetracene and guest DCM1. The energy bandgap for tetracene and DCM1 are 2.74 eV and 2.1 eV, respectively, which means energy can transfer from the host tetracene to the guest DCM1.

In this chapter, DCM1-doped tetracene crystals were prepared by using physical vapor transport method.^[31] Their crystalline phase were characterized by polarizing optical microscope. Optoelectronic properties including luminescent spectra, external quantum yield as well as carrier transport were characterized in both pure and doped tetracene crystals. Bilayer transistor composed with tetracene crystal as carrier transporter (bottom layer) and DCM1-doped tetracene crystal as light emitter (top layer) was fabricated. To balance the electron- and hole-injection, CsF^[152, 153] was insert between Ca and tetracene crystal. Red light emission from top crystal which is different from that in tetracene (green light-emission color) was observed. This result proved our anticipation that excitons were form in the bottom crystal and transferred to the top crystal with light emission. To further prove this mechanism, an insulator TTC thin film was inserted between tetracene crystal and DCM1-doped crystal, only green light emission was observed in the device, which means excitons were blocked by TTC thin film. We finally realized the separation of carrier-transport and light-emission functions by fabricating a bilayer light-emitting transistor.

6.2 Experimental Section

Preparation of Samples - Tetracene (99.9%) and DCM1 (98%) was purchased from Aldrich. Both pure and doped tetracene crystals were grown by physical vapor transport in a stream of argon gas (99.9999%).

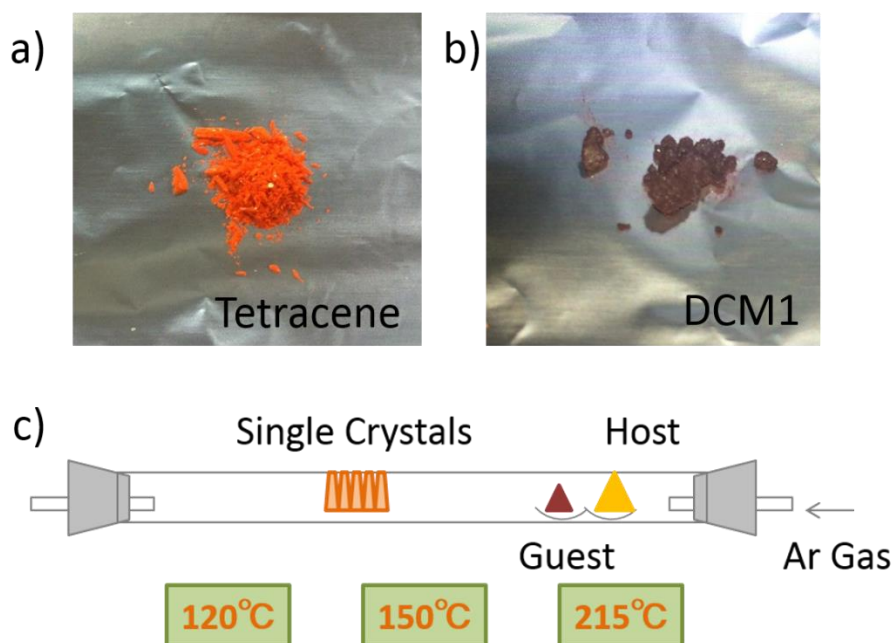


Figure 6.4. a), b) are photographs of host material tetracene and guest material DCM1 in powder form. c) Schematic figure of DCM1-doped tetracene crystal grown by PVT method.

Crystal Quality - Crystalline phase were characterized by polarizing optical microscope.

Optical Properties - Absorption spectra were obtained from UV/vis spectrophotometer (JASCO: V-650DS), and fluorescent spectra were obtained by using fluorescent spectrophotometer (HITACHI: F-7000) with the excitation wavelength at 380 nm. PLQY were measured by a photo-counting method using an integration sphere on a Hamamatsu Photons C9920-02 spectrometer.

FET Device Fabrication - A highly n-type doped silicon wafer with a 300 nm thick SiO₂ film was used as a gate dielectric. For minimizing the electron traps at the interface between the gate and organic semiconductor, a 30 nm thick PMMA film was spin-coated on the SiO₂ surface from the toluene solution as the buffer layer. The whole gate substrate was heated overnight at 75°C in the argon atmosphere. Doped crystals were drop-casted on the substrate by using methanol. Au (100 nm

in thickness) and Ca (500 nm in thickness) for hole and electron injecting electrodes were deposited on the single crystal by vacuum evaporation with the shadow mask technique.

Bilayer Transistor - the DCM1-doped crystal was laminated on the center position of the tetracene crystal. Au and CsF/Ca were deposited separately, the thickness of CsF is about 1 nm. Thicknesses of Au and Ca are the same as those described above. There was no contact between top crystal and electrodes during the device fabrication.

TTC insertion - a certain area TTC thin film with thickness of 6 nm was deposited on the center position of the tetracene crystal, then DCM1-doped tetracene crystal was laminated on the TTC thin film. The following procedures were the same as fabricating a regular bilayer transistor.

Theoretical Calculations - All quantum chemistry calculations were performed on the Gaussian 03 package. The molecular orbital energies of tetracene were calculated by B3LYP/cc-pVDZ, which is a hybrid method of DFT and Hartree-Fock method.

6.3 Results and discussion

6.3.1 DCM1-Doped Tetracene crystal

Crystal quality of doped crystals

Crystal quality of DCM1-doped tetracene crystal was characterized by polarized optical microscopy. In this measurement, polarizer and analyzer are vertical with each other, light cannot transmit unless optical axis of anisotropic crystals have different angle with them. On the other hand, anisotropic crystals will turn into totally dark if their optical axis have the same direction with either polarizer or analyzer. So if there is phase separation in a crystal, its polarized optical image cannot be totally dark due to the random optical axes of crystalline phases. Figure 6.5 illustrate that the guest content shows no evident influence on the shape and size of the as-prepared crystals. Furthermore, doping DCM1 caused no phase separation in tetracene because crystals in the blue-dashed frame became totally dark when their long axes had the same direction with polarizer or analyzer. In other words, DCM1 molecules replaced those of tetracene in the crystal matrix

instead of aggregating into their own crystalline grains.

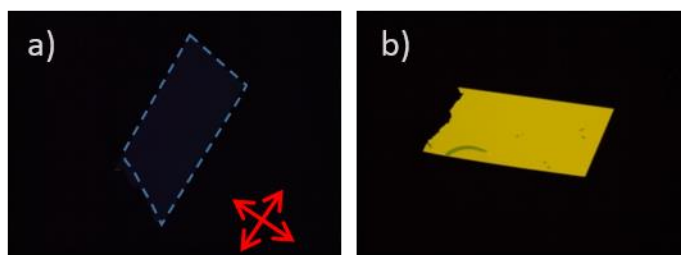


Figure 6.5. Polarizing optical images of DCM1-doped tetracene crystal. (a) shows crystal in the blue-dashed frame turns into totally dark when optical axes of crystals parallel to polarizer or analyzer; (b) is the case that the optical axis have different angle with polarizer and analyzer.

Improvement of optical properties

Figure 6.6 displays the photoluminescence spectra of pure tetracene crystal (green curve), the dopant DCM1 (red curve) and DCM1-doped tetracene crystal (orange curve). Pure tetracene crystal exhibits its luminescence emission with peaks at 539 nm, 574 nm, 615 nm with a small tail at around 673 nm. Emission from dopant DCM1 shows a broad peak at around 607 nm. As for the doped crystal, the emission spectrum covers all over the region from 500 nm to 700 nm, positions of the first three peaks are the same as those of pure tetracene. However, it is clear to observe that the fluorescent intensity of the doped tetracene has been enhanced at the wavelength of 610 nm, which means the dopant DCM1 has light emission in the doped crystal. The aforementioned phenomenon illustrates that both host tetracene and dopant DCM1 molecules emit light in the doped crystal, which means that energy transferred from tetracene molecule to DCM1 molecules but not drastically.

To investigate the luminescence efficiency of the doped crystals, the crystalline-state quantum yields of the pure and doped crystals were recorded. Figure 6.6 shows the quantum yields of crystals excited by UV light at 380 nm. After doping, an enhancement in quantum yield has been observed that about 7% of quantum yield has been improved. Such phenomenon just corresponds to the conclusion above that partial energy transferred from tetracene molecule to

DCM1 molecules.

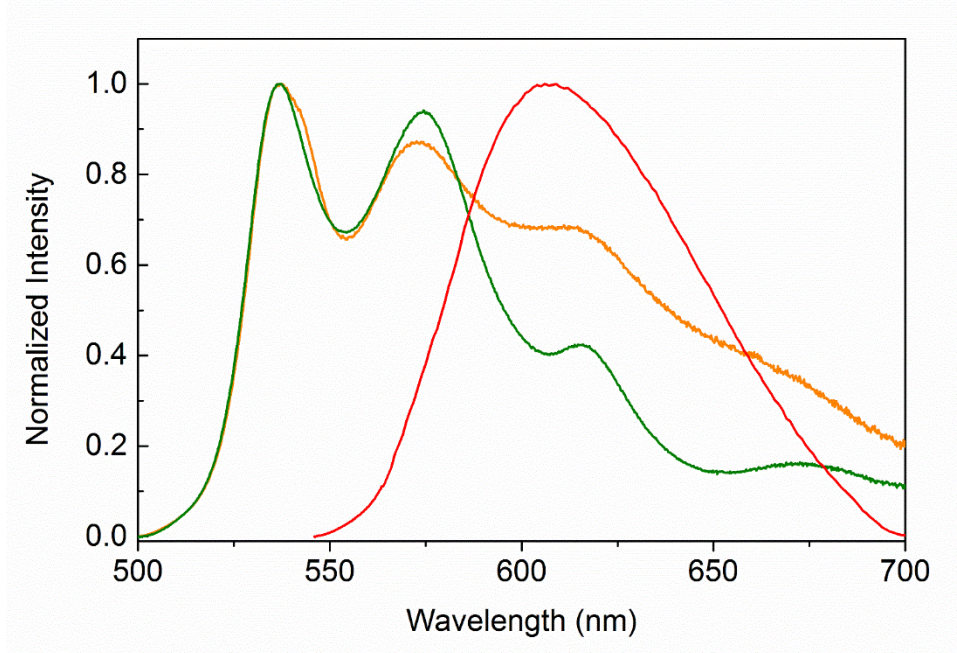


Figure 6.6. Steady-state fluorescent spectra of tetracene crystal (blue curve), DCM1 (red curve) and DCM1-doped tetracene crystal (orange curve).

Transport properties after doping

The transport properties of both pure tetracene and DCM1-doped tetracene crystals were characterized by FET device measurement. For enhancing the carrier injection, asymmetric electrodes (Au-Ca) were used and buffer layer were introduced between the gate electrode and organic semiconductor.

Figure 6.7 shows the transfer characteristics of top-contact p-type OFETs based on both pure and doped tetracene crystals. Both of them showed ambipolar behavior, and saturated carrier mobility of $\mu_h = 0.33 \text{ cm}^2\text{V}^{-1}\text{s}^{-1}$ and $\mu_e = 1.28 \text{ cm}^2\text{V}^{-1}\text{s}^{-1}$ were obtained in pure tetracene crystal. On the other hand, carrier mobility of doped crystal are as follows, $\mu_h = 0.12 \text{ cm}^2\text{V}^{-1}\text{s}^{-1}$ and $\mu_e = 0.13 \text{ cm}^2\text{V}^{-1}\text{s}^{-1}$, which indicates the structural ordering maintenance of the doped crystals could ensure hole carrier mobility comparable to that of pure tetracene. Meanwhile, the electron mobility was one order decreased due to the reason that the dopant DCM1 molecules induces electron traps with a depth of about 1.2 eV.

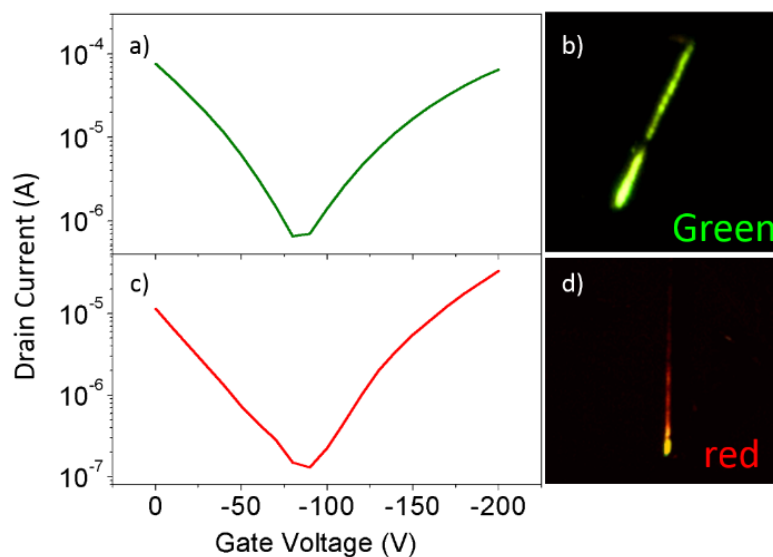


Figure 6.7. (a) and (c) are transfer curves of pure tetracene crystal (Green) and DCM1-doped tetracene crystal (red), respectively, V_D was -200 V and V_G varies from 0 V to -200 V. (b) and (d) are their electroluminescence photography, green light emission was obtained in pure tetracene crystal and red light emission was observed in DCM1-doped tetracene crystal.

6.3.2 Bilayer light-emitting transistor

After characterization of optoelectronic properties of DCM1-doped tetracene crystal, a bilayer transistor based on tetracene and its doped crystals was fabricated. The device configuration is illustrated in figure 6.8, to enhance the carrier injection, asymmetric electrodes (Au-CsF/Ca) were applied.

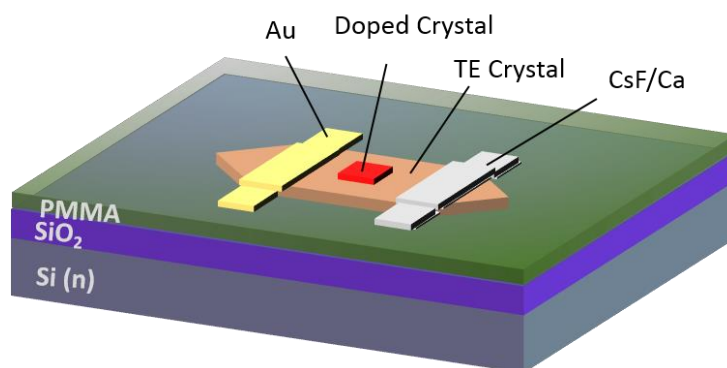


Figure 6.8. Schematic configuration of the bilayer transistor.

In this fabrication, CsF layer which can somehow bent the valence band and decrease the electron-injection barrier was inserted between tetracene crystal and Ca; On the other hand, Au directly contacts with the tetracene crystal without any disturbance from Ca, and the contact area becomes much larger than the regular device construction with enhancing the hole injection.

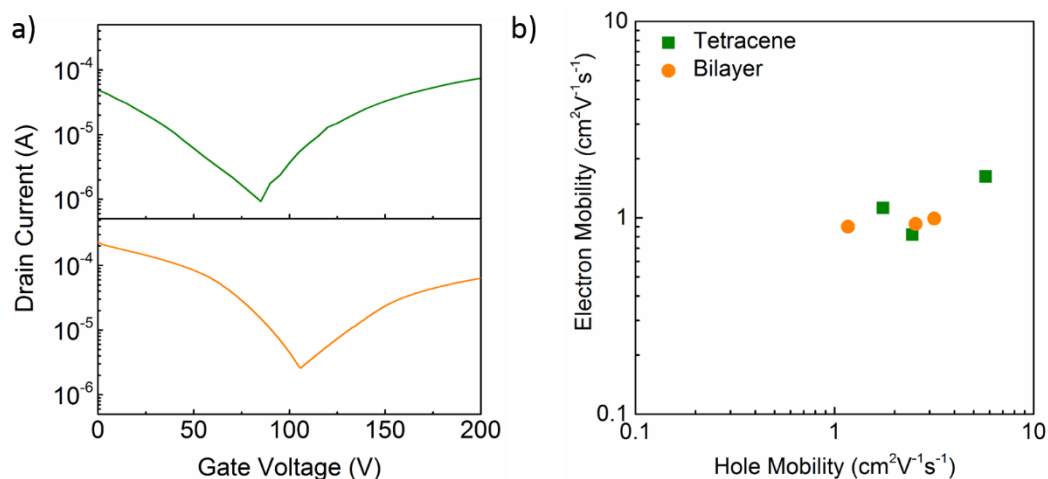


Figure 6.9. a) transfer curves of tetracene-crystal monolayer transistor (Green) and bilayer transistor based on DCM1-doped and pure tetracene crystals (orange), respectively, V_D was 200 V and V_G varies from 0 V to 200 V. b) mobility distributions of tetracene-crystal monolayer transistors (Green) and bilayer transistors (orange).

Figure 6.9a shows the transfer curves of tetracene-crystal monolayer transistor (Green) and bilayer transistor based on DCM1-doped and pure tetracene crystals (orange) under n-type operation. The transfer curves of these two transistors are in the same order, which illustrates that lamination of DCM1-doped tetracene crystal as top layer has no affection on carrier transport in the bottom layer. Further proof can be shown in figure 6.9b, the mobility distributions of both monolayer transistors (Green) and bilayer transistors (orange), in which no separation has been observed between them.

Figure 6.10a and b are the top-view photographs of the bilayer transistor configuration and that recording the light emission from it. Dramatically color difference of light-emission was observed in this bilayer transistor. The relative ratio of green and red value on top crystal is $189(\pm 39):119(\pm 29)$, which is more red

than that in the monolayer ($137(\pm 36):156(\pm 36)$). These phenomena proved the mechanics proposed above that exciton formed in the bottom crystal and diffused to the top crystal with red-light emission.

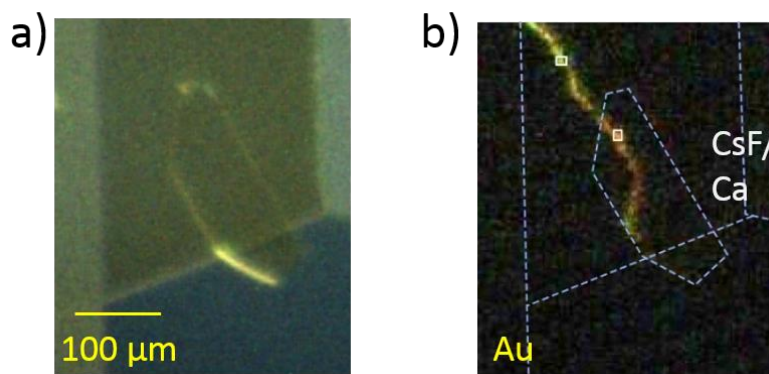


Figure 6.10. a) top-view photographs of the bilayer transistor configuration and b) the record of light emission from the bilayer transistor at ambipolar operation.

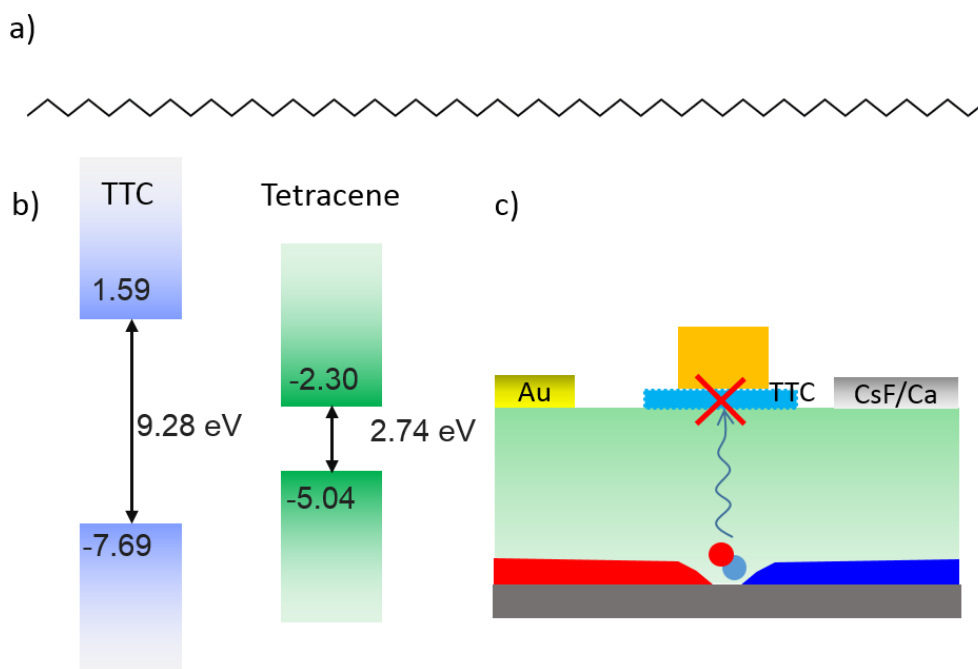


Figure 6.11. a) Molecular structure of TTC; b) Energy band diagrams of TTC and Tetracene; c) Schematic configuration of the bilayer transistor inserted with TTC thin film.

To further confirm whether the top crystal is excited by excitons transferred from bottom crystal or not, a $\text{CH}_3(\text{CH}_2)_{42}\text{CH}_3$ (TTC, figure 6.11a) thin film layer with thickness of 6 nm was inserted between tetracene and DCM1-doped tetracene crystals. Because TTC is an insulator with energy band gap of 9.28 eV (figure 6.11b), it can block the exciton diffusion between crystals, but also allow light propagation. Figure 6.11c shows the side-view diagram of bilayer transistor inserted with TTC thin film between tetracene and DCM1-doped tetracene crystals.

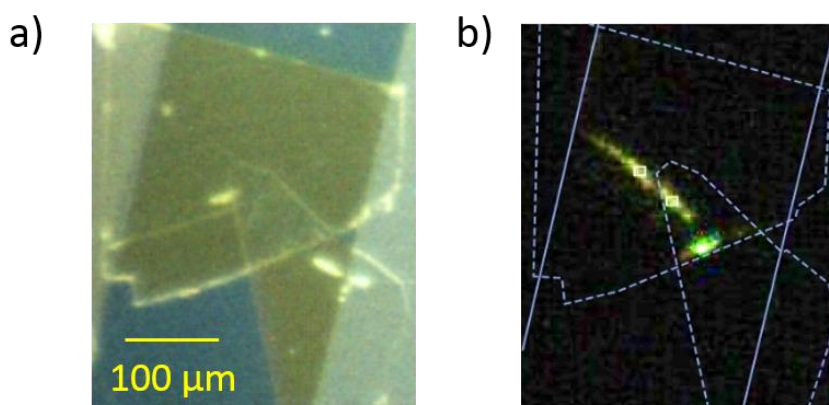


Figure 6.12. a) top-view photographs of the bilayer transistor with insert of TTC thin film and b) the record of light emission from this bilayer transistor under ambipolar operation.

Figure 6.12a and b are the top-view photographs of the bilayer transistor configuration and that recording the light emission from it. No color difference of light-emission was observed in this bilayer transistor after analyzing the R and G value. In other words, exciton were blocked in the bottom crystal. We can finally conclude that the light emission difference in figure 6.10 is due to exciton diffusion from the bottom crystal to the top crystal, rather than light propagation or photoexcitation.

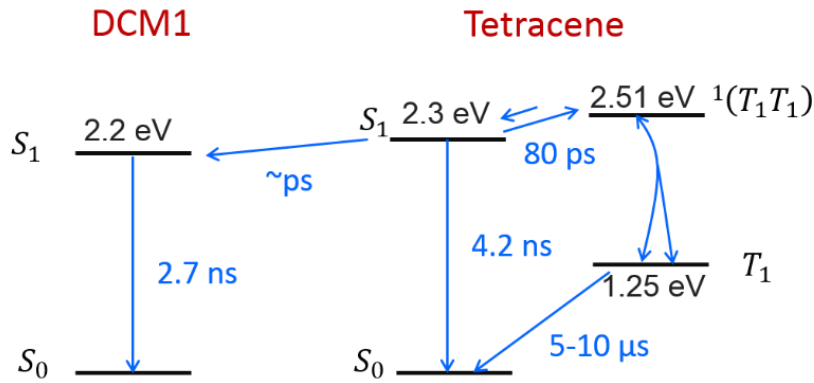


Figure 6.13. Energy level diagram of tetracene and DCM1. Here S_1 is the lowest singlet state, T_1 is the lowest triplet state and $^1(T_1T_1)$ is optical dark state of triplet pair.

A mechanism in this bilayer transistor can be brought out: field-effect carriers have a recombination at the bottom of tetracene crystal, the quantum efficiency of generated singlets and triplets are 0.25 and 0.75, respectively. According to references 154, the quantum yield for singlet fission was estimated to be 2, which is due to the much longer decay time of the other competing process fluorescence (lifetime is 4.2 ns). So the generated singlets are soon converted into triplets, and formed triplets are 1.25 ($0.75+2\times 0.25$) in quantum yield. Then this amount of triplets have a diffusion and the possibility of them to come to the bilayer interface can be calculated by $\exp(-x/L_{EX})$, where x is the thickness of bottom crystal and L_{EX} is the exciton diffusion length along c axis determined in chapter 5. The possibility of the triplets migrate to bilayer interface is 0.732 when thickness of bottom crystal is 583 nm measured by AFM. So at the interface, the quantum yield of triplets is 0.915 (1.25×0.732). In the top layer which is composed by DCM1-doped tetracene crystal, as illustrated that energy transfer from host tetracene to guest DCM1 is in several picoseconds which is faster than the singlet fission, that is why we can improve the luminescent efficiency from 1% to 8%.

Here we would like to discuss about the photo efficiency in this bilayer transistor, photons created in the top crystal is not only determined by the luminescent efficiency but also determined by the transfer efficiency of excitons between the bilayers. The light intensity is supposed to be 5 times higher than that in the bottom layer. However, in figure 6.8c, light emission from top crystal

cannot be observed higher intensity than that in the bottom layer, the large amount of exciton blocking maybe due to the perpendicular lamination of these two crystals.

6.4 Conclusions

DCM1-doped tetracene crystals were prepared by using physical vapor transport method. Their crystalline phase were characterized by polarizing optical microscope. Optoelectronic properties including luminescent spectra, external quantum yield as well as carrier transport were characterized in both pure and doped tetracene crystals. Bilayer transistor composed with tetracene crystal as carrier transporter (bottom layer) and DCM1-doped tetracene crystal as light emitter (top layer) was fabricated. To balance the electron- and hole-injection, CsF was insert between Ca and tetracene crystal. Red light emission from top crystal which is different from that in tetracene (green light-emission color) was observed. This result proved our anticipation that excitons were formed in the bottom crystal and transferred to the top crystal with red-color light emission. To further prove this mechanism, an insulator TTC thin film was inserted between tetracene crystal and DCM1-doped crystal, only green light emission was observed in the device, which means excitons were blocked by TTC thin film. We finally realized the separation of carrier-transport and light-emission functions by fabricating a bilayer light-emitting transition.

Chapter VII

General Conclusions and Future Perspectives

7.1 Conclusions

Realizing electrically driven lasers is still a challenge that sufficient exciton density must be created for population inversion. Exciton density is determined by the mean factor i.e. charge-carrier mobility in LE-FETs. On the other hand, high luminescent efficiency is also a crucial factor for realizing lasers that they are capable to reduce the nonradiative losses caused by quenching and supplement the photo absorbed by electrodes.

Based on the aforementioned statement, we found that the exciton behavior in organic semiconducting crystal is a crucial factor for realizing lasers. For example, ASE behavior is due to interaction between photons and excitons, doping which can improve optical property is determined by energy transfer (exciton migration), also, singlet fission and its reverse process i.e. triplet fusion make the exciton diffusion length to be in micro-scale.

To realize laser, investigating gain property is a necessary process because laser contains only a gain media with a resonator. In chapter 3, we focus on specific analysis of gain properties of BP2T, BP2F and BPFT single crystals. By comparing both the absorption and fluorescence spectra of these three co-oligomers in both single-crystalline and deposited thin-film forms, we assigned the dual gain-narrowed peaks corresponding to the vibronic transitions from $S_{1,0}$ to $S_{0,n}$ state. Combining the transient absorption spectra with ground-state absorption spectra, we finally determined that the number of gain-narrowed peaks corresponding vibronic transitions is affected by the re-absorption from

both the ground-state and excited-state molecules, and energy distribution of this gain behavior is determined by transition probability from $S_{1,0}$ to $S_{0,n}$ and bleaching of the ground-state absorption. ASE and SF processes have been attributed to vibronic transition $S_{1,0}$ - $S_{0,1}$ and $S_{1,0}$ - $S_{0,2}$ in BPFT single crystal, respectively. Furthermore, gain with the highest efficiency can be expected when only the vibronic transition with the highest transition probability is confined in the window of absorption at both ground state and singlet state. This research is not only the first report of the mechanism describing energy efficiency and its distribution but also a good guide to design materials for laser.

In chapter 4, tetracene-doped anthraene crystal is employed as a model for studying doping system based on RET theory. Both the fluorescent spectra and much more improved luminescent efficiency proved that there was an efficient energy transfer from the donor molecule to the acceptor molecule. Furthermore, we have successfully overcome the differences of molecular structures and their stacking modes, finally doped a certain quantity of CNDPASDB into trans-DPDSB by solution growth method, and maintained the original crystal structure of host crystal as proved by polarizing optical microscope analysis. Light emission color can be tuned by changing the doping ratio, due to intrinsically high QY of the host material and efficient energy transfer from trans-DPDSB molecules to CNDPASDB molecules. Therefore, emission spectra can cover both the emission region of the host (blue color) and that of the guest (orange color). With suitable balance of the ratio between host and guest, white light emission was successfully obtained. Moreover, superb high EQY (~80%) comparable with that in solution was obtained by doping, and it slightly decreased with increasing the doping ratio due to the singlet-singlet annihilation. Finally, carrier transport characteristic was also investigated in both pure trans-DPDSB and its doped crystals. It is concluded that dopant with smaller energy band gap may introduce carrier-traps, which means if the problem of carrier-trap is overcome in the doping system, electrically driven laser may be realized.

As well known that high luminescent efficiency and high carrier mobility cannot coexist in one material. An idea came to us that we can separate these two factors into two layers, and assign the combination of these two layers as active layer. In this case, light-emission and carrier-transport functions can be separated. We will fabricate such bilayer FET, and realize the separation of

light-emission and carrier-transport functions. In chapter 6, we designed a novel device structure which can separate the carrier-transport and light-emission functions into two crystal layers. This device structure can divide the two important yet conflicting factors, high luminescent efficiency and high carrier mobility, making the device promise to realize electrically driven lasers. .

7.2 Future Perspectives

The pursuit for current-driven organic laser will remain a great challenge for several years to come, particularly from the viewpoint of the related fundamental physics. The field of easily processed organic semiconductor lasers is young at more than a decade old and advancing rapidly. As we look to the future, the realization of electrically driven lasers will be a breakthrough in the field of organic photonics. The development of device and material will help reduce threshold. Also the emerging technologies such as inject printing will pave the way for lasers to become practical sources, initially for use in a range of spectroscopic applications. From the applicational viewpoint, the organic semiconductor community expects current-driven organic laser can be available by the year 2030.

This doctor research had challenged several alternatives, mainly focus on the exciton behavior in organic crystals, to pursuit the electrically driven organic lasers. Some issues are worth to be expended:

Firstly, molecular design is in a need of improvement. Figure 7.1 illustrates spectra of an idealized organic semiconducting material, from which we can see that the absorption in the ground state and singlet state act as a casement, only vibronic transitions in the gap between these two absorptions can be a gain-narrowed peaks, in other words, the number of gain-narrowed peaks is confined by the gap. Moreover, when only a vibronic transition with the highest transition probability (transition S_{10} to S_{01} in the schematic spectra) shows in the window, energy will be concentrated and gain behavior with the most efficiency can be expected.

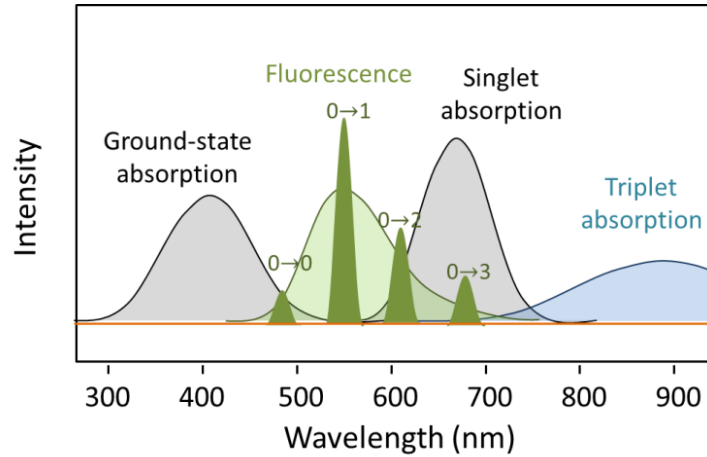


Figure 7.1. Schematic spectra of idealized material with the most energy efficiency. The separated narrowed peaks correspond to vibronic transitions.

Secondly, a novel device structure is demanded such as proposed in chapter 6. A bilayer device which separates the carrier-transport and light-emission functions, smartly avoided the conflict between high luminescent efficiency and high carrier transfer issues. If more suitable materials are applied, electrically driven laser can be expected.

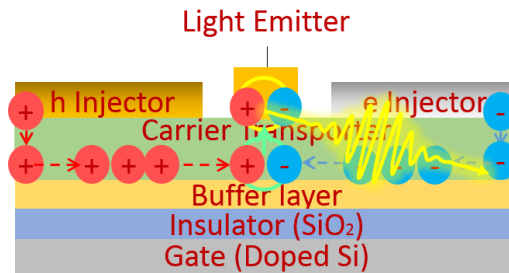


Figure 7.2. Schematic side-view diagram of bilayer light-emitting transistors. Green layer at bottom stands for carrier transporter, top layer act as light emitter.

Mechanism can be described that after electrons and holes accumulation, they will have a recombination to form excitons, the excitons diffuse to the top layer with light emission.

References

- [1] T. H. Maiman, *Nature*, **1960**, *187*, 493.
- [2] M. Dantus, R. M. Bowman, A. H. Zewail, *Nature*, **1990**, *343*, 737.
- [3] M. Pope and C. E. Swenberg, *Electronic Processes in Organic Crystals and Polymers*, 2nd ed. (Oxford University Press, New York, 1999).
- [4] F. Hide, M. A. Díaz-García, B. J. Schwartz, M. R. Andersson, Q. Pei and A. J. Heeger, *Science*, **1996**, *273*, 1833.
- [5] N. G. Tessler, J. Denton, R. H. Friend, *Nature*, **1996**, *38*, 695.
- [6] N. Tessler, *Adv. Mater.*, **1999**, *11*, 363.
- [7] M. Pope, H. P. Kallmann, P. Maganante, *J. Chem. Phys.*, **1963**, *38*, 2042.
- [8] N. Karl, *Phys. Stat. Sol. (a)*, **1972**, *13*, 651.
- [9] O. S. Avensjan, V. A. Bendeerskii, V. K. Brikenstein *et al.*, *Mol. Cryst. Liq. Cryst.*, **1974**, *29*, 165,
- [10] Y. V. Naboikin, L. A. Ogurtsova, A. P. Podgorny *et al.*, *Sov. J. Quantum Electron.*, **1978**, *8*, 457.
- [11] R. H. Friend, R. W. Gymer, A. B. Holmes and J. H. Burroughes, *Nature*, **1999**, *397*, 121.
- [12] C. W. Tang, S. A. VanSlyke and C. H. Chen, *J. Appl. Phys.*, **1989**, *65*, 3610.
- [13] I. Musubu, N. Kiyoshi, I. Masamitsu and T. Yoshio, *Appl. Phys. Lett.*, **2005**, *87*, 221113.
- [14] T. Siegrist, C. Kloc, R. A. Laudise, H. E. Katz and R. C. Haddon, *Adv. Mater.*, **1998**, *10*, 379.
- [15] C. D. Dimitrakopoulos and P. R. L. Malenfant, *Adv. Mater.*, **2002**, *14*, 99.
- [16] R. W. I. de Boer, M. E. Gershenson, A. F. Morpurgo and V. Podzorov, *Phys. Status Solidi A*, **2004**, *201*, 1302.
- [17] M. Ichikawa, R. Hibino, M. Inoue, T. Haritani, S. Hotta, T. Koyama and Y. Taniguchi, *Adv. Mater.*, **2003**, *15*, 213.
- [18] H. Yanagi, T. Ohara, and T. Morikawa, *Adv. Mater.*, **2001**, *13*, 1452.
- [19] I. D. W. Samuel, and G. A. Turnbull, *Chem. Rev.*, **2007**, *107*, 1272.
- [20] J. Takeya, C. Goldmann, S. Haas, K. P. Pernstich, B. Ketterer and B. Batlogg, *J. Appl. Phys.*, **2003**, *94*, 5800.

- [21] R. W. I. de Boer, T. M. Klapwijk, and A. M. Morpurgo, *Appl. Phys. Lett.*, **2003**, *83*, 4345.
- [22] T. Hasegawa, K. Mattenberger, J. Takeya and B. Batlogg, *Phys. Rev. B: Condens. Matter Mater. Phys.*, **2004**, *69*, 245115.
- [23] C. Vijila, N. G. Meng, Z. K. Chen, et al., *J. Polym. Sci. Pol. Phys.*, **2008**, *46*, 1159.
- [24] M. Redecker, D. D. C. Bracley, M. Inbasekaran, et al., *Appl. Phys. Lett.*, **1998**, *73*, 1565.
- [25] E. B. Namdas, M. H. Tong, P. Ledochowitsch et al., *Adv. Mater.*, **2009**, *21*, 799.
- [26] V. Podzorov, E. Menard, A. Borissov et al., *Phys. Rev. Lett.*, **2004**, *93*, 086602.
- [27] T. Takenobu, S. Z. Bisri, T. Takahashi, M. Yahiro, C. Adachi and Y. Iwasa, *Phys. Rev. Lett.* **2008**, *100*, 6.
- [28] K. Sawabe, T. Takenobu, S. Z. Bisri et al., *Appl. Phys. Lett.*, **2010**, *97*, 043307.
- [29] H. Wang, Z. Q. Xie, B. Yang, F. Z. Shen, Y. P. Li and Y. G. Ma, *CrystEngComm*, **2008**, *10*, 1252.
- [30] P. G. Kloc, Ch., Simpkins, T. Siegrist and R. A. Laudise, *J. Cryst. Growth*, **1997**, *182*, 416.
- [31] R. A. Laudise, P. G. Kloc, Ch., Simpkins and T. Siegrist, *J. Cryst. Growth*, **1998**, *187*, 449.
- [32] M. Campione, R. Ruggione, S. Tavazzi and M. Moret *J. Mater. Chem.*, **2005**, *15*, 2437.
- [33] B. Fraboni, C. Femoni., Mencareli, I. et al., *Adv. Mater.*, **2009**, *21*, 1835.
- [34] S. Manetta, M. Ehrensperger, C. Bosshard, P. Gunter, *C. R. Phys.* **2002**, *3*, 449.
- [35] H. Shang, H. Wang, N. Gao, F. Shen, X. Li and Y. Ma, *CrystEngComm*, **2012**, *14*, 869.
- [36] A. Moliton, , *Optoelectronics of molecules and polymer*, Springer: **2006**.
- [37] H. Wang, Z. Q. Xie, Y. G. Ma, and J. C. Shen, *Sci. China, Ser. B: Chem.*, **2007**, *50*, 433 .
- [38] H. S. Avanesyan, V. A. Benderskii, V. K. Brikenstein et al, *Phys. Stat. Sol. (a)*, **1975**, *30*, 781.
- [39] M. Schwoerer, H. C. Wolf, *Organic Molecular Solids*, Wiley-VCH: 2007.

- [40] C. H. Zhao, A. Wakamiya, Y. Inukai, et al, *J. Am. Chem. Soc.*, **2006**, *128*, 15934.
- [41] Y. P. Li, F. Li, H. Y. Zhang, Z. Q. Xie, W. J. Xie, H. Xu, B. Li, F. Z. Shen, L. Ye, M. Hanif, D. G. Ma, and Y. G. Ma, *Chem. Commun.* 2007, 231
- [42] J. Cornil, D. A. Dos Santos, X. Crispin et al, *J. Am. Chem. Soc.*, **1998**, *120*, 1289.
- [43] Z. Xie, B. Yang, F. Li, L. L. Liu, G. D. Yang, H. Xu, L. Ye, M. Hanif, S. Y. Liu, D. G. Ma, Y. G. Ma, *J. Am. Chem. Soc.*, **2005**, *127*, 14152.
- [44] N. Sanyal, P. M. Lahti, *Cryst. Growth Des.*, **2006**, *6*, 1253.
- [45] N. Sanyal, Amherst: Univ. of Massachusetts, **2007**.
- [46] Z. Q. Xie, H. Wang, F. Li, W. J. Xie, L. L. Liu, B. Yang, L. Ye, and Y. G. Ma, *Cryst. Growth Des.* **2007**, *7*, 2512.
- [47] W. J. Feast, P. W. Lovenich, H. Puschmann et al, *Chem. Comm.* **2001**, 505.
- [48] C. W. Tang, S. A. Van Slyke, C. H. Chen, *J. Appl. Phys.*, **1989**, *65*, 3610
- [49] M. Ichigawa, R. Hibino, M. Inoue, T. Haritani, S. Hotta, K. Araki, T. Koyama and Y. Taniguchi, *Adv Mater*: **2005**, *17*, 2073.
- [50] X. J. Li, N. Gao, Y. X. Xu, F. Li, Y. G. Ma, *Appl. Phys. Lett.* **2012**, *101*, 063301.
- [51] F. H. H et al. *Adv. Funct. Mater.* 2012, *22*, 33.
- [52] V. G. Kozlov, S. R. Forrest, *Curr. Opin. Solid State Mater. Sci.*, **1999**, *4*, 203.
- [53] R. Zamboni, R. Capelli, S. Toffanin et al, *Proc.SPIE*, **2008**, *7118*, 71180C-1.
- [54] T. Takahashi, T. Takenobu, J. Takeya, Y. Iwasa, *Adv. Funct. Mater.*, **2007**, *17*, 1623.
- [55] S. Z. Bisri, T. Takenobu, Y. Yomogida, H. Shimotani, T. Yamao, S. Hotta and Y. Iwasa, *Adv. Funct. Mater.* **2009**, *19*, 1728.,
- [56] R. Capelli, S. Toffanin, G. Generali, H. Usta, A. Facchetti and M. Muccini, *Nat. Mater.* **2010**, *9*, 496
- [57] J. Zaumseil, R. H. Friend, H. Sirringhaus, *Nature Mater.*, **2006**, *5*, 69.
- [58] N. Karl, *Synth. Met.*, **2003**, *133*, 649.
- [59] S. Z. Bisri, K. Sawabe, M. Imakawa, K. Maruyama, T. Yamao, S. Hotta, Y. Iwasa, T. Takenobu, *Scientific Reports*, **2012**, *2*, 985.
- [60] K. Sawabe, M. Imakawa, M. Nakano, T. Yamao, S. Hotta, Y. Iwasa, T. Takenobu, *Adv Mater*. **2012**, *24*, 46
- [61] S. Hotta, H. Kimura, S. A. Lee, T. Tamaki, *J. Heterocycl. Chem.*, **2000**, *37*, 281.

- [62] A. Okada, Y. Makino, S. Hotta and T. Yamao, *Phys. Status. Solidi. C*, **2012**, *9*, 2545.
- [63] K. Maruyama, K. Sawabe, T. Sakanoue, J. P. Li, W. Takahashi, S. Hotta, Y. Iwasa, T. Takenobu, , *Scientific Reports*, **2015**, *5*, 10221
- [64] S. A. Lee, Y. Yshida, M. Fukuyama, S. Hotta, *Synth. Met.* **1999**, *106*, 39.
- [65] K. Oniwa, T. Kanagasekaran, T. Jin, Md. Akhtaruzaman, Y. Yamamoto, H. Tamura, H. Shimotani, N. Asao, S. Ikeda and K. Tanigaki, *J. Mater. Chem. C* **2013**, *1*, 4163.
- [66] H. Mizuno, U. Haku, Y. Marutani, A. Ishizumu, H. Yanagi, F. Sasaki and S. Hotta, *Adv. Mater.* **2012**, *24*, 5744.
- [67] Y. Wang, R. Kumashiro, Z. Li, R. Nouchi, K. Tanigaki, *Appl. Phys. Lett.* **2009**, *95*, 103306.
- [68] S. Hotta, M. Goto, R. Azumi, M. Inoue, M. Ichikawa and Y. Taniguchi, *Chem. Mater.*, **2004**, *16*, 237.
- [69] H. M. Cuppen, W. S. Graswinckel, and H. Meekes, *Crystal Growth & Design*, **2004**, *4*, 1351.
- [70] Y. akahashi and M. Tomura, *J.Phys. Soc. Jpn.* **1971**, *31*, 1100.
- [71] Y. Nozue, M. Kawaharada and T. Coto, *J.Phys. Soc. Jpn.* **1987**, *56*, 4176.
- [72] Y. Nozue, *J. Phys. Soc. Jpn.* 1988, *57*, 3204.
- [73] Y. Nozue and T. Goto, *J. Phys. Soc. Jpn.* 1989, *58*, 1831.
- [74] M. Pope and C. E. Swenberg, *Electronic Processes in Organic Crystals and Polymers*, 2nd ed. (Oxford University Press, New York, 1999).
- [75] A. N. Aleshin, J. Y. Lee, S. W. Chu, J. S. Kim, and Y. W. Park, *Appl. Phys. Lett.*, **2004**, *84*, 5383.
- [76] K. P. Seefeld, H. Muller, H. Bassler, *J. Lumin.* **1978**, *16*, 395
- [77] Godzik, K.; Jortner, J. *J. Chem. Phys.* **1980**, *72*, 4471
- [78] R. C. Powell and Z. G. Soos, *J. Lumin.* **1975**, *11*, 1
- [79] R. C. Powell, R. G. Kepler, *Phys. Rev. Lett.* **1969**, *22*, 636
- [80] M. Pope, P. Magnante, H. P. Kallmann, *J. Chem. Phys.* **1963**, *38*, 2042
- [81] J. H. Wu, Z.P. Guan, T. Z. Xu, Q. H. Xu and G. Q. Xu, *Langmuir* **2011**, *27*, 6374.
- [82] C. E. Swenberg, W. T. Jones, *Chem. Phys. Lett.* **1972**, *14*, 305.
- [83] M. B. Smith and J. Michl, *Chem. Rev.* **2010**, *110*, 6891.

- [84] C. C. Wu, O. J. Korovyanko, M. C. Delong, Z. V. Vardeny, and J. P. Ferraris, *Synth. Met.* **2003**, *139*, 735
- [85] Y. P. Li, F. Z. Shen, H. Wang, F. He, Z. Q. Xie, H. Y. Zhang, Z. M. Wang, L. L. Liu, F. Li, M. Hanif, L. Ye, and Y. G. Ma, *Chem. Mater.* **2008**, *20*, 7312.
- [86] J. Takeya, et al, *Appl. Phys. Lett.* **2004**, *85*, 5078.
- [87] T. J. Richards and H. Sirringhaus, *Appl. Phys. Lett.* **2008**, *92*, 023512
- [88] T. J. Richards and H. Sirringhaus, *J. Appl. Phys.* **2007**, *102*, 094510
- [89] D. Pisignano, M. Anni, G. Gigli, R. Cingolani, M. Zavelani-Rossi, G. Lanzani, G. Barbarella and L. Favaretto, *Appl. Phys. Lett.* **2002**, *81*, 3534.
- [90] I. D. W. Samuel, E. B. Namdas and G. A. Turnbull, *Nat. Photonics*, **2009**, *3*, 546.
- [91] M. C. Gwinner, S. Khodabakhsh, M. H. Song, H. Schweizer H. Giessen and H. Sirringhaus, *Adv. Funct. Mater.* **2009**, *19*, 1360.
- [92] D. Fichou, S. Delysse and J. Nunzi, *Adv. Mater.* **1997**, *9*, 1178.
- [93] G. Horowitz, F. Kouki, A. E. Kassmi, P. Valat, V. Wintgens, F. Garnier, *Adv. Mater.* **1999**, *11*, 234.
- [94] M. Nagawa, R. Hibino, S. Hotta, H. Yanagi, M. Ichikawa, T. Koyama, Y. Taniguchi, *Appl. Phys. Lett.* **2002**, *80*, 544.
- [95] P. A. Losio, C. Hunziker and P. Gunter, *Appl. Phys. Lett.* **2007**, *90*, 241103.
- [96] M. Polo, A. Camposeo, S. Tavazzi, L. Raimondo, P. Spearman, A. Papagni, R. Cingolani, D. Pisignano, *Appl. Phys. Lett.* **2008**, *92*, 083311.
- [97] R. Kabe, H. Nakanotani, T. Sakanoue, M. Yahiro, C. Adachi, *Adv. Mater.* **2009**, *21*, 4034.
- [98] H. Tamura, I. Hamada, H. Shang, K. Oniwa, Md. Akhtaruzzaman, T. Jin, N. Asao, Y. Yamamoto, T. Kanagasekaran, H. Shimotani, S. Ikeda and K. Tanigaki, *J. Phys. Chem. C*, **2013**, *117*, 8072.
- [99] S. Hotta, M. Goto, R. Azumi, M. Inoue, M. Ichikawa and Y. Taniguchi, *Chem. Mater.* **2004**, *16*, 237.
- [100] R. Katoh, K. Suzuki, A. Furube, M. Kotani and K. Tokumaru, *J. Phys. Chem. C*, **2009**, *113*, 2961.
- [101] E. Condon, *Phys. Rev.* **1926**, *28*, 1182.
- [102] K. Bando, T. Nakamura, S. Fujiwara and Y. Matsumoto, *Phys. Rev. B* **2008**, *77*, 045205.
- [103] F. T. Arecchi and E. Courtens, *Phys. Rev. A* **1970**, *2*, 1730.

- [104] R. Bonifacio and L. A. Lugiato, *Phys. Rev. A* **1975**, *11*, 1507.
- [105] J. C. MacGillivray and M. S. Feld, *Phys. Rev. A* **1976**, *14*, 1169.
- [106] S. V. Frolov, Z. V. Vadenny and K. Yoshino, *Phys. Rev. B* **1998**, *57*, 9141.
- [107] T. Hiramatsu, N. Matsuoka, H. Yanagi, F. Sasaki and S. Hotta, *Phys. Stat. Sol. C* **2009**, *6*, 3
- [108] S. L. Tao, C. S. Lee, S.T. Lee and X. H. Zhang, *Appl. Phys. Lett.* 2007, **91**, 013507
- [109] Y. Y. Lyu, J. Kwak, O. Kwon, S. H. Lee, D Kim, C. Lee and K. Char, *Adv Mater.* 2008, **20**, 2720–2729
- [110] W. Chang, G. M. Akselrod, and V. Bulović, *ACS Nano*, 2015, **9**, 4412–4418
- [111] H. Wang, F. Li, B. R. Gao, Z. Q. Xie, S. J. Liu, C. L. Wang, D. H. Hu, F. Z. Shen, Y. X. Xu, H. Shang, Q. D. Chen, Y. G. Ma and H. B. Sun, *Cryst. Growth&Des.* 2009, **9** , 4945–4950
- [112] K.E. Sapsford, L. Berti and I. L. Medintz, *Angew. Chem. Int. Ed.* **2006**, *45*, 4562.
- [113] Y. S. Zhao, J. S. Wu and J. X. Huang, *J. Am. Chem. Soc.*, 2009, **131**, 3158.
- [114] D. O'Carroll, I. Lieberwirth and G. Redmond, *Nat. Nanotechnol.*, 2007, **2**, 180–184
- [115] H. B. Liu, Q. Zhao, Y. L. Li, F. S. Lu, J. P. Zhuang, S. Wang, L. Jiang, D. B. Zhu, D. P. Yu, L. F. Chi, *J. Am. Chem. Soc.* 2005, **127**, 1120
- [116] X. J. Zhang, J. S. Jie, W. F. Zhang, C. Y. Zhang, L. B. Luo, Z. B. He, X. H. Zhang, W. J. Zhang, C. S. Lee and S. T. Lee, *Adv Mater.*, 2008, **20**, 2427.
- [117] Y. S. Zhao, C. A. Di, W. S. Yang, G. Yu, Y. Q. Liu and J. N. Yao, *Adv Funct. Mater.*, 2006, **16**, 1985–1991
- [118] Q. X. Tang, H. X. Li, Y. L. Liu, W. P. Hu, *J. Am. Chem. Soc.* 2006, **128**, 14634.
- [119] B. K. An, D. S. Lee, J. S. Lee, Y. S. Park, H. S. Song, S. Y. Park, *J. Am. Chem. Soc.* 2004, **126**, 10232.
- [120] T. Naddo, Y. K. Che, W. Zhang, K. Balakrishnan, X. M. Yang, M. Yen, J. C. Zhao, J. S. Moore and L. Zang, *J. Am. Chem. Soc.*, 2007, **129**, 6978-6979
- [121] Y. K. Che, X. M. Yang, S. Loser and L. Zang, *Nano Lett.*, 2008, **8**, 2219-2223
- [112] O. J. Dautel, G. Wantz, R. Almairac, D. Flot, L. Hirsch, J.-P. Lere-Porte, J.-P. Parneix, F. Serein-Spirau, L. Vignau, J. J. E. Moreau, *J. Am. Chem. Soc.* 2006, **128**, 4892

- [123] A. L. Briseno, S. C. B. Mannsfeld, X. M. Lu, Y. J. Xiong, S. A. Jenekhe, Z. N. Bao and Y. N. Xia, *Nano Lett.*, 2007, **7**, 668-675
- [124] K. Takazawa, Y. Kitahama, Y. Kimura and G. Kido, *Nano Lett.*, 2005, **5**, 1293.
- [125] F. Quochi, F. Cordella, A. Mura, G. Bongiovanni, F. Balzer and H. G. Rubahn, *Appl. Phys. Lett.*, 2006, **88**, 041106
- [126] Y. S. Zhao, A. D. Peng, H. B. Fu, Y. Ma and J. N. Yao, *Adv. Mater.*, 2008, **20**, 1661.
- [127] C. Zhang, C. L. Zou, Y. L. Yan, R. Hao, F. W. Sun, Z. F. Han, Y. S. Zhao and J. N. Yao, *J. Am. Chem. Soc.*, 2011, **133**, 7276.
- [128] A. Patra, S. P. Anthony and T. P. Radhakrishnan, *Adv. Funct. Mater.*, 2007, **17**, 2077
- [129] Z. Zhang, B. Xu, J. Su, L. Shen, Y. Xie and H. Tian, *Angew. Chem., Int. Ed.*, 2011, **50**, 11654
- [130] J. Luo, Z. Xie, J. W. Y. Lam, L. Cheng, H. Chen, C. Qiu, H. S. Kwok, X. Zhan, Y. Liu, D. Zhu and B. Z. Tang, *Chem. Commun.*, 2001, 1740
- [131] Y. Hong, J. W. Y. Lam and B. Z. Tang, *Chem. Commun.*, 2009, 4332.
- [132] D. P. Yan, W. Jones, G. L. Fan, M. Wei and D. G. Evans, *J. Mater. Chem. C*, 2013, **1**, 4138.
- [133] Y. S. Zhao, H. B. Fu, F. Q. Hu, A. D. Peng, W. S. Yang, and J. N. Yao, *Adv. Mater.* 2008, **20**, 79.
- [134] J. H. Wu, Z. P. Guan, T. Z. Xu, Q. H. Xu, and G. Q. Xu, *Langmuir*, 2011, **27**, 6374.
- [135] T. Forster, *Discuss. Faraday Soc.* 1959, **27**, 7
- [136] B. Kippelen and J. L. Bredas, *Energy Environ. Sci.* **2009**, **2**, 251
- [137] T. Mori and K. Kato, *J. Photopolymer Sci. Technol.* **2007**, **20**, 61.
- [138] P. Peumans, A. Yakimov and S. R. Forrest, *J. Appl. Phys.* **2004**, **93**, 3693.
- [139] L. G. Yang, H. Z. Chen and M. Wang, *Thin Solid Films*, **2008**, **516**, 7701.
- [140] H. Najafov, B. Lee, Q. Zhou, L. C. Feldman and V. Porzorov, *Nat. Mater.* **2010**, **9**, 938.
- [141] A. K. Ghosh and T. Feng, *J. Appl. Phys.* **1978**, **49**, 5982.
- [142] R. R. Lunt, N. C. Giebink, A. A. Belak, J. B. Benziger, S. R. Forrest, *J. Appl. Phys.* **2009**, **105**, 053711.

- [143] V. M. Agranovich and G. F. Bassani, *Electronic Excitations in Organic Based Nanostructures*, **2003**, 45–47 (Elsevier Academic).
- [144] L. S. Devi, M. K. Al-Suti, C. Dosche, M. S. Khan, R. H. Friend, and A. Köhler, *Phys. Rev. B*, **2008**, *78*, 045210.
- [145] C. E. Swenberg and N. E. Geacintov, *Org. Mol. Photophysics*, **1973**, *18*, 489
- [146] C. E. Swenberg and W. T. Stacy, *Chem. Phys. Lett.* **1968**, *2*, 327.
- [147] W. Y. Zhao, P. Wei, Q. J. Zhang, H. Peng, W. T. Zhu, D. G. Tang, J. Yu, H. Y. Zhou, Z. Y. Liu, X. Mu, D. Q. He, J. C. Li, C. L. Wang, X. F. Tang and J. H. Yang, *Nat. Comm.* **2015**, *6*, 6197.
- [148] H. H. Fang, J. Yang, J. Feng, T. Yamao, S. Hotta, H. B. Sun, *Laser & Photonics Reviews*, **2014**, *8*, 5
- [149] Hotta, S., Kimura, H., Lee, S. A., Tamaki, T., *J. Heterocycl. Chem.*, **2000**, *37*, 281.
- [150] T. Mutai, H. Satou and K. Araki, *Nat. Mater.* **2005**, *4*, 685.
- [151] A. Inoue, T. Hosokawa, M. Haishi and N. Ohtani, *phys. Stat. sol. c*, **2009**, *6*, 334.
- [152] K. J. Baeg, J. Kim, D. Khim, M. Caironi, D. Y. Kim, I. K. You, J. R. Quinn, A. Facchetti and Y. Y. Noh, *ACS Appl. Mater. Interfaces*, **2011**, *3*, 3205.
- [153] L. S. Hung, C. W. Tang, M. G. Mason, *Appl. Phys. Lett.* **1997**, *70*, 152.
- [154] V. K. Thorsmølle et al., *Phys. Pev. Lett*, **2009**, *102*, 017401.

Curriculum Vitae

PERSONAL INFORMATION

Name Hui SHANG

Date of Birth 25/06/1985

Citizen P. R. China

Address WPI-AIMR, Tohoku University,
2-1-1, Katahira, Aoba-ku, Sendai, 980-8577, Japan.

Phone +81-22-217-6173 (Office); +81-09029862093 (Mobile)

E-mail shanghui0625@gmail.com



EDUCATION

10/2012-9/2015 Ph. D of Science, Physics, Tohoku University, Japan.

10/2010-9/2012 Master of Science, Physics, Tohoku University, Japan.

9/2005-7/2009 Bachelor of Science, Chemistry, Jilin University, China.

HONOR & AWARDS

2010-2015 President Scholarship for Foreign Students, Tohoku University,
Japan

2010-2014 National Scholarship for Overseas PhD Student, China
Scholarship Council

2012 GCOE Young Scientist Initiative A, Japan

2006-2009 Third-Class of Undergraduate Scholarship, Jilin University, China

2005 Outstanding Freshman Scholarship, Jilin University, China.

Publication List

1 Hui Shang, Huan Wang, Na Gao, Fangzhong Shen, Xianjie Li, Yuguang Ma, “Large Organic Single Crystal sheets Grown from the Gas-Liquid and Gas-Liquid-Solid Interface”, *CrystEngComm*, **14**, 869, 2012.

2 Hui Shang, Hidekazu Shimotani, Susumu Ikeda, Kanagasekaran Thangavel, Kazuaki Oniwa, Tienan Jin, Naoki Asao, Yoshinori Yamamoto, Hiroyuki Tamura, Kenta Abe, Masayuki Yoshizawa, Katsumi Tanigaki, “Gain Properties of Thiophene/Furan/Phenylene Co-oligomer Single Crystals: Energy Efficiency and Distribution”, to be submitted.

3 Hui Shang, Hidekazu Shimotani, Zengqi Xie, Huan Wang, Yuguang Ma, and Kazumi Tanigaki, “Size Controllable One-Dimensional Doped Organic Crystals with Color Tunable Light Emission and Superb High Luminescent Efficiency”, to be submitted.

4 Hui Shang, Hidekazu Shimotani, Kanagasekaran Thangavel, Katsumi Tanigaki, “Separation of Carrier-Transport and Light-Emission Functions in a Light-Emitting Organic Transistor with Bilayer Configuration”, under preparation.

5 Huan Wang, Feng Li, Bingrong Gao, Zengqi Xie, Suijun Liu, Chunlei Wang, Dehua Hu, Fangzhong Shen, Yuanxiang Xu, **Hui Shang**, Qidai Chen, Yuguang Ma and Hongbo Sun, “Doped Organic Crystals with High Efficiency, Color-Tunable Emission toward Laser Application”, *Crystal Growth & Design*, **9**, 11, 4945, 2009.

6 Yan Wang, Dandan Liu, Susumu Ikeda, Ryotaro Kumashiro, Ryo Nouch, Yuanxiang Xu, **Hui Shang**, Yuguang Ma and Katsumi Tanigaki, “Ambipolar behavior of 2, 5-diphenyl-1, 4-distyrylbenzene based field effect transistors: An experimental and theoretical study”, *Appl. Phys. Lett.*, **97**, 033305, 2010.

7 Hiroyuki Tamura, Ikutaro Hamada, **Hui Shang**, Kazuaki Oniwa, Md. Akhtaruzzaman, Tienan Jin, Naoki Asao, Yoshinori Yamamoto, Thangavel Kanagasekaran, Hidekazu Shimotani, Susumu Ikeda and Katsumi Tanigaki, “Theoretical Analysis on the Optoelectronic Properties of Single Crystals of Thiophene-furan-phenylene Co-Oligomers: Efficient Photoluminescence due to Molecular Bending”, *J. Phys. Chem. C*, **117**, 8072–8078, 2013.

8 Fucui Liu, Hidekazu Shimotani, **Hui Shang**, Thangavel Kanagasekaran, Viktor Zólyomi, Neil Drummond, Vladimir I. Fal’ko, and Katsumi Tanigaki, “High-Sensitivity Photodetectors Based on Multilayer GaTe Flakes”, *ACS Nano*, **8**, 752, 2014.

9 Feng Li, Na Gao, Hai Xu, Wei Liu, **Hui Shang**, Wenjun Yang and Ming Zhang, “Relationship between molecular stacking and optical properties of

9,10-bis((4-N,N-dialkylamino)styryl) anthracene crystals: the cooperation of excitonic and dipolar coupling”, *Chem. Eur. J.*, **20**, 9991, 2014.

10 Huan Wang, Yang Zhao, Zengqi xie, **Hui Shang**, Huaiyuan Wang, Feng Li and Yuguang Ma, “Preparation, optical property and field-effect mobility investigation of stable white-emissive doped organic crystal”, *CrystEngComm*, **17**, 2168, 2015.

11 Thangavel Kanagasekaran, Hidekazu Shimotani, Susumu Ikeda, **Hui Shang**, Ryotaro Kumashiro, and Katsumi Tanigaki, “Equivalent ambipolar carrier injection of electrons and holes with Au electrodes in air-stable field effect transistors” *Appl. Phys. Lett.* **107**, 043304, 2015

International Presentations

- April 2012 MRS Spring Meeting- “Optoelectronic Properties of Newly Synthesized Furan/ Phenylene Co-oligomer Single Crystal”, San Francisco, USA, poster.
- October 2012 OIST International Symposium on Organic Electronics 2012 - “Investigation on Gain Properties of Organic Single Crystals towards Electrically Driven Lasers”, Okinawa, Japan, poster.
- December 2014 MRS Fall Meeting- “Gain Properties of Thiophene/Furan/ Phenylene Co-oligomer Single Crystals: Energy Efficiency and Distribution”, Boston, USA, poster.

Acknowledgements

I would like to express my gratitude to all of those who selflessly provide their helps during this 5 years in Japan. As a student from foreign country, I am proud to say that I will never regret to come to Tohoku University, which is notable for its excellent education as well as research.

My deepest gratitude first goes to Prof. Katsumi Tanigaki and Prof. Hidekazu Shimotani, my adviser and supervisor, for their constant encouragement and guidance. They have walked me through all the stages of the writing of this dissertation. Without their consistent and illuminating instruction, this dissertation could not have reached its present form. Also, they always gave me a lot of help in the daily life which made me feel comfortable and homey in Japan.

Also, I would like to convey my appreciation to Professor Yuguang Ma, my supervisor in Jilin University, who led me into the world of the science. Without his encouragement and kindly support, I may never have the chance to enjoy research of science. Dr. Huan Wang also supported me a lot and it is not exaggerated to say that he is a model to me due to his excellent research ability and good morality.

I am also greatly indebted to the professors and researchers from Tohoku University: Prof. Susumu Ikeda, Prof. Masayuki Yoshizawa, Dr. Kanagasekaran Thangavel, Dr. Hiroyuki Tamura, Dr. Kazuaki Oniwa and

Prof. Tienan Jin. They supplied their best supports and instructions in my research.

Also, my thanks would go to: Jiazhen Wu, who has helped me a lot on study of physical knowledge; Hirota-kun, Kobayashi-kun, Nakao-kun, Oikawa-kun, Shirai-kun and Kasai-kun from FET team, with whom the seminars and textbook study were meaningful and interesting; all the members in Tanigaki-lab, who give me a lot of supports in campus life.

At last, I would like to express my heartfelt gratitude to my father, my mother and my husband for their considerations and great confidence in me all through these years. Their encouragement gives me the courage to continue my studying in a foreign country. I also owe my sincere gratitude to my friends, who gave me their help and time listening to me and helping me work out my problem in my life.